

## ABSTRACT

WU, FAN. Planar Defects in Metallic Thin Film Heterostructures. (Under the direction of Prof. Jagdish (Jay) Narayan and Prof. Yuntian Zhu.)

Twin and phase interfaces are two important types of planar defects in nanocrystalline (NC) thin film heterostructures. Formation of twins in NC metals plays a critical role in their physical and mechanical properties. The introduction of twins in NC metal films has been reported to result in a combination of ultra-high strength and good ductility, good electrical conductivity and excellent resistance to current-induced diffusion, much better thermal stability (stable at 800 C for 1 hr) and negligible grain growth (little grain size change at room temperature for 1 yr). Meanwhile, the stress relief by formation of twins in thin film fabrication helps to avoid damage in a microelectronic device and prolong its service life. Despite the reported advances in properties, the twinning mechanisms in NC thin film heterostructures have remained poorly understood. In this project, the following aspects of twinning mechanisms in NC thin film heterostructures were studied: 1) the formation of twins and grain size dependence of twin density in as-fabricated NC Cu films were investigated for the first time; 2) twin intersection mechanisms in NC fcc metals were understood by observing twin transmission across the boundary of another twin. A partial dislocation reaction model was proposed for twin transmission phenomenon and evidenced by experimental observation. The observations and mechanisms proposed in this project can be applied in other twin intersection phenomena in all fcc materials; 3) the long-

existing question about the dominant mechanism for the formation of deformation twins in NC fcc metals with zero macrostrain was answered, by a novel design of experimental approach in this project.

The interface between different phases is another type of important planar defect. It will play an increasingly important role in device performance when device size shrinks to several monolayers thick. In this project, the following aspects of interfacial phase formation in NC thin film heterostructures were studied: 1) the world's first bcc/fcc Cu and MgO structure was fabricated on Si using TiN as the buffer layer and the detailed atomic structure at Cu/MgO interface was studied; 2) epitaxial Ni/MgO stack was successfully integrated on Si substrate and the atomic structure at Ni/MgO interface was studied. The distinctive magnetic properties as a function of Ni thin film morphology were investigated for the first time; 3) the world's first Cu<sub>3</sub>Ge/sapphire thin film structure was fabricated and the first study of twinning structure inside the Cu<sub>3</sub>Ge thin films was performed.

© Copyright 2014 by Fan Wu

All Rights Reserved

Planar Defects in Metallic Thin Film Heterostructures

by  
Fan Wu

A dissertation submitted to the Graduate Faculty of  
North Carolina State University  
in partial fulfillment of the  
requirements for the Degree of  
Doctor of Philosophy

Materials Science and Engineering

Raleigh, North Carolina

2014

APPROVED BY:

-----

Prof. Jagdish Narayan

Co-Chair of the Advisory Committee

-----

Prof. Yuntian Zhu

Co-Chair of the Advisory Committee

-----

Prof. John T. Prater

-----

Prof. Korukonda Murty

## **DEDICATION**

To

My grandmother, who raised me up with unconditional love;

My parents, who taught me the importance of honesty, kindness and forgiveness;

My family, who always supports me to overcome difficulties;

And all people who have influenced me in a positive way...

You deserve my gratitude from the bottom of my heart!

## BIOGRAPHY

Fan Wu was born on December 12<sup>th</sup>, 1989, to Mrs. Hui Jun Shao and Mr. Zhu Ming Wu in Hangzhou, China. This is a beautiful capital city, which is famous for its rare combination of gorgeous natural scenery and prosperous civilization. Fan was enrolled on August 17<sup>th</sup>, 2007, into Materials Science and engineering department at Zhejiang University, which ranked #3 in China at that time. As a junior during his undergraduate program, he got exchanged to University of Alberta, Canada, where he won the Chancellor's Research Award for a research program in which he contributed as a leader. He was the first foreign student to be granted this honor. After completing his college as an outstanding graduate in Zhejiang Province, he continued his journey in Materials Science and Engineering at North Carolina State University, USA. Starting from August 2011, he received a Master of Science degree and a Doctor of Philosophy degree within a total span of 2 years and 11 months, under the guidance of Prof. Jagdish Narayan and Prof. Yuntian Zhu, at the NSF Center for Advanced Materials and Smart Structures. Upon graduation, he received an offer for a postdoctoral researcher position at Princeton University, a postdoctoral researcher position at Duke University, an offer for a vacuum engineer position at Seagate and an offer for an assistant professor position at Nanjing University of Science and Technology. Dr. Wu is devoting himself to a career of scientific research.

## ACKNOWLEDGMENTS

I would like to express my sincere gratitude to Prof. Jagdish Narayan and Prof. Yuntian Zhu for their continuous support, guidance, and encouragement throughout this project. Both of them devote themselves to scientific research with undiminished passion, despite their admirable reputation. Their expertise in the fields of thin film and deformation twinning, as well as selfless guidance laid a solid foundation for my future development as a professional researcher. Their rigorous attitudes towards research set an example of excellence to me. I highly appreciate the great degree of freedom they gave me to be the master of my own project.

I am also cordially grateful to Prof. John T. Prater. His insightful advice and constructive comments are indispensable to the successful completion of this work. I also appreciate Prof. Korukonda Murty's time as one of my advisory committee members. It's my greatest honor to have these four prestigious professors on board. Their guidance helped me in a great deal to march forward continuously.

It's my greatest pleasure to thank my colleagues and dear friends: Dr. Sudhakar Nori, Dr. Alok Gupta, Dr. Pranav Gupta, Dr. M. Reza Bayati, Dr. Roya Molaei, Dr. Srinivasa Rao, Dr. Wan-jui Shen, Yifang Lee, Namik Temizer, S. Punugupati, Dr. Weiwei Jian, Dr. Xin Wang, Dr. Chongxiang Huang, Dr. Orm Piyawit, Zhou Zhou, Weizong Xu, Xiaolong Ma, Hao Zhou, Jordan Moore and many others who shared their expertise and collaborated with me throughout this project. They made my journey towards Ph.D degree more

enjoyable. It would never be possible without their support throughout my doctoral research at NC State.

I would also like to thank all the administrative staff in the department of Materials Science and Engineering at NC State University, especially Edna Deas, for her prompt help with the administrative work.

I am indebted to anyone who has helped me or collaborated with me, on or off campus. Even if they are not mentioned in the list here, they are living in my heart.

This project is financially supported by US National Science Foundation through grant number of DMR-1104667, without which the project would not have been possible.

## TABLE OF CONTENTS

<b>LIST OF TABLES .....</b>	<b>xii</b>
<b>LIST OF FIGURES .....</b>	<b>xiii</b>
<b>Chapter 1 Introduction .....</b>	<b>1</b>
References .....	11
<b>Chapter 2 Background Knowledge .....</b>	<b>24</b>
2.1 Substrate materials.....	24
2.1.1 Si.....	24
2.1.2 Sapphire .....	25
2.2 Buffer layers .....	27
2.2.1 Titanium Nitride (TiN) .....	27
2.2.2 Magnesium Oxide (MgO) .....	28
2.3 Thin film epitaxy .....	29
2.3.1 Thin film growth modes.....	30
2.3.2 Strain Sources .....	34
2.3.3 Lattice matching epitaxy.....	37
2.3.4 Domain matching epitaxy.....	39

2.4 Deformation twinning mechanisms in nanocrystalline fcc materials.....	42
2.4.1 Twinning by partial emission from grain boundaries.....	44
2.4.2 Twinning by overlapping of stacking fault ribbons.....	44
2.4.3 Twinning with macroscopically low strain .....	45
2.4.4 Sequential twinning mechanism.....	47
2.4.5 Twinning by grain boundary splitting and migration.....	47
2.4.6 Partial multiplication at twin boundaries .....	48
2.4.7 Dislocation rebound mechanism .....	48
2.5 Grain size effect on deformation twinning .....	48
2.6 General planar fault energy effect on deformation twinning.....	49
References .....	51
<b>Chapter 3 Experimental Techniques .....</b>	<b>58</b>
3.1 Substrate Preparation.....	58
3.2 Pulsed Laser Deposition (PLD) .....	59
3.2.1 Laser-solid interaction mechanism .....	61
3.2.2 Advantages of PLD.....	68
3.2.3 Drawbacks of PLD .....	70
3.3 X-Ray Diffraction.....	71
3.4 Transmission Electron Microscopy.....	73
3.4.1 Introduction.....	73

3.4.2 Basic operating principles.....	74
3.4.3 TEM Sample preparation.....	77
3.4.4 Operation Mode.....	83
3.4.5 Astigmatism, beam shift and tilt .....	88
3.4.6 Scanning transmission electron microscope (STEM).....	89
3.5 Magnetic characterization.....	90
References .....	92
<b>Chapter 4 Grain size effect on twin density in as-deposited nanocrystalline Cu film</b>	
.....	<b>94</b>
4.1 Introduction.....	94
4.2 Experimental Approach .....	96
4.3 Results and Discussion .....	98
4.3.1 Grain size distribution .....	98
4.3.2 Grain size effect on twin density in NC Cu grains.....	103
4.4 Conclusions .....	109
References .....	110
<b>Chapter 5 Twin intersection mechanisms in nanocrystalline fcc metals .....</b>	<b>115</b>
5.1 Introduction.....	115
5.2 Experimental Approach .....	117

5.3 Results and Discussion .....	118
5.3.1 TEM and HRTEM observation of twin transmission across twin boundary .....	118
5.3.2 Possible dislocation reactions at the intersection of two twin boundaries .....	121
5.3.3 Explanation of the experimentally observed twin transmissions.....	124
5.4 Conclusions .....	130
References .....	131
<b>Chapter 6 Macroscopic strain by twinning in nanocrystalline Cu.....</b>	<b>135</b>
6.1 Introduction.....	135
6.2 Experimental Approach .....	139
6.3 Results and Discussion .....	140
6.3.1 Texture and Stress State of the Cu Film .....	140
6.3.2 Microstructure in the Cu/Ta Film .....	144
6.3.3 Twins with Zero Macrostrain.....	148
6.3.4 Twins with Macrostrain .....	149
6.4 Conclusions .....	153
References .....	154

**Chapter 7 Controlled epitaxial growth of bcc and fcc Cu on MgO for integration on**

<b>Si.....</b>	<b>161</b>
7.1 Introduction.....	162
7.2 Experimental Approach .....	165
7.3 Results and Discussion .....	165
7.4 Conclusions .....	177
References .....	179
<b>Chapter 8 Fabrication and investigation of the interface between Ni and MgO on Si</b>	
<b>.....</b>	<b>186</b>
8.1 Introduction.....	186
8.2 Experimental Approach .....	188
8.3 Results and Discussion .....	190
8.4 Conclusions .....	202
References .....	203
<b>Chapter 9 Interface and twinning in Cu<sub>3</sub>Ge/sapphire thin film heterostructures</b>	
<b>.....</b>	<b>208</b>
9.1 Introduction.....	208
9.2 Experimental Approach .....	211
9.3 Results and Discussion .....	213
9.4 Conclusions .....	224

9.5 Supporting Information .....	226
References .....	228
<b>Chapter 10 Concluding Remarks.....</b>	<b>231</b>
References .....	235

## LIST OF TABLES

<b>Table 2.1</b> Optical properties of MgO .....	29
<b>Table 6.1</b> The layer thicknesses and grain size ranges for films 1 to 5 .....	146
<b>Table 8.1</b> The correlation between Out-of-plane lattice constants, in-plane and out of plane strain, coercive field, and exchange bias .....	194
<b>Table 9.1</b> PLD parameters of Cu <sub>3</sub> Ge thin films for sample 1 to 5.....	213

## LIST OF FIGURES

<b>Figure 2.1</b> The schematic illustration of the different crystallographic planes of sapphire .....	26
<b>Figure 2.2</b> A schematic illustration of thin film growth steps: (a) Deposition of atoms from the vapor. (b) Surface movement/ diffusion of the adatoms. (c) Formation of clusters by nucleation. (d) Addition of adatoms to existing clusters. (e) Dissociation of clusters and (f) Evaporation .....	31
<b>Figure 2.3</b> Schematic illustration of the three growth modes of thin films: Frank-van der Merwe or layer-by-layer growth, Volmer-Weber or island growth, and Stranski-Krastanov or layer-by-layer followed by island growth.....	34
<b>Figure 2.4</b> Schematic illustration of lattice matching epitaxy.....	39
<b>Figure 2.5</b> Schematic illustration of domain matching epitaxy (DME).....	40
<b>Figure 3.1</b> Schematic illustration demonstrating the variation of the density ( $n$ ), pressure ( $P$ ), and velocity ( $V$ ) as a function of distance away from the target surface.....	65
<b>Figure 3.2</b> (a) Schematic illustration of the plasma shape right after the laser pulse terminates. (b) Final shape of the plasma when it hits the substrate.....	67

**Figure 3.3** Schematic view of the TEM column ..... 76

**Figure 4.1** (a) HRTEM micrograph of a NC Cu grain in which a twin exists. (b) HRTEM micrograph of a twin in large Cu grains (~40-50 nm) ..... 100

**Figure 4.2** (a) Grain size distribution of the NC Cu film on Si. (b) B-N model fitting of the grain size distribution of NC Cu film on Si ..... 102

**Figure 4.3** (a) The distribution of number of grains that contain twins as a function of grain size. (b) Dependence of surface area density of twins on  $d^2$  (grain surface area over  $4\pi$ ) for different grain size ranges. (c) Percentage of grains containing twins for different grain sizes ..... 105

**Figure 5.1** (a) A typical HRTEM image showing twin transmission phenomenon in NC Cu films processed by PLD and the subsequent uniaxial elongation. (b) The HRTEM image showing the transmission area shown in (a) with marks added. (c) A typical TEM image showing twin transmission phenomenon in NC Brass 260 alloy processed by cryo-milling and the following SPS. (d) The HRTEM image showing the twin transmission area in (c) with marks added ..... 119

**Figure 5.2** Schematic illustration of a double Thompson tetrahedron ..... 122

<b>Figure 5.3</b> Schematic illustrations of twin transmission phenomena with (a) $\theta= 35.25^\circ$ , (b) $\theta= 0^\circ$ , and (c) $\theta= 43^\circ$ .....	125
<b>Figure 5.4</b> (a) An HRTEM image enlarged from the MTB area in Figure 5.1 (a). (b) An HRTEM image enlarged from the MTB area in Figure 5.1 (c) .....	128
<b>Figure 6.1</b> XRD $\theta$ - $2\theta$ scan patterns for 5 different Cu/Ta multilayer films integrated on Si substrates .....	141
<b>Figure 6.2</b> Schematic illustration of $\sigma_{xx}$ , $\sigma_{yy}$ , $\sigma_{zz}$ and different $\{111\}$ planes of Cu within the multilayer structure.....	143
<b>Figure 6.3</b> (a) Cross-sectional dark field (DF) image of a typical Cu/Ta multilayer film on Si substrate. (b) Cross-sectional dark field (DF) image of another Cu/Ta multilayer structure on Si substrate. (c) The typical $\langle 110 \rangle$ zone- axis selected area diffraction pattern (SADP) of the Si/Cu/Ta multilayer heterostructure. Cu layers are $\{111\}$ textured, while Ta layers are too thin to show diffraction spots on the SADP. (d) The typical HRTEM image showing the structure of Cu/Ta layers and the interface morphology .....	147
<b>Figure 6.4</b> Typical NC Cu twinned grains with zero macroscopic strains, as manifested by smooth grain boundaries. The out-of-plane direction is shown as the arrow.....	149

**Figure 6.5** Typical NC Cu twinned grains with macroscopic strains, as manifested by shape change (kink angles) on grain boundaries. The out-of-plane direction for each part of the image is marked by the arrows.....152

**Figure 7.1** Schematic illustration of (a) 3-D atomic structure demonstrating the crystallographic relationship between bcc(t) Cu/MgO(100). (b) 2-D atomic structure of bcc(t) Cu/MgO(100), viewed along  $[001]_{\text{bcc(t) Cu}} \parallel [001]_{\text{MgO}}$ , perpendicular to the interface plane. (c) 2-D atomic structure of bcc(t) Cu/MgO(100), viewed parallel to the interface plane. (d) 3-D atomic structure demonstrating the crystallographic relationship between bcc(t) Cu/MgO(111). (e) 2-D atomic structure of bcc(t) Cu/MgO(111), viewed along  $[011]_{\text{bcc(t) Cu}} \parallel [-111]_{\text{MgO}}$ , perpendicular to the interface plane. (f) Schematic illustration of 2-D atomic structure of bcc(t) Cu/MgO(111), viewed parallel to the interface plane.....167

**Figure 7.2** (a) Typical TEM bright-field cross-section image showing the whole stack Cu/MgO(100)/TiN(100)/Si(100). Pt layer was deposited for protection during the FIB sample preparation process. (b)  $[110]$  zone-axis-pattern (ZAP) of Si(100)/TiN(100) interface. (c)  $[110]$  ZAP of MgO(100)/TiN(100) interface. (d) A typical HRTEM image showing the Cu/MgO(100) interface. (e) A typical HRTEM image showing the atomic structure of bct Cu at the Cu/MgO(100) interface region.....170

**Figure 7.3** (a) Typical TEM bright-field cross-section image showing the whole stack Cu/MgO(111)/TiN(111)/Si(111). Pt layer was deposited for protection during the FIB sample preparation process. (b) [110] zone-axis-pattern (ZAP) of Si(111)/TiN(111) interface. (c) [110] ZAP of MgO(111)/TiN(111) interface. (d) - (f) HRTEM images of fcc Cu/ MgO (111) interface at different magnifications, viewed along [110] direction. (g) Schematic illustration of the hexagonal dislocation network on (111) planes between two close-packed lattices (fcc Cu/MgO) with a cube-on-cube relationship..... 171

**Figure 7.4** (a) A typical HRTEM image in which island-shaped bcc(t) Cu and epitaxial fcc Cu coexist on MgO(111). (b) Enlarged HRTEM image showing the island region where bcc Cu lattice appears. (c) [110] ZAP of fcc Cu. (d) [110] ZAP of MgO. (e) [111] ZAP of bcc Cu. (f) Simulated [110] ZAP of fcc Cu and [111] ZAP of bcc Cu ..... 176

**Figure 8.1** The  $\theta$ -2 $\theta$  XRD patterns of the three multilayer Ni/MgO/TiN/Si(100) heterostructures, for which the deposition pulses of Ni are 1500, 3500 and 7000 pulses, respectively ..... 191

**Figure 8.2** (a) The typical cross-sectional bright field (BF) TEM image of Ni1. (b) The [110] zone-axis SADP of Ni1, in which the diffraction patterns corresponding to Si, TiN, MgO and Ni are labeled. (c) The typical cross-

sectional BF TEM image of Ni2. (d) The typical cross-sectional BF TEM image of Ni3.....197

**Figure 8.3** (a) STEM-Z contrast image demonstrating the Ni/ MgO (100) interface, viewed along <110> direction for both Ni and MgO phases. (b) HRTEM image showing the Ni/ MgO (100) interface, in which DME mechanism is labeled in detail .....198

**Figure 8.4** (a) Comparison of isothermal M-H curves measured on Ni1, Ni2 and Ni3 under in-plane configuration measured 4 K. (b) A significant M-H loop shift toward the positive magnetic field axis, called positive exchange bias (PEB) for Ni1, negative exchange bias (NEB) (M-H loop shift toward negative field axis) for Ni2 and PEB for Ni3 have been observed when each sample was cooled under zero field and then measured during the warming up cycle .....200

**Figure 9.1** XRD  $\theta$ -2 $\theta$  patterns for samples on c-plane sapphire ( $Al_2O_3\{0001\}$ ). For all five samples, the laser shot frequency is 1HZ, the deposition temperature is 400C, and 90 repetitions of depositions of Cu/Ge were performed, while numbers of laser pulses for Cu and Ge depositions are different: sample 1: Cu:Ge=35:5; sample 2: Cu:Ge=25:5; sample 3: Cu:Ge=15:5; sample 4: Cu:Ge=14:2; sample 5: Cu:Ge=7:1 .....214

**Figure 9.2** (a) The typical bright-field cross-section TEM image showing the film morphology of sample 5. (b) The zone-axis pattern (ZAP) of sample 5, clearly demonstrating an epitaxial relationship between the single-crystal  $\text{Cu}_3\text{Ge}$  island and c-sapphire substrate .....218

**Figure 9.3** (a) The HRTEM image showing the atomic structure at the interface region between the  $\text{Cu}_3\text{Ge}$  island and c-sapphire substrate. The viewing direction is  $[110]$  zone of c-sapphire (  $[11-20]$  zone in Miller-Bravais Indices system). (b) The schematic illustration of the matching scenario at the interface between  $\epsilon_1\text{-Cu}_3\text{Ge}(010)$  and c-sapphire  $(0001)$ . (c) The HRTEM image at a higher magnification showing the atomic structure at the interface in detail, at the region close to that of (a).....221

**Figure 9.4** A typical HRTEM image showing the planar defects in  $\text{Cu}_3\text{Ge}$  thin film, in which twins and stacking faults coexist.....223

**Figure S9.1** (a)-(e) The plan-view images of samples (1)-(5) respectively, observed by optical microscope .....226

**Figure S9.2** Typical plan-view SEM image of the  $\text{Cu}_3\text{Ge}$  film in sample 5, showing a uniform  $\text{Cu}_3\text{Ge}$  film grown via 3-D growth mode, without the formation of chunks and excessive Ge grains .....227

# Chapter 1

## Introduction

Deformation mechanisms identified in nanocrystalline (NC) materials include partial dislocation emission from grain boundaries [1-8], deformation twinning [1-8], perfect dislocation slip [2, 4, 6], grain boundary sliding [2, 9-13], and grain rotation [3, 6, 14]. The unique deformation mechanisms [15-18] in NC materials control their mechanical properties. Deformation twinning has been frequently observed in NC face-centered cubic (fcc) materials under various deformation conditions, including low temperature [19], high strain rate [20], high-pressure torsion [21], uniaxial tensile testing [10] and cryo-genic ball milling [22], even in materials such as copper and nickel with medium to high stacking fault energies [23, 24]. Therefore, twinning becomes one of the important deformation mechanisms for NC materials [1, 6]. Formation of twins in NC metals [23, 25, 26] plays a critical role in their physical and mechanical properties. For example, the introduction of twins in Cu has been reported to result in a combination of ultra-high strength and good ductility [27-32], due to interactions between twins and gliding dislocations at twin boundaries. These interactions will inevitably occur because of the simultaneous slip of dislocations along with deformation twins, and have been observed both experimentally [27, 33-36] and by

molecular dynamics simulations [37-39]. The ultra-high strength of these materials originates from the strengthening effect of the high density of TBs, which is analogous to the Hall–Petch behavior exhibited by the NC grains [31]. Dislocations interact with twin boundaries and may be blocked by them (similar to the effect of grain boundaries), leading to the ultra-high strength [19, 28]. It is good for the mechanical stability of the multilayered Cu interconnect structure and also good for Chemical Mechanical Polishing (less dishing) during the manufacturing process (damascene procedure) [40]. The good ductility also originates from the interaction of dislocations with the twin boundaries [41], during which twin boundaries act as dislocation sources or sinks, contributing to the good ductility of nano-twinned structures [7, 41, 42]. It is also reported that NC Cu with high density of twins have good electrical conductivity and excellent resistance to current-induced diffusion [27, 43]. The rare combination of excellent mechanical strength and low electrical resistivity are valuable for Cu to serve as interconnecting wires in integrated circuits, from the perspective of the resistive-capacitive delay, electromigration, and stress migration [44-46]. The triple points where twin boundaries meet grain boundaries were found to slow down or block the electromigration-induced atomic transport of Cu by one order of magnitude under current stressing, due to a longer incubation time of the nucleation of steps [43]. Twins in Cu films were also reported to result in a much better thermal stability (stable at 800 C for 1 hr) [47] and much less grain growth (little grain size change at room temperature for 1 yr) [48]. Therefore, deformation twinning in NC materials is of both

fundamental and practical importance, and can be utilized to design NC materials for superior mechanical and physical properties.

The grain size effect on twinning in NC fcc Ni was systematically investigated by Wu and Zhu [49], who observed that the twinning propensity first increases then drops with increasing grain size in the range of 10–75 nm. Similar grain size effect on twinning in NC fcc Cu was later observed in other systems [50, 51]. These observations correlate well with the prediction made by an analytical model of Zhu et al. [52]. Schiøtz and Jacobsen have observed by molecular dynamic simulation for NC metals that the critical grain size for inverse Hall-Petch effect for Cu was 7.5 nm, which indicates the importance of grains smaller than 10 nm [53]. However, there have been no experimental reports regarding the grain size effect on the formation of twins during the synthesis of NC metal films. In this project, the grain size effect (in the size range of ~2 nm to ~10 nm) on twin density in as-deposited NC copper films was investigated. The characteristics and number density of twins were studied as a function of grain size, and the internal strain inside the NC Cu thin film was calculated. The detailed results can be found in Chapter 4 of this thesis.

When multiple twinning systems are activated in fcc metals, interactions between various twinning systems become inevitable. This not only affects the microstructural evolution but also is expected to affect the mechanical behavior of the material during deformation. Twin intersections have been observed in fcc stainless steel [54] and Hadfield steel single crystals [55]. However, these experimental observations raise a

critical unresolved question: what is the dislocation mechanism governing the observed twin intersections? This question is of both fundamental and technological significance. To answer the above question, the intersections of twins in NC Cu film and Cu-30 wt% Zn-0.8 wt% Al alloy (Brass 260, Cartridge Brass) samples were studied in this project. These two material systems were selected because NC Cu has been reported to easily form deformation twins [23, 56], and the Brass 260 alloy has lower stacking fault energy than Cu and also easily forms deformation twins and twin intersections [57]. The detailed investigation process and results can be found in Chapter 5 of this thesis.

One of the most salient features of deformation twins in NC fcc metals is that most of them produce very little or even zero macroscopic strain [58-60]. A deformation twin is formed by the slip of multiple partials. While the slip of an individual partial produces local strain, the net strain from slips of multiple partials could sum to zero on a macroscopic scale, producing a deformation twin with zero-macrostrain. This is in sharp contrast to a deformation twin in conventional coarse-grained fcc metals, which is usually produced by the slip of partials with the same Burgers vectors so that a macroscopic strain exists. Whether deformation twins in NC metals produce macroscopic strain may have a significant effect on their microstructural evolution and mechanical behavior during tensile testing. For example, it is known that grain rotation [61] and grain boundary sliding [61] occur extensively during the deformation of NC metals, which may lead to grain growth. Deformation twins that do not produce macroscopic strain will result in a smooth grain boundary [58], which will make grain

rotation and grain boundary sliding easier. Therefore, it is of great importance to understand how the microstructures and stress conditions affect the formation of twins with zero macroscopic strain. Two mechanisms have been proposed for deformation twins with zero macroscopic strain. One is the random activation of partials (RAP) mechanism by Wu et al. [58], in which partial dislocations with different Burgers vectors are randomly activated. The RAP mechanism was proposed to require the change of local stress orientation with time during deformation, so that the resolved shear stress on partials with different Burgers vectors varied with time during the deformation. Grain rotation and grain boundary sliding were believed to promote the RAP mechanism. The other mechanism was proposed by Wang et al. [59] and Li et al. [60], which involved the cooperative slip of three partials (CSTP) with the sum of their Burgers vectors equaling zero, generating twins with zero-macrostrain. This mechanism does not require the variation of local stress orientation. However, a critical issue remains unsolved: which mechanism plays a major role in the formation of deformation twins with zero-macrostrain in NC fcc metals? This issue is further complicated because monotonic activation of partial (MAP) dislocations with the same Burgers vector was also found in NC fcc metals [62]. Although the MAP twins are in small percentage, they form under the same stress condition as the CSTP twins. To solve this issue, the RAP in NC Cu grains is suppressed in this project by designing a layer-by-layer microstructure, to deter the grain rotation and grain boundary sliding of NC Cu grains during the deformation. In addition, the nanograins are textured to have

their {111} planes parallel to the film surface, and the residual stress is oriented to have resolved shear stress on one type of partial dislocations only. Such a microstructure and stress state not only suppresses the RAP mechanisms, but also should promote the CSTP mechanism and the MAP mechanism. This unique experimental design helps solve the critical issue on the dominant mechanism governing the formation of deformation twins with zero-macrostrain in NC fcc metals. The detailed investigation process and results can be found in Chapter 6 of this thesis.

Unlike twins, phase interface is another kind of planar defects between two phases. The interfaces between dissimilar metals often exhibit unique atomic arrangements and properties that are not found in bulk crystals [63]. Cu/MgO interface is of great importance because it plays a crucial role in applications such as microelectronics packaging, coating, and corrosion protection [64], catalysis, metal-matrix composites, recording media, etc. [65]. The epitaxial growth of fcc Cu on MgO has been reported at different temperatures [66, 67]. However, despite the growth of bcc Cu on substrates such as Nb [68], Ag [69], and Pd [70], no bcc(t) Cu has been fabricated onto MgO, which has a rock salt structure. The special atomic structure of the fcc/bcc(t) interface plays a decisive role in determining mechanical, electrical, thermal, and diffusion properties of thin film heterostructures, such as elevated strength [71, 72], superplasticity [73], and suppression of fatigue [74]. The special microstructure of bcc/fcc interface produces ultra-high strengths and enhanced radiation damage

tolerance, due to a short diffusion distance to the nearest sink. The bcc/fcc interface acts as sinks for vacancies and interstitials [75], enhances their recombination, and helps the material on both sides of the interface to persist in a damage-free steady state even when driven out of equilibrium by intense particle radiation. With regard to mechanical properties, the bcc/fcc interface acts as a strong barrier for slip transmission because the dislocation core spreads in interfaces as a result of their low shear resistance [76, 77]. Therefore it is of great technical importance to study the microstructure and matching mechanism of bcc(t)/rock salt interfaces between bcc(t) Cu and MgO. In this project, the world's first epitaxial bcc(t) Cu was fabricated on MgO template and the interface between two phases was investigated in detail. This is the first systematic study on bcc(t) Cu on MgO templates with different orientations (MgO(100) and MgO(111)). The first integration of the technologically important Si substrate holds tremendous promise in microelectronics industry. The detailed investigation process and results can be found in Chapter 7 of this thesis.

Metal-oxide [78] interfaces are of growing interest from both fundamental and technological viewpoints. Ni/MgO is one of the most attractive metal-ceramic systems due to its high temperature stability, the excellent tunneling barrier characteristics of MgO, and the ferromagnetic properties of Ni [79]. In addition, Ni films can work as an effective buffer/seed layer for growing other materials like carbon nanotubes [80]. Various studies have been done on the Ni/MgO system. For instance, Raatz and Woltersdorf [81] reported the effect of Ni film thickness on its film orientation.

McCaffrey [82], Svedberg [83], Reniers [84] and Qiu [85] et al studied the effect of growth temperature on the orientation of epitaxial Ni films on MgO(001). Lukaszew [86] et. al. studied the magneto-optic Kerr effect (the magnetization-induced change in polarization state and/or intensity of the light reflected from the surface of a magnetized medium) of Ni thin films grown on MgO single crystal substrate. Furthermore, there have been several reports on Ni nanowires [87] and thin films [88] that were used to engineer the magnetic properties for data storage applications. Unfortunately, all of the above investigations have been focused on Ni films grown on MgO substrates using MBE and sputtering techniques, while the investigation on the interface between epitaxial Ni thin films and MgO buffer layers prepared on Si(100) substrates is missing. In this project, epitaxial Ni/MgO stack was successfully integrated on the technologically important, inexpensive, readily available and widely used silicon substrate, by fabricating an epitaxial MgO template on Si using TiN as the buffer layer. The interface between Ni and MgO was investigated. Furthermore, the distinctive magnetic properties such as transition of exchange bias ( $H_{EB}$ ) (from positive to negative to positive) and coercive field ( $H_c$ ) (technologically relevant magnetic device parameters) were studied as a function of Ni thin film morphology and thickness. The detailed investigation process and results can be found in Chapter 8 of this thesis.

$Cu_3Ge$  has been considered to be a candidate for contacts and interconnections, as an alternative to Cu, due to its low bulk resistivity ( $\sim 6 \mu\Omega \text{ cm}$  compared with  $\sim 2 \mu\Omega \text{ cm}$  for Cu) over a large Ge composition range of 25-35 at.% Ge [89, 90] and its stability up

to 450 °C [89]. It also reduces the out diffusion of Cu [91], and remains stable against oxidation in air up to ~500 °C [91, 92]. The Cu<sub>3</sub>Ge ε<sub>1</sub>-phase has been grown in the form of polycrystalline films on various substrates/templates, such as Si [91, 93-95], Si<sub>x</sub>Ge<sub>1-x</sub> [93, 94, 96], Ge [95, 97], GaAs [98-100], GaN [101], YBa<sub>2</sub>Cu<sub>3</sub>O<sub>7-x</sub> [102], Ta/TaN [103]. However, no fabrication of Cu<sub>3</sub>Ge films on sapphire has been reported, thus the interface between Cu<sub>3</sub>Ge and sapphire has not been investigated. Due to its low electrical but high heat conductivities, sapphire has been widely used as an insulating substrate in high-power, high-frequency CMOS integrated circuits, especially for high-power radio-frequency applications. Consequently, the integration of Cu<sub>3</sub>Ge as contacts or interconnections onto sapphire substrates will have tremendous promise in semiconductor industry. In this project, epitaxial Cu<sub>3</sub>Ge thin films were fabricated on c-plane sapphire substrates and the interface between Cu<sub>3</sub>Ge and sapphire was investigated. Furthermore, twinning in as-grown Cu<sub>3</sub>Ge thin films were studied for the first time. The detailed investigation process and results can be found in Chapter 9 of this thesis.

To summarize, twins and phase interfaces were studied as two important planar defects in metallic thin film heterostructures in this project. The thesis is organized into 10 chapters. The introduction chapter is followed by a chapter talking about the relevant background knowledge, giving the readers a general idea about some concepts that are of critical importance in this project. The third chapter is on experimental methods, which describes the experimental approach and methodology that are

adopted to accomplish the goals set for this Ph.D project. Chapter 4-9 describe the research results in detail, showing the readers the research accomplishments in this project. The specific contents in these 6 chapters are listed as following.

Chapter 4: Grain size effect on twin density in as-deposited nanocrystalline Cu film;

Chapter 5: Twin intersection mechanisms in nanocrystalline fcc metals;

Chapter 6: Macroscopic twinning strain in nanocrystalline Cu;

Chapter 7: Fabrication and investigation of the interface between bcc/fcc Cu and  
MgO on Si;

Chapter 8: Fabrication and investigation of the interface between Ni and MgO on  
Si;

Chapter 9: Interface and twinning in  $\text{Cu}_3\text{Ge}$ /sapphire thin film heterostructures.

Chapter 10: The overall conclusions are summarized. Most of this work has been published in peer reviewed journals [57, 104-108].

## References

1. Liao, X.Z., et al., *Deformation twinning in nanocrystalline copper at room temperature and low strain rate*. Applied Physics Letters, 2004. **84**(4): p. 592-594.
2. Schiotz, J., F.D. Di Tolla, and K.W. Jacobsen, *Softening of nanocrystalline metals at very small grain sizes*. Nature, 1998. **391**(6667): p. 561-563.
3. Shan, Z., et al., *Grain Boundary-Mediated Plasticity in Nanocrystalline Nickel*. Science, 2004. **305**(5684): p. 654-657.
4. Van Swygenhoven, H., P.M. Derlet, and A. Hasnaoui, *Atomic mechanism for dislocation emission from nanosized grain boundaries*. Physical Review B, 2002. **66**(2): p. 024101.
5. Kumar, K.S., et al., *Deformation of electrodeposited nanocrystalline nickel*. Acta Materialia, 2003. **51**(2): p. 387-405.
6. Liao, X.Z., et al., *High-pressure torsion-induced grain growth in electrodeposited nanocrystalline Ni*. Applied Physics Letters, 2006. **88**(2): p. 021909.
7. Asaro, R.J. and S. Suresh, *Mechanistic models for the activation volume and rate sensitivity in metals with nanocrystalline grains and nano-scale twins*. Acta Materialia, 2005. **53**(12): p. 3369-3382.
8. Rice, J.R., *Dislocation nucleation from a crack tip: An analysis based on the Peierls concept*. Journal of the Mechanics and Physics of Solids, 1992. **40**(2): p. 239-271.

9. Wu, X.-L. and E. Ma, *Deformation twinning mechanisms in nanocrystalline Ni*. Applied Physics Letters, 2006. **88**(6): p. 061905.
10. Wu, X., et al., *Twinning and stacking fault formation during tensile deformation of nanocrystalline Ni*. Scripta Materialia, 2006. **54**(9): p. 1685-1690.
11. Wu, X.-L., Y.T. Zhu, and E. Ma, *Predictions for partial-dislocation-mediated processes in nanocrystalline Ni by generalized planar fault energy curves: An experimental evaluation*. Applied Physics Letters, 2006. **88**(12): p. 121905.
12. Van Swygenhoven, H. and P.M. Derlet, *Grain-boundary sliding in nanocrystalline fcc metals*. Physical Review B, 2001. **64**(22): p. 224105.
13. Yamakov, V., et al., *Deformation-mechanism map for nanocrystalline metals by molecular-dynamics simulation*. Nat Mater, 2004. **3**(1): p. 43-47.
14. Ke, M., et al., *Observation and measurement of grain rotation and plastic strain in nanostructured metal thin films*. Nanostructured Materials, 1995. **5**(6): p. 689-697.
15. Chen, M.W., et al., *Deformation twinning in nanocrystalline aluminum*. Science, 2003. **300**(5623): p. 1275-1277.
16. Yamakov, V., et al., *Dislocation processes in the deformation of nanocrystalline aluminium by molecular-dynamics simulation*. Nature Materials, 2002. **1**(1): p. 45-48.
17. Zhu, Y. and T. Langdon, *The fundamentals of nanostructured materials processed by severe plastic deformation*. JOM, 2004. **56**(10): p. 58-63.

18. Wolf, D., et al., *Deformation of nanocrystalline materials by molecular-dynamics simulation: relationship to experiments?* Acta Materialia, 2005. **53**(1): p. 1-40.
19. Christian, J.W. and S. Mahajan, *Deformation twinning*. Progress in Materials Science, 1995. **39**(1-2): p. 1-157.
20. Meyers, M.A., O. Vohringer, and V.A. Lubarda, *The onset of twinning in metals: A constitutive description*. Acta Materialia, 2001. **49**(19): p. 4025-4039.
21. Liao, X.Z., et al., *Grain-size effect on the deformation mechanisms of nanostructured copper processed by high-pressure torsion*. Journal of Applied Physics, 2004. **96**(1): p. 636-640.
22. Liao, X.Z., et al., *Deformation twins in nanocrystalline Al*. Applied Physics Letters, 2003. **83**(24): p. 5062-5064.
23. Zhu, Y.T., X.Z. Liao, and X.L. Wu, *Deformation twinning in nanocrystalline materials*. Progress in Materials Science, 2012. **57**(1): p. 1-62.
24. Liao, X.Z., et al., *Deformation mechanism in nanocrystalline Al: Partial dislocation slip*. Applied Physics Letters, 2003. **83**(4): p. 632-634.
25. Zhu, Y.T., et al., *Formation of single and multiple deformation twins in nanocrystalline fcc metals*. Acta Materialia, 2009. **57**(13): p. 3763-3770.
26. Narayan, J. and Y.T. Zhu, *Self-thickening, cross-slip deformation twinning model*. Applied Physics Letters, 2008. **92**(15).
27. Lu, L., et al., *Ultra-high Strength and High Electrical Conductivity in Copper*. Science, 2004. **304**(5669): p. 422-426.

28. Lu, L., et al., *Revealing the Maximum Strength in Nanotwinned Copper*. Science, 2009. **323**(5914): p. 607-610.
29. Zhao, Y.H., et al., *Simultaneously increasing the ductility and strength of ultra-fine-grained pure copper*. Advanced Materials, 2006. **18**(22): p. 2949.
30. Zhao, Y.H., et al., *Tailoring stacking fault energy for high ductility and high strength in ultrafine grained Cu and its alloy*. Applied Physics Letters, 2006. **89**(12).
31. Shen, Y.F., et al., *Tensile properties of copper with nano-scale twins*. Scripta Materialia, 2005. **52**(10): p. 989-994.
32. Dao, M., et al., *Strength, strain-rate sensitivity and ductility of copper with nanoscale twins*. Acta Materialia, 2006. **54**(20): p. 5421-5432.
33. Liao, X.Z., et al., *Nanostructures and deformation mechanisms in a cryogenically ball-milled Al-Mg alloy*. Philosophical Magazine, 2003. **83**(26): p. 3065-3075.
34. Lu, K., L. Lu, and S. Suresh, *Strengthening Materials by Engineering Coherent Internal Boundaries at the Nanoscale*. Science, 2009. **324**(5925): p. 349-352.
35. Wang, Y.B. and M.L. Sui, *Atomic-scale in situ observation of lattice dislocations passing through twin boundaries*. Applied Physics Letters, 2009. **94**(2).
36. Wang, Y.B., B. Wu, and M.L. Sui, *Dynamical dislocation emission processes from twin boundaries*. Applied Physics Letters, 2008. **93**(4).
37. Afanasyev, K.A. and F. Sansoz, *Strengthening in Gold Nanopillars with Nanoscale Twins*. Nano Letters, 2007. **7**(7): p. 2056-2062.

38. Henager Jr, C.H. and R.G. Hoagland, *A rebound mechanism for misfit dislocation creation in metallic nanolayers*. Scripta Materialia, 2004. **50**(5): p. 701-705.
39. Jin, J., S.A. Shevlin, and Z.X. Guo, *Multiscale simulation of onset plasticity during nanoindentation of Al (001) surface*. Acta Materialia, 2008. **56**(16): p. 4358-4368.
40. Xu, D., H.P. Chen, and K.N. Tu, *Improved Interconnect Properties For Nano-Twinned Copper: Microstructure And Stability*, in *Stress-Induced Phenomena in Metallization*, E. Zschech, P.S. Ho, and S. Ogawa, Editors. 2010. p. 23-32.
41. Zhu, T., et al., *Interfacial plasticity governs strain rate sensitivity and ductility in nanostructured metals*. Proceedings of the National Academy of Sciences of the United States of America, 2007. **104**(9): p. 3031-3036.
42. Lu, L., et al., *Nano-sized twins induce high rate sensitivity of flow stress in pure copper*. Acta Materialia, 2005. **53**(7): p. 2169-2179.
43. Chen, K.C., et al., *Observation of atomic diffusion at twin-modified grain boundaries in copper*. Science, 2008. **321**(5892): p. 1066-1069.
44. Hu, C.K. and J.M.E. Harper, *Copper interconnections and reliability*. Materials Chemistry and Physics, 1998. **52**(1): p. 5-16.
45. Frankovic, R. and G.H. Bernstein, *Electromigration drift and threshold in Cu thin-film interconnects*. Electron Devices, IEEE Transactions on, 1996. **43**(12): p. 2233-2239.
46. Borgesen, P., et al., *Thermal-Stress-Induced voiding in narrow, passivated Cu lines*. Applied Physics Letters, 1992. **60**(14): p. 1706-1708.

47. Anderoglu, O., et al., *Thermal stability of sputtered Cu films with nanoscale growth twins*. Journal of Applied Physics, 2008. **103**(9).
48. Xu, D., et al., *Nanotwin-modified Copper Interconnects and Its Effect on the Physical Properties of Copper*. 2009 Ieee 59th Electronic Components and Technology Conference, Vols 1-42009. 2060-2063.
49. Wu, X.L. and Y.T. Zhu, *Inverse grain-size effect on twinning in nanocrystalline Ni*. Physical Review Letters, 2008. **101**(2).
50. Zhang, J.-Y., et al., *Double-inverse grain size dependence of deformation twinning in nanocrystalline Cu*. Physical Review B, 2010. **81**(17).
51. Ni, S., et al., *Effect of grain size on the competition between twinning and detwinning in nanocrystalline metals*. Physical Review B, 2011. **84**(23): p. 235401.
52. Zhu, Y.T., et al., *Nucleation and growth of deformation twins in nanocrystalline aluminum*. Applied Physics Letters, 2004. **85**(21): p. 5049-5051.
53. Schiotz, J. and K.W. Jacobsen, *A maximum in the strength of nanocrystalline copper*. Science, 2003. **301**(5638): p. 1357-1359.
54. Roland, T., et al., *Enhanced mechanical behavior of a nanocrystallised stainless steel and its thermal stability*. Materials Science and Engineering: A, 2007. **445-446**(0): p. 281-288.
55. Efstathiou, C. and H. Sehitoglu, *Strain hardening and heterogeneous deformation during twinning in Hadfield steel*. Acta Materialia, 2010. **58**(5): p. 1479-1488.

56. Zhu, Y.T., et al., *Nucleation of deformation twins in nanocrystalline face-centered-cubic metals processed by severe plastic deformation*. Journal of Applied Physics, 2005. **98**(3): p. 034319.
57. Wu, F., et al., *Twin intersection mechanisms in nanocrystalline fcc metals*. Materials Science and Engineering: A, 2013. **585**(0): p. 292-296.
58. Wu, X.L., et al., *New Deformation Twinning Mechanism Generates Zero Macroscopic Strain in Nanocrystalline Metals*. Physical Review Letters, 2008. **100**(9): p. 095701.
59. Wang, J., et al., *Detwinning mechanisms for growth twins in face-centered cubic metals*. Acta Materialia, 2010. **58**(6): p. 2262-2270.
60. Li, B.Q., et al., *Twinning mechanism via synchronized activation of partial dislocations in face-centered-cubic materials*. Scripta Materialia, 2011. **64**(9): p. 852-855.
61. Chinh, N.Q., et al., *Experimental evidence for grain-boundary sliding in ultrafine-grained aluminum processed by severe plastic deformation*. Advanced Materials, 2006. **18**(1): p. 34-39.
62. Ma, E., et al., *Strain hardening and large tensile elongation in ultrahigh-strength nano-twinned copper*. Applied Physics Letters, 2004. **85**(21): p. 4932-4934.
63. Misra, A., J.P. Hirth, and R.G. Hoagland, *Length-scale-dependent deformation mechanisms in incoherent metallic multilayered composites*. Acta Materialia, 2005. **53**(18): p. 4817-4824.

64. Burger, K., W. Mader, and M. Rühle, *Structure, chemistry and diffusion bonding of metal/ceramic interfaces*. Ultramicroscopy, 1987. **22**(1–4): p. 1-13.
65. Zhukovskii, Y.F., et al., *First principles simulations of 2D Cu superlattices on the MgO(0 0 1) surface*. Applied Surface Science, 2004. **226**(1–3): p. 298-305.
66. Mewes, T., et al., *Comparative study of the epitaxial growth of Cu on MgO and on hydrogen terminated Si*. Surface Science, 2001. **481**(1–3): p. 87-96.
67. Eilers, G. and K. Mukasa, *Surface morphology of thin Cu films grown on magnesium oxide (100)*. Japanese Journal of Applied Physics Part 1-Regular Papers Short Notes & Review Papers, 2000. **39**(6B): p. 3780-3783.
68. Kung, H., et al., *Observation of body centered cubic Cu in Cu/Nb nanolayered composites*. Applied Physics Letters, 1997. **71**(15): p. 2103-2105.
69. Li, H., et al., *Low-energy electron-diffraction and photoemission-study of epitaxial films of Cu on Ag(001)*. Physical Review B, 1991. **43**(8): p. 6342-6346.
70. Hahn, E., et al., *Strain driven fcc-bcc phase transition of pseudomorphic Cu films on Pd(100)*. Physical Review Letters, 1995. **74**(10): p. 1803-1806.
71. Hoagland, R.G., et al., *On the strengthening effects of interfaces in multilayer fee metallic composites*. Philosophical Magazine A, 2002. **82**(4): p. 643-664.
72. Demkowicz, M.J., et al., *Simulation of plasticity in nanocrystalline silicon*. Philosophical Magazine, 2007. **87**(28): p. 4253-4271.

73. Mukherjee, A.K., *An examination of the constitutive equation for elevated temperature plasticity*. Materials Science and Engineering: A, 2002. **322**(1-2): p. 1-22.
74. Wang, Y.C., A. Misra, and R.G. Hoagland, *Fatigue properties of nanoscale Cu/Nb multilayers*. Scripta Materialia, 2006. **54**(9): p. 1593-1598.
75. Demkowicz, M.J., R.G. Hoagland, and J.P. Hirth, *Interface Structure and Radiation Damage Resistance in Cu-Nb Multilayer Nanocomposites*. Physical Review Letters, 2008. **100**(13): p. 136102.
76. Wang, J., et al., *Atomistic simulations of the shear strength and sliding mechanisms of copper–niobium interfaces*. Acta Materialia, 2008. **56**(13): p. 3109-3119.
77. Wang, J., et al., *Atomistic modeling of the interaction of glide dislocations with “weak” interfaces*. Acta Materialia, 2008. **56**(19): p. 5685-5693.
78. Narayan, J., Y. Chen, and R.M. Moon, *Nickel colloids in reduced Ni-doped magnesium-oxide* Physical Review Letters, 1981. **46**(22): p. 1491-1494.
79. Lin, C., et al., *Morphology evolution of thin Ni film on MgO(100) substrate*. Journal of Physics D-Applied Physics, 2002. **35**(15): p. 1864-1866.
80. Choi, Y.C., et al., *Effect of surface morphology of Ni thin film on the growth of aligned carbon nanotubes by microwave plasma-enhanced chemical vapor deposition*. Journal of Applied Physics, 2000. **88**(8): p. 4898-4903.

81. Raatz, G. and J. Woltersdorf, *Structure of metal deposits on ceramic materials studied in the Ni/MgO system*. Physica Status Solidi a-Applied Research, 1989. **113**(1): p. 131-141.
82. McCaffrey, J.P., et al., *Epitaxial variations of Ni films grown on MgO(0 0 1)*. Journal of Crystal Growth, 1999. **200**(3-4): p. 498-504.
83. Svedberg, E.B., et al., *Epitaxial growth of Ni on MgO(002)1x1: surface interaction vs. multidomain strain relief*. Surface Science, 1999. **429**(1): p. 206-216.
84. Reniers, F., et al., *Glow discharge sputtering deposition of thin films of Ag, Cr, Cu, Ni, Pd, Rh and their binary alloys onto NaCl and MgO experimental parameters and epitaxy*. Applied Surface Science, 1996. **92**: p. 35-42.
85. Qiu, H., et al., *Epitaxial growth and characterization of Ni films grown on MgO(001) by biased direct-current sputter deposition*. Journal of Vacuum Science & Technology A, 1994. **12**(5): p. 2855-2858.
86. Lukaszew, R.A., et al., *Annealing effects on (001) Ni films grown on MgO*. Applied Surface Science, 2003. **219**(1-2): p. 74-79.
87. Nielsch, K., et al., *Hexagonally ordered 100 nm period nickel nanowire arrays*. Applied Physics Letters, 2001. **79**(9): p. 1360-1362.
88. Lukaszew, R.A., et al., *Exchange bias on epitaxial Ni films due to ultrathin NiO layer*. European Physical Journal B, 2005. **45**(2): p. 181-184.

89. Krusin-Elbaum, L. and M.O. Aboelfotoh, *Unusually low resistivity of copper germanide thin films formed at low temperatures*. Applied Physics Letters, 1991. **58**(12): p. 1341-1343.
90. Doyle, J.P., B.G. Svensson, and M.O. Aboelfotoh, *Copper germanide Schottky barrier contacts to silicon*. Journal of Applied Physics, 1996. **80**(4): p. 2530-2532.
91. Borek, M.A., et al., *Low resistivity copper germanide on (100) Si for contacts and interconnections*. Applied Physics Letters, 1996. **69**(23): p. 3560-3562.
92. Huang, J.S., et al., *Kinetics of Cu<sub>3</sub>Ge formation and reaction with Al*. Journal of Applied Physics, 1997. **82**(2): p. 644-649.
93. Borek, M.A., et al., *Properties of Cu<sub>3</sub>Ge films for contacts to Si and SiGe and Cu metallization*, in *Advanced Interconnects and Contact Materials and Processes for Future Integrated Circuits*, S.P. Murarka, et al., Editors. 1998. p. 269-274.
94. Aboelfotoh, M.O., M.A. Borek, and J. Narayan, *Interaction of Cu and Cu<sub>3</sub>Ge thin films with Si<sub>1-x</sub>Ge<sub>x</sub> alloys*. Applied Physics Letters, 1999. **75**(12): p. 1739-1741.
95. Aboelfotoh, M.O., et al., *Electrical transport properties of Cu<sub>3</sub>Ge thin films*. Journal of Applied Physics, 1994. **75**(3): p. 1616-1619.
96. Aboelfotoh, M.O., M.A. Borek, and J. Narayan, *Microstructure and electrical resistivity of Cu and Cu<sub>3</sub>Ge thin films on Si<sub>1-x</sub>Ge<sub>x</sub> alloy layers*. Journal of Applied Physics, 2000. **87**(1): p. 365-368.
97. Guizzetti, G., et al., *Optical response of Cu<sub>3</sub>Ge thin films*. Journal of Applied Physics, 1996. **79**(10): p. 8115-8117.

98. Aboelfotoh, M.O., M.A. Borek, and J. Narayan, *Ohmic contact to p-type GaAs using Cu<sub>3</sub>Ge*. Applied Physics Letters, 1999. **75**(25): p. 3953-3955.
99. Aboelfotoh, M.O., et al., *Microstructure characterization of Cu<sub>3</sub>Ge/n-type GaAs ohmic contacts*. Journal of Applied Physics, 1994. **76**(10): p. 5760-5763.
100. Aboelfotoh, M.O., C.L. Lin, and J.M. Woodall, *Novel low-resistance ohmic contact to n-type GaAs using Cu<sub>3</sub>Ge*. Applied Physics Letters, 1994. **65**(25): p. 3245-3247.
101. Hsin, H.-C., et al., *Cu<sub>3</sub>Ge Schottky contacts on n-GaN*. Journal of Materials Science: Materials in Electronics, 2002. **13**(4): p. 203-206.
102. Kumar, D., et al., *LaNiO<sub>3</sub> and Cu<sub>3</sub>Ge contacts to YBa<sub>2</sub>Cu<sub>3</sub>O<sub>7-x</sub> films*. Journal of Electronic Materials, 1996. **25**(11): p. 1760-1766.
103. Peter, A.P., et al., *Selective chemical vapor synthesis of Cu<sub>3</sub>Ge: Process optimization and film properties*. Intermetallics, 2013. **34**(0): p. 35-42.
104. Wu, F. and J. Narayan, *Controlled Epitaxial Growth of Body-Centered Cubic and Face-Centered Cubic Cu on MgO for Integration on Si*. Crystal Growth & Design, 2013. **13**(11): p. 5018-5024.
105. Wu, F., Y.T. Zhu, and J. Narayan, *Grain size effect on twin density in as-deposited nanocrystalline Cu film*. Philosophical Magazine, 2013. **93**(35): p. 4355-4363.
106. Wu, F., Y.T. Zhu, and J. Narayan, *Macroscopic Twinning Strain in Nanocrystalline Cu*. Materials Research Letters, 2014. **2**(2): p. 63-69.

107. Wu F., S.S.R., J.T. Prater, Y.T. Zhu, J. Narayan, *Tuning exchange bias in epitaxial Ni/MgO/TiN heterostructures integrated on Si(100)*. Current Opinion in Solid State & Materials Science, 2014. **under review**.
108. Wu F., Z.J.K., Narayan J., Zhu Y.T. , *Structure and properties of epitaxial Cu<sub>3</sub>Ge films on sapphire* Current Opinion in Solid State & Materials Science, 2014. **under review**.

## Chapter 2

### Background knowledge

#### 2.1 Substrate materials

##### 2.1.1 Si

Single-side polished Si(100) and (111) wafers were used most frequently as the substrates in this project. Silicon is a group VI elemental semiconductor with a diamond structure, which is a union of two superimposed face centered cubic crystal lattices with a displacement of  $1/4$  length of the unit cell in the [111] direction. The lattice constant of Si is  $5.43 \text{ \AA}$ . Each silicon atom forms tetrahedral covalent bonds with its neighbors because it has four valence electrons to share. The band gap of silicon is about  $1.12 \text{ eV}$ , and its thermal expansion coefficient is about  $2.6 \times 10^{-6} \text{ K}^{-1}$  at room temperature.

Thanks to the natural abundance, physical properties and large-scale fabrication ability, Si substrates have been widely used for most commercial electronic devices. Both *n*-type and *p*-type silicon substrates with different doping concentrations are readily available at a low cost. They are also available in large sizes. Consequently the integration of novel structures on silicon substrate holds tremendous promise, both

scientifically and technologically. Before fabrication of epitaxial films on silicon substrates, the native oxide ( $\text{SiO}_x$ ) layer should always be removed to promote formation of crystalline films with controlled microstructures.

### 2.1.2 Sapphire

Sapphire ( $\text{Al}_2\text{O}_3$ ) wafers with different crystallographic orientations are also used as substrates for thin film deposition. Single crystal  $\text{Al}_2\text{O}_3$  is an ionic solid that has a rhombohedral/ hexagonal structure belonging to the space group of  $R3C$ . The close packed planes of oxygen alternate with a hexagonal array of aluminum planes to form the hexagonal unit cell of sapphire. One third of the sites of the hexagonal aluminum planes are vacant, such that the stoichiometric ratio of Al/O in sapphire is 2/3. The aluminum atoms and vacancies have a three-fold symmetry axis along the  $[0001]$  direction. The lattice constants of a hexagonal  $\text{Al}_2\text{O}_3$  unit cell are  $a=4.7587 \text{ \AA}$  and  $c=12.9929 \text{ \AA}$ , respectively. Due to the optical transparency, easy pre-growth cleaning and handling, thermal stability up to  $\sim 1100 \text{ }^\circ\text{C}$ , and low electrical conductivity (insulating at room temperature with a band gap of  $\sim 9 \text{ eV}$ ), sapphire has been commonly used as substrate material for thin film growth and device fabrication in the semiconductor industry, e.g. high-power, high-frequency CMOS integrated circuits, especially for high-power radio-frequency applications. Single-crystal sapphire has also

been commonly used in semiconductor devices, such as blue light-emitting diodes (LED) [1]. The thermal expansion coefficient of sapphire along its a-axis is  $6.2 \times 10^{-6} \text{ K}^{-1}$ , while that along c-axis is  $7.07 \times 10^{-6} \text{ K}^{-1}$ . The termination planes of sapphire substrates are in four different orientations: c-plane (0001), r-plane (1-102), m-plane (1-100), and a-plane (11-20). Figure 2.1 is the schematic illustration of the different crystallographic planes of sapphire.

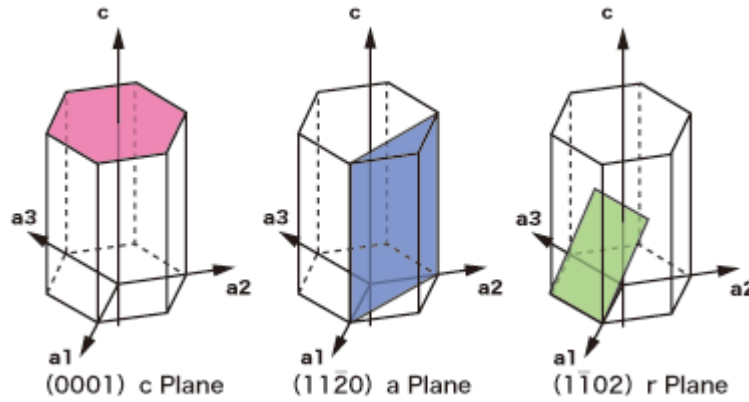


Figure 2.1: The schematic illustration of the different crystallographic planes of sapphire.

## 2.2 Buffer layers

### 2.2.1 Titanium Nitride (TiN)

TiN has been commonly used in various thin film applications. For example, due to its high hardness, good corrosion and erosion resistance, TiN has been used as coatings to increase the wear resistance of punches, metal forming tools and high speed steel cutting tools. Furthermore, TiN coatings have been chosen as diffusion barriers for microelectronic devices, cosmetic gold-colored surfaces, and wavelength selective transparent optical films, taking advantage of its relative inertness, high sublimation temperature, optical and electronic properties. TiN exhibits a metallic character with golden color, which can be further adjusted by doping with zirconium. TiN has a NaCl-type cubic crystal structure with a lattice constant of 4.24 Å. Its vacancy defect structure is stable over a wide composition range ( $0.6 < N/Ti < 1.16$ ). The typical TiN coatings have the following characteristics: (1) High hardness: Hardness Values of 2500-3000 kg/mm<sup>2</sup> in Knoop or Vickers Microhardness measurements are typical for TiN thin films, which is higher than hard chrome or carbide material; (2) Good adhesion: The coating forms a metallurgical bond with the substrate, such that no flake, chip or peeling exists; (3) Low coefficient of friction: TiN films usually have a relatively low coefficient of friction against steels, carbides, ceramics, etc. (4) High thin film uniformity: TiN film conforms uniformly to the substrate. No buildup occurs on corners.

### 2.2.2 Magnesium Oxide (MgO)

Magnesium oxide (MgO) is widely used in applications of electrochemistry, catalysis, and microelectronics. It is also widely used as substrate or buffer material for thin film growth. MgO is close to an ideal insulating ionic solid, because its valence band is controlled by the strong potential of the ionic core [2]. Since the interaction between O and Mg is characterized by ionic force, MgO has a very large bandgap ( $\sim 8$  eV) and is therefore transparent in a wide spectral range from 300 nm to 6000 nm. The melting point of MgO is very high ( $\sim 2800$  °C). Similar to TiN, MgO has a sodium chloride (NaCl) structure with the lattice constant of 4.216 Å. This structure of MgO can be considered as a fcc lattice of  $\text{Mg}^{2+}$  ions, with all the octahedral holes occupied by  $\text{O}^{2-}$  ions, or vice versa. MgO has been widely used as the buffer layer for the thin film growth in the present micro-electronic industry. Numerous materials can be grown epitaxially on MgO, such as metal [3], metal-composite nanoparticles [4], phosphors [5], ferromagnetic materials (nitrides [6], oxides [7]), electro-optic (or ferroelectric) materials [8], semiconductor oxides [9], optical storage materials, superconductive materials, etc. MgO is also a good gate-dielectric for GaN-based MOS diodes. The physical properties of MgO are summarized in table 2.1.

**Table 2.1 Optical properties of MgO**

Transmission Range	Refractive Index	Reflection Loss	Exciton binding energy (meV)	Bandgap (eV)	Absorption Coefficient
0.3 to 6 microns	1.7085 at 2 microns	12.8% at 2 microns	$E_b = 161$	$E_g = 7.9$	$0.05 \text{ cm}^{-1}$ at $5.5 \mu\text{m}$

### 2.3 Thin film epitaxy

Epitaxy originates from two ancient Greek words:  $\epsilon\pi\iota$  (epi-: placed or resting upon) and  $\tau\alpha\chi\iota\varsigma$  (-taxis: arrangement). For the field of thin film, epitaxy means the fabrication of an extended single-crystalline film onto a crystalline substrate. Though this phenomenon was first observed in alkali halide crystal over a century ago [10], the word “epitaxy” was not invented until 1982 by the French mineralogist L. Royer. Homoepitaxy and heteroepitaxy are two large categories for epitaxy. Homoepitaxy refers to the scenario in which the film and the substrate are the same material, such that the lattice parameters of the film and the substrate are the same and no misfit strain/ missing interfacial bonds exist. A typical example is the deposition of epitaxial silicon films on silicon wafers using vapor-phase epitaxy. In contrast, heteroepitaxy involves the deposition of a film onto a substrate with different materials. The growth of novel devices or materials (epitaxial thin films) on commercially available substrate

systems is extremely important technologically. The difference in thermal expansion coefficients and chemistry between the film and substrate, together with the mismatch between the film and substrate lattice parameters determine the structure and properties of heteroepitaxial films.

### **2.3.1 Thin film growth modes**

Thin film growth is a nucleation and growth process including a number of steps, such as deposition, diffusion, bonding and so forth. Figure 2.2 is a schematic illustration showing the major atomic processes: (a) deposition of atoms from the vapor onto the substrate surface or existing clusters; (b) diffusion of adatoms on the surface; (c) nucleation of adatom clusters; (d) addition of mobile adatoms to the existing clusters; (e) dissociation of clusters, and (f) a dynamic equilibrium is reached when the evaporation of the absorbed atoms from substrate surface and the deposition of the atoms from the vapor occur simultaneously.

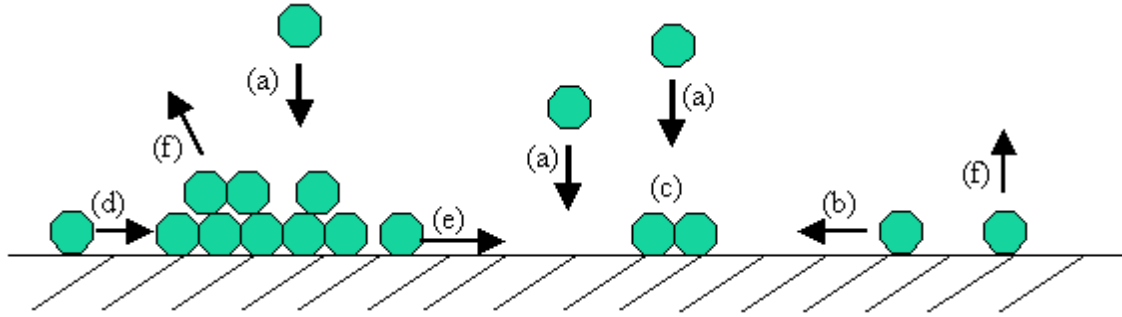


Figure 2.2: A schematic illustration of thin film growth steps: (a) deposition of atoms from the vapor (b) surface movement/ diffusion of the adatoms (c) formation of clusters by nucleation (d) addition of adatoms to existing clusters (e) dissociation of clusters and (f) evaporation.

The film morphology is determined by the growth modes of thin film on substrates. There are three possible modes of crystal growth on surfaces, namely island growth, layer-by-layer growth and a mixture growth mode of the former two modes. To a large degree, film growth mode is following the energy minimization rule in thermodynamics. Three energies (the surface free energy of the substrate ( $\sigma_s$ ), the surface free energy of the film ( $\sigma_f$ ) and the interfacial energy ( $\sigma_{int}$ ) between the film and the substrate) determine the growth mode that a system will take. Generally speaking, when  $\sigma_s = \sigma_f + \sigma_{int}$ , a uniform film will grow on the substrate; when  $\sigma_s < \sigma_f + \sigma_{int}$ , the film will tend to form 3-D islands; when  $\sigma_s > \sigma_f + \sigma_{int}$ , the film will follow a growth mode that is

a mixture of the former two. These three growth modes are discussed in detail as following.

### **(1) Island growth mode (Volmer -Weber or V-W mode)**

V-W mode refers to the growth mode in which small clusters nucleate directly on the substrate surface and then grow into three-dimensional islands. Island growth is a physical mode of deposited film growth and chemical vapor deposition. During deposition, atoms deposited onto a flat surface undergo random walks and meet with each other. They then form an island with a higher mass and a lower random walk velocity. The size and stability of an island will increase as more atoms are deposited on the substrate and bond with the island. A large number of separate islands can form and grow independently. Individual islands will grow to become separate grains in the final film. This mode has been observed in many systems of metals on insulators, including many metals on alkali halides, graphite and other layer compounds such as mica [11]. V-W growth occurs when the deposited atoms are more strongly bonded to each other than to the substrate atoms.

### **(2) Layer-by-layer growth mode (Frank-van der Merwe or F-M mode)**

In F-M mode, small clusters will nucleate and grow into one monolayer in height in the first stage. As the deposition proceeds, the monolayer keeps growing to be a uniform film. In other words, a complete monolayer will form on the substrate surface before the second layer of film is built up. This growth mode has been observed in many

homoepitaxy systems, such as metal on metal, and semiconductor on semiconductor systems. F-M growth occurs when the deposited atoms are more strongly bonded to the substrate than to each other.

### **(3) Layer-by-layer followed by island growth mode (Stranski-Krastanov/SK mode)**

This mode is a mixture of the previous two growth modes. After reaching a few monolayers, 3-D islands begin to form on the uniform film, such that the islands are on a “wetting layer”, rather than directly on the bare substrate surface as in V-W growth mode. S-K mode is commonly observed in heteroepitaxial semiconductor systems with a small lattice mismatch. S-K growth mode can be explained in terms of strain energy. When the strain accumulated in the wetting layer reaches the critical value, it is energetically unfavorable for the system to continue the layer-by-layer growth. The island growth mode can avoid the introduction of misfit dislocations [12-14].

Theoretically, the growth of thin film proceeds in thermodynamic equilibrium and the above three growth modes will occur. In practice, however, the film growth mode will be influenced by kinetic parameters. Two kinetic factors are critical: (1) the density of adatoms, which is controlled by deposition rate; (2) the surface mobility of adatoms, which is influenced by surface temperature. The substrate temperature can result from two sources: either from a local lattice heating by the kinetic energy dissipation and the latent heat of condensation [15] or from substrate heating, if any. Defects, such as

vacancies, steps and kinks, will also affect adatom mobility strongly. They can act as sinks for diffusion atoms, providing them adsorption sites [16].

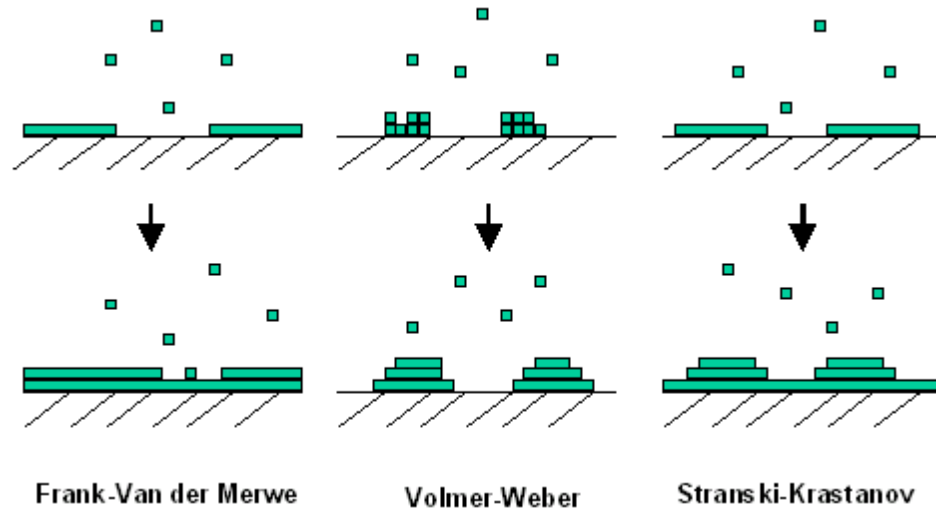


Figure 2.3: Schematic illustration of the three growth modes of thin films: Frank-van der Merwe or layer-by-layer growth, Volmer-Weber or island growth, and Stranski-Krastanov or layer-by-layer followed by island growth.

### 2.3.2 Strain sources

The strains in thin film heterostructures mainly originate from three sources: thermal misfit, lattice misfit, and defect (including dopant/impurity) related strains.

The lattice relaxation will be determined by the combined effect of thermal, lattice, and

defect strains because all of these strains are additive during thin film fabrication process [17]. The three different sources of strains are discussed in detail as following.

### **(1) Thermal misfit strains**

For any thin film fabrication processes that involve deposition at elevated temperatures, the difference in thermal expansion coefficients of the film and the substrate will result to a thermal misfit strain. Specifically, if  $\alpha_f$  (thermal expansion coefficient of the film) is larger than  $\alpha_s$  (thermal expansion coefficient of the substrate), a residual tensile stress will exist in the film after cooling down from the growth temperature to room temperature. In contrast, if  $\alpha_f < \alpha_s$ , a residual compressive stress will exist in the film while the substrate will be under tension.  $\epsilon_T$  (thermal misfit strain) in the film can be calculated as following:

$$\epsilon_T = (\alpha_s - \alpha_f)\Delta T$$

Where  $\Delta T$  is the difference between growth temperature and room temperature, such that  $\Delta T$  is negative during cooling down and positive after heating up [17].  $\sigma_T$  (thermal misfit stress in the film) can be calculated by the following equation:

$$\sigma_T = 2(\alpha_s - \alpha_f)\Delta T \mu_f (1 + \nu_f)/(1 - \nu_f)$$

Where  $\mu_f$  is the shear modulus and  $\nu_f$  is the Poisson's ratio of the film. Thermal strains are usually small and difficult to relax, since the associated critical thickness is large. For scenarios where dislocation nucleation and propagation are not easy, such as in strongly bonded oxide and nitride materials, the relaxation is more difficult. The residual strains accumulate as thickness increases. If the accumulated stress exceeds

the fracture stress, cracking and delamination will happen for tensile strain, while compressive stresses can be managed easier [17].

## **(2) Lattice misfit strains**

The lattice misfit is calculated as:

$$\varepsilon = a_f/a_s - 1,$$

where  $a_f$  and  $a_s$  are lattice parameters of the film and the substrate. If the planar spacing of lattice planes is different for the film and the substrate, the planes of different materials will not align perfectly across the interface, such that lattice misfit strain will arise. Planar misfit is more accurate than lattice misfit because it is the planes that align across the film/substrate interface and play a dominant role during thin film growth [17].

The epitaxial film first grows pseudomorphically [18] to assume the crystalline lattice of the substrate, such that the strain accumulates in the film. As the film thickness increases, the strain energy in the system also increases. Finally, dislocations or missing/extra half planes nucleate and propagate to relieve the misfit strain accumulated in the system.

The dislocations represent either an extra or a missing plane, depending on compressive or tensile strain in the film. The properties of heteroepitaxial films are determined by the crystallographic properties of the substrate and the film, difference

in thermal expansion coefficients and chemistry between the film and substrate [18], among which the lattice misfit between substrate and film plays the key role to control the growth and morphology of the film.

### **(3) Defect related strains**

Defects in thin film heterostructures include dislocations, vacancies, interstitials, clusters and dopants/impurities (for doped and alloyed materials). The defect distribution and lattice relaxation around defects will lead to misfit strains. For example, boron in silicon leads to tensile stress since the dopant size is smaller than that of the host material, while Ge and Sb in Si result in compressive stress. The planar/lattice misfit can be accommodated by defects without misfit dislocations. The defect strains are sensitive to processing variables and growth kinetics, because they determine the location, clustering, and annealing of defects. Chemical strains and stabilization of pseudomorphic metastable phases are also influencing the defect strains [17].

#### **2.3.3 Lattice matching epitaxy**

Traditionally, the relaxation of strains across the interface is explained by the lattice matching epitaxy (LME) mechanism, in which one-to-one matching of the lattice parameters of the film and substrate occurs at the interface. LME requires the unit cells of the film and the substrate to match with each other. As the films grow pseudomorphically on the substrate, the lattice parameters of the film and the substrate

match and strains accumulate. Then after the pseudomorphic growth of the film continues and reaches the critical thickness, the strain energy reaches the critical value to trigger the nucleation of dislocations. The critical thickness is the thickness at which the misfit strain energy stored in the system exceeds the energy of misfit dislocations, such that the system prefers to accommodate dislocations to minimize the free energy. These dislocations nucleate at the film surface and then propagate through the whole film to the film/substrate interface, such that the misfit strain in the film is relieved. The stored strain energy is proportional to the film thickness and smaller than the energy of misfit dislocations below the critical thickness. The critical thickness at which dislocations nucleate is determined by the misfit. When the misfit is small, the critical thickness for dislocation nucleation will be very large, such that dislocation nucleation and strain relaxation may not be possible. The glide of dislocations throughout the film will result to a high density of threading dislocations in the films, which act as charge carrier trap/recombination centers [18] and are detrimental for the device. Figure 2.4 is a schematic illustration of the LME mechanism. It shows the crystalline lattice of the film and the substrate before growth, during pseudomorphic/ coherent growth, and after dislocation nucleation beyond the critical thickness.  $d_c$  stands for the critical thickness in this figure.

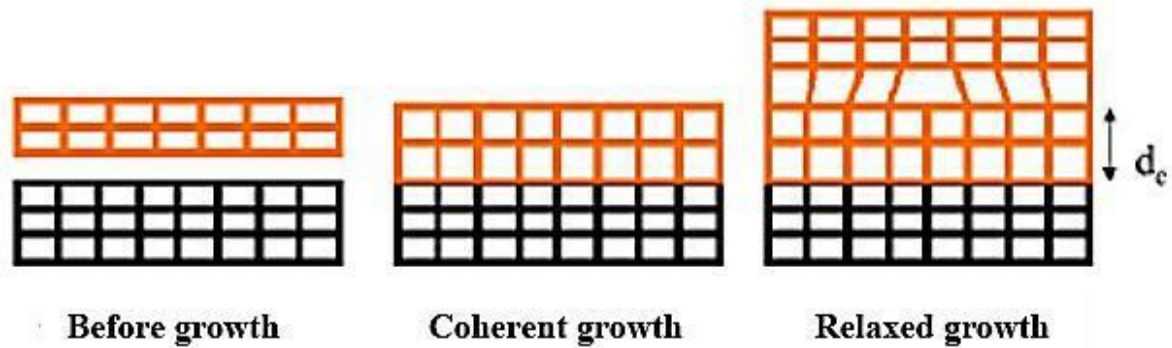


Figure 2.4 Schematic illustration of lattice matching epitaxy [19]

### 2.3.4 Domain matching epitaxy

According to conventional wisdom in LME, thin films will grow as epitaxial single crystals only for systems with a lattice misfit (between the film and the substrate) smaller than 7-8% [20]. If the total misfit exceeded 7%, it was surmised that thin films would turn polycrystalline, with large-angle grain boundaries [20]. However, epitaxial growth was also observed in large misfit systems where the misfit strain was far beyond 7-8% regime, such as TiN/Si [21]. Since the strain across the film/substrate interface is relaxed by dislocations, which are extra/missing half planes in nature, it is the planar matching that leads to LME, rather than LME causing the matching of planes [17]. Dr. Narayan proposed [18, 21] a Domain Matching Epitaxy (DME) framework, taking the dominant role of lattice planes in thin film epitaxy into consideration. In the DME paradigm, the matching of planes can be different in different directions of the

film–substrate interface, and there is one dislocation (missing/extra plane) in each domain. For low misfit conditions, the matching planes for the film and the substrate are the same, such that DME reduces to LME [17]. Figure 2.5 is the schematic illustration of DME. DME is based upon the matching of integral multiples of lattice planes across the film/ substrate interface. When integral multiples of lattice planes match perfectly, then  $md_f = nd_s$ , in which  $d_f$  and  $d_s$  are the planar spacing of the film and the substrate, respectively, and  $m$  and  $n$  are integral numbers. There will be a residual strain ( $\epsilon_r = ((nd_s - md_f)/nd_s)$ ) when the misfit falls in-between the integral multiples. This residual strain will be accommodated by a combination of two different domains that alternate with a certain frequency  $\alpha$ , such that  $(m + \alpha)d_f = (n + \alpha)d_s$ .

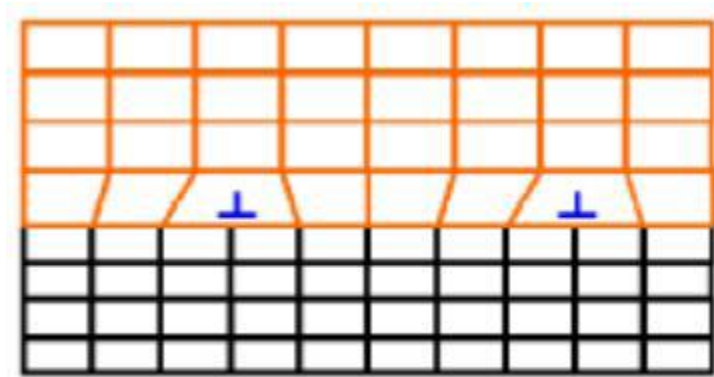


Figure 2.5 Schematic illustration of domain matching epitaxy (DME)[19]

From an atomistic kinetic perspective of growth, the formation and growing of clusters introduce nuclei for dislocations from the very first monolayer for sufficiently large misfit [17, 18], so that the rest of the film can grow strain-free. This is because in large misfit conditions, the critical thickness will be less than a monolayer, and all the dislocations nucleate at the steps present during the initial growth stages. More importantly, these dislocations can be confined to the interface if the initial growth is through 2-D cluster formation. These misfit dislocations can then run out to the edges of the wafer, reducing the number density of threading dislocations significantly [17, 18, 21]. This provides a novel way to relax the misfit strain completely within the first monolayer for high (>7%) misfit systems, by the kinetically controlled introduction of a 2-D array of interfacial misfit dislocations. The critical considerations for thin film epitaxy across the misfit scale, with lattice/planar misfit, thermal and defect strains are summarized as following.

- (1) For small planar misfit strain ( 2% or less), pseudomorphic growth (the film assumes the planar spacing of the substrate) occurs. As the pseudomorphic layer grows thicker, the strain-free energy builds up until the critical thickness, which is determined by the competition between the chemical free energy associated with the pseudomorphic metastable phase and the strain-free energy. The misfit dislocations accommodate the strain between the new phase and the pseudomorphic transition layer, leaving the new phase strain-free.

- (2) For systems with large planar misfit strains ( $\geq 8\%$ ), the critical thickness will be less than a monolayer, such that the film is fully relaxed at growth temperatures. Only thermal and defect strains remain upon cooling. The cooling rate plays a critical role in dislocation nucleation and propagation, defects trapping, etc.. The stress accumulates with thickness [22] until exceeding the fracture stress of the film, and film cracks appear above a critical thickness.
- (3) For intermediate planar misfit strains, critical thickness is several monolayers thick. The residual strains are determined by dislocation nucleation and propagation steps. Thermal strains are usually small (of the order of 0.1–0.2%), such that lattice strains will dominate if they are not relaxed.

#### **2.4 Deformation twinning mechanisms in nanocrystalline fcc materials**

Nanocrystalline (NC) fcc metals are found to deform by twinning more easily, especially in those fcc metals with medium to high stacking fault energy [23]. High strain rate and low temperature generally promote deformation twinning [24-27]. Due to the difficulty in experimental studies of NC materials, early insights on the deformation mechanisms of NC materials were largely obtained by MD simulations [28-32], which predicted several mechanisms for deformation twinning. First of all, deformation twinning was observed to form by emission of Shockley partials from grain boundaries [28-32]. Furthermore, a twin nucleus may form by the overlapping of two extended dislocations on adjacent slip planes [28]. Last but not least, grain boundary

splitting and migration can also generate a coherent twin boundary [28]. Experimental results can validate and add insights to the MD simulations. Early experimental observations were limited to validate MD simulation results, such as emission of partial dislocations from grain boundaries [33-35] and deformation twinning [33-36]. Recently, new phenomena were revealed by experiments, such as twins with reduced macroscopic strain [24, 37] fivefold twins [33, 36], V-shaped twins [67,69], inverse grain size effect on twinning [171], etc. High-resolution transmission electron microscopy (HRTEM), in situ HREM, and X-ray diffraction, and synchrotron/neutron diffraction analysis are major experimental tools to study deformation twinning, among which HRTEM is most frequently used because it provides direct evidence of twins with atomic resolution. In situ HRTEM is relatively difficult, and the image quality needs to be improved. X-ray analysis is also used to analyze the twin boundary density in NC materials [38, 39], but it is usually qualitative and the absolute value of twin boundary density is not precise.

MD simulations and experimental investigations have their own advantages. For example, MD simulations often use relatively uniform grain sizes, while experimental samples usually have a wide grain size distribution. Experimental techniques have much lower spatial and temporal resolutions than MD simulations, and it is difficult to experimentally observe defect evolutions in real time. Therefore, it is ideal to combine experiments and MD simulations for investigation of the deformation process of NC

materials. Based on experimental observations and MD simulation results, several twinning mechanisms have been proposed for NC fcc materials [23].

#### **2.4.1 Twinning by partial emission from grain boundaries**

MD simulations first predicted [28] and HRTEM [40, 41] verified the formation mechanism of deformation twins by emission of Shockley partials from grain boundaries. Shockley partials need to be emitted from the grain boundaries on successive slip planes to form the twins. This twinning mechanism is most commonly observed in NC fcc metals and alloys [28, 42, 43], making it scientifically important to understand the emission mechanism of partials from the grain boundary. Partial dislocations can readily emit from non-equilibrium grain boundary to nucleate a deformation twin [42] but nucleation of a partial on every slip plane is difficult due to the required high energy barrier. The partial multiplication mechanism at the grain boundary supplying a twinning partial on every slip plane has been proposed by Zhu et al. [40]. Two dislocation reaction and cross-slip mechanisms have been proposed. These mechanisms involve the emission of partials either with the same Burgers vector or with two different Burgers vectors, producing a twin with smaller shear strain.

#### **2.4.2 Twinning by overlapping of stacking fault ribbons**

MD simulations [28] first predicted the nucleation of deformation twins by overlapping of two stacking fault ribbons. A twin nucleus with a thickness of two atomic

planes can be formed by the dynamic overlapping of two extended partial dislocations with stacking faults (SF) on adjacent slip planes. Adding more SFs on either side of the twin can increase its thickness, but no deformation twins of this type have been reported to be thicker than two layers [23]. It depends on the incidental overlapping of other slipping dissociated dislocations with stacking fault ribbons to grow, but a continuous growth mechanism is lacking. The overlapping of a dissociated dislocation with a SF connected with the grain boundary [42] is a variant of this twinning mechanism. If the leading partial of the dissociated dislocation reaches the grain boundary, the twin nucleus will be identical to a twin nucleus generated by emission of two Shockley partials from the grain boundary. Non-equilibrium grain boundaries provide high possibilities for this mechanism to function, e.g. high density of dissociated partials with one end on the grain boundary has been observed in NC Ni with non-equilibrium grain boundaries [42].

### **2.4.3 Twinning with macroscopically low strain**

Deformation twins in NC fcc metals have the highest macroscopic strain if formed by partials with the same burger vector. If the partials have different Burgers vectors, the macroscopic strain will be lower [23]. Different mechanisms have been proposed for deformation twins with low or even zero macroscopic strain [23]. Random activation of partials (RAP) [24] were proposed as one mechanism for twinning with zero macroscopic strains. The RAP mechanism involves three Shockley partials with

different Burgers vectors. The three partials with different orientations will produce the same stacking sequence shifts, such that if the three partials propagate in equal number of times one after another, no net macroscopic strain will accumulate. Since the three partials can not be driven simultaneously by a global shear stress, the changing local shear stresses were proposed to be the driving source [24]. These local stress variations can differ from the global shear stress significantly and promote the random emission of partials. The locations for high local stress concentration include the edge of a stacking fault [43], triple junctions, and grain boundary steps.

A global strain is necessary to relieve the global stress. It is worth noting that though at the grain level, no direct contribution to the macroscopic deformation is from the RAP twins, they indirectly contribute to grain boundary sliding and grain rotation (bulk deformation) by favorably reorienting the crystal lattice, changing the applied resolved shear stresses on slip systems. The applied stress and the accumulated energy are distributed locally by the RAP twinning, and their Burgers vectors add up to zero macroscopic strain, without violating laws of thermodynamics. Note that the RAP twins form only if the numbers of three partials are about the same. There will be macroscopic strain in the twinned grain if this condition is not met. The magnitude of the strain is determined by the relative numbers of the three partials.

#### **2.4.4 Sequential twinning mechanism**

The sequential twinning mechanism by emissions of Shockley partials from grain/twin boundaries was proposed to explain multifold twins, e.g. fivefold twins [44]. The first step of this mechanism is the formation of a simple twin by partial dislocation emissions from grain boundaries. The second step starts with the emission of a  $90^\circ$  Shockley partial from grain boundaries. The partial glides on a  $\{111\}$  slip plane toward the twin boundary. When a  $90^\circ$  Shockley partial reaches the twin boundary, it becomes equivalent to another new  $90^\circ$  partial on another  $\{111\}$  plane. The gliding of this new partial moves the twin boundary up/downward by one atomic plane. When a series of Shockley partials emit from the grain boundary successively on adjacent  $\{111\}$  planes, and convert to a new partial that glides away, the regular twin will be converted into a threefold twin. Repetition of this process leads to the formation of fourfold and fivefold twins.

#### **2.4.5 Twinning by grain boundary splitting and migration**

This twinning mechanism was first proposed by Ashby and Harper in 1967, then got verified by the MD simulation [32] and experimental observation [45]. A twin lamella can be formed by the migration of non-crystallographic segments, which are the new twin boundary. The boundaries of twin lamellae formed at different time frames can join together to form a zigzag boundary.

#### **2.4.6 Partial multiplication at twin boundaries**

The source of partial dislocations on consecutive  $\{111\}$  slip planes is the major issue in the formation of deformation twins in NC fcc metals. The partial multiplication mechanisms discussed in Section 2.4.1 and the RAP mechanism discussed in Section 2.4.3 are two mechanisms of partial multiplication by dislocation reaction at grain boundaries. There are more mechanisms for partial multiplication at twin boundaries to form single and multiple twins in a self-sustained way [46].

#### **2.4.7 Dislocation rebound mechanism**

Dislocation rebound mechanism was also proposed [47] for the formation of single and multiple twins. The elastic field of a partial dislocation is reflected at grain/twin boundaries [47], and an opposite-sign dislocation may nucleate under the reverse shear field, especially when the dislocation velocity is close to the sound velocity [46, 47]. Single twin, and V/T/X-shaped twin can form via this dislocation rebound mechanism [46]. The rebound mechanism is deliberated in the following sections.

### **2.5 Grain size effect on deformation twinning**

Smaller grain sizes have been reported to be less favorable for twin nucleation for coarse-grained (CG) materials [48]. However, when the grain size further decreases (less than 100 nm), deformation twinning has been frequently observed even in

materials with medium to high stacking fault energies such as copper and nickel [23]. Therefore, twinning is one of the major plastic deformation mechanisms of NC materials [29, 30, 49, 50].

It was reported that the number of grains containing twins first increases and then decreases, while the number of grains containing stacking faults increases monotonically for NC fcc Ni [51]. Since the fraction of twinned grains is a good statistical indicator of twinning propensity, the twinning propensity first increases and then drops with decreasing grain size. The decrease of twinning propensity with decreasing grain size is called the inverse grain-size effect [51], which was verified by synchrotron and neutron diffraction, and also observed in NC Cu [52]. This suggests that it is a common phenomenon in NC fcc metals, since Cu has a lower stacking fault energy and very different general planar fault energies (GPFE) from the Ni. Zhu et al. [53, 54] proposed an analytical model, which successfully predicted the grain size effect. GPFE makes it more difficult to activate a twinning partial than to activate the first partial to form stacking fault, such that no inverse grain-size effect exists for stacking faults.

## **2.6 General planar fault energy effect on deformation twinning**

Stacking fault energy (SFE) is traditionally considered to be the major intrinsic material property that affects the twinning propensity. Recent studies, such as molecular dynamics (MD) simulations, phase field simulation, and experimental

observations, reveal that the SFE can not be the only reason for the observed twinning behavior. GPFEs should be taken into consideration for deformation processes mediated by partial dislocations [25, 49, 55, 56]. In NC fcc metals, the GPFE curves describe the energy change of rigidly shifting two semi-infinite crystals on glide plane ( {111} plane) along a  $\langle 112 \rangle$  direction [55]. Ab initio approach [57] is the most accurate way to calculate the GPFE curves, while the errors come from boundary conditions and simulation code. GPFE curves involve three important energies: stacking fault energy ( $\gamma_{sf}$ ), unstable stacking fault energy ( $\gamma_{usf}$ ), and unstable twin fault energy ( $\gamma_{utf}$ ). After a stacking fault is generated by a leading partial, the nucleation and gliding barrier for the trailing partial is a function of the difference between unstable stacking fault energy and SFE ( $\gamma_{usf} - \gamma_{sf}$ ). If the difference is large, some first partials will slip without trailing partial, generating stacking faults. Twinning may then be possible if the unstable twin fault energy is not much higher than the unstable stacking fault energy. The GPFEs have been used to explain the differences in deformation mechanisms of NC Al, Ni and Cu with a small grain size of 12 nm [55].

## References

1. Bianchi, M.P., *Gallium nitride collector grid solar cell*, 2002, Google Patents.
2. Canney, S.A., et al., *Electronic band structure of magnesium and magnesium oxide: experiment and theory*. Journal of Physics-Condensed Matter, 1999. **11**(39): p. 7507-7522.
3. Narayan, J., et al., *Formation of epitaxial and textured platinum films on ceramics-(100) MgO single crystals by pulsed laser deposition*. Applied Physics Letters, 1994. **64**(16): p. 2093-2095.
4. Kang, K., et al., *(001) oriented FePt-Ag composite nanogranular films on amorphous substrate*. Applied Physics Letters, 2003. **82**(19): p. 3284-3286.
5. Jeong, J.H., et al., *Enhanced green emission in ZnGa<sub>2</sub>O<sub>4</sub>:Mn thin film phosphors by Se doping*. Applied Physics Letters, 2003. **83**(7): p. 1346-1348.
6. Loloee, R., K.R. Nikolaev, and W.P. Pratt, *Growth and characterization of sputtered epitaxial  $\gamma'$ -Fe<sub>4</sub>N and NbN films and bilayers using electron backscatter diffraction patterns and magnetometry*. Applied Physics Letters, 2003. **82**(19): p. 3281-3283.
7. Kale, S.N., et al., *Magnetism in cobalt-doped Cu<sub>2</sub>O thin films without and with Al, V, or Zn codopants*. Applied Physics Letters, 2003. **82**(13): p. 2100-2102.
8. Tayebati, P., D. Trivedi, and M. Tabat, *Pulsed laser deposition of SBN:75 thin films with electro-optic coefficient of 844 pm/V*. Applied Physics Letters, 1996. **69**(8): p. 1023-1025.

9. Ogale, S.B., et al., *Deposition of copper oxide thin films on different substrates by pulsed excimer laser ablation*. Journal of Applied Physics, 1992. **72**(8): p. 3765-3769.
10. M. Ohring, ed. *The Materials Science of Thin Films*,. 1992, Academic Press: Boston.
11. Venables, J.A., G.D.T. Spiller, and M. Hanbucken, *Nucleation and growth of thin-films*. Reports on Progress in Physics, 1984. **47**(4): p. 399-459.
12. Eaglesham, D.J. and M. Cerullo, *Dislocation-free Stranski-Krastanow growth of Ge on Si(100)*. Physical Review Letters, 1990. **64**(16): p. 1943-1946.
13. Tersoff, J. and F.K. LeGoues, *Competing relaxation mechanisms in strained layers*. Physical Review Letters, 1994. **72**(22): p. 3570-3573.
14. Christiansen, S., et al., *Reduced effective misfit in laterally limited structures such as epitaxial islands*. Applied Physics Letters, 1995. **66**(5): p. 574-576.
15. Shen, J., Z. Gai, and J. Kirschner, *Growth and magnetism of metallic thin films and multilayers by pulsed-laser deposition*. Surface Science Reports, 2004. **52**(5-6): p. 163-218.
16. Koch, R., *The intrinsic stress of polycrystalline and epitaxial thin metal films*. Journal of Physics-Condensed Matter, 1994. **6**(45): p. 9519-9550.
17. Narayan, J., *Recent progress in thin film epitaxy across the misfit scale (2011 Acta Gold Medal Paper)*. Acta Materialia, 2013. **61**(8): p. 2703-2724.
18. Narayan, J. and B.C. Larson, *Domain epitaxy: A unified paradigm for thin film growth*. Journal of Applied Physics, 2003. **93**(1): p. 278-285.

19. Gopinath R Trichy, *Growth, characterization and magnetic properties of epitaxial iron-platinum nanostructures*, in *Materials Science and Engineering* 2008, North Carolina State University Raleigh.
20. Frank, F.C. and J.H. Vandermerwe, *One-dimensional dislocations. 1. static theory*. Proceedings of the Royal Society of London Series a-Mathematical and Physical Sciences, 1949. **198**(1053): p. 205-216.
21. Narayan, J., et al., *Epitaxial growth of TiN films on (100) silicon substrates by laser physical vapor deposition*. Applied Physics Letters, 1992. **61**(11): p. 1290-1292.
22. Sharan, S. and J. Narayan, *Strain relief mechanisms and the nature of dislocations in GaAs/Si heterostructures*. Journal of Applied Physics, 1989. **66**(6): p. 2376-2380.
23. Zhu, Y.T., X.Z. Liao, and X.L. Wu, *Deformation twinning in nanocrystalline materials*. Progress in Materials Science, 2012. **57**(1): p. 1-62.
24. Wu, X.L., et al., *New Deformation Twinning Mechanism Generates Zero Macroscopic Strain in Nanocrystalline Metals*. Physical Review Letters, 2008. **100**(9): p. 095701.
25. Wu, X.L., Y. Qi, and Y.T. Zhu, *Partial-mediated slips in nanocrystalline Ni at high strain rate*. Applied Physics Letters, 2007. **90**(22): p. 221911.
26. Meyers, M.A., O. Vohringer, and V.A. Lubarda, *The onset of twinning in metals: A constitutive description*. Acta Materialia, 2001. **49**(19): p. 4025-4039.

27. Meyers, M.A., A. Mishra, and D.J. Benson, *Mechanical properties of nanocrystalline materials*. Progress in Materials Science, 2006. **51**(4): p. 427-556.
28. Yamakov, V., et al., *Dislocation processes in the deformation of nanocrystalline aluminium by molecular-dynamics simulation*. Nat Mater, 2002. **1**(1): p. 45-49.
29. Schiotz, J., F.D. Di Tolla, and K.W. Jacobsen, *Softening of nanocrystalline metals at very small grain sizes*. Nature, 1998. **391**(6667): p. 561-563.
30. Van Swygenhoven, H., P.M. Derlet, and A. Hasnaoui, *Atomic mechanism for dislocation emission from nanosized grain boundaries*. Physical Review B, 2002. **66**(2): p. 024101.
31. Yamakov, V., et al., *Length-scale effects in the nucleation of extended dislocations in nanocrystalline Al by molecular-dynamics simulation*. Acta Materialia, 2001. **49**(14): p. 2713-2722.
32. Yamakov, V., et al., *Deformation twinning in nanocrystalline Al by molecular-dynamics simulation*. Acta Materialia, 2002. **50**(20): p. 5005-5020.
33. Liao, X.Z., et al., *Deformation twinning in nanocrystalline copper at room temperature and low strain rate*. Applied Physics Letters, 2004. **84**(4): p. 592-594.
34. Chen, M.W., et al., *Deformation twinning in nanocrystalline aluminum*. Science, 2003. **300**(5623): p. 1275-1277.
35. Liao, X.Z., et al., *Deformation mechanism in nanocrystalline Al: Partial dislocation slip*. Applied Physics Letters, 2003. **83**(4): p. 632-634.

36. Liao, X.Z., et al., *Nanostructures and deformation mechanisms in a cryogenically ball-milled Al-Mg alloy*. Philosophical Magazine, 2003. **83**(26): p. 3065-3075.
37. Wu, F., Y.T. Zhu, and J. Narayan, *Macroscopic Twinning Strain in Nanocrystalline Cu*. Materials Research Letters, 2014. **2**(2): p. 63-69.
38. Zhao, Y.H., et al., *Tailoring stacking fault energy for high ductility and high strength in ultrafine grained Cu and its alloy*. Applied Physics Letters, 2006. **89**(12): p. 121906.
39. Zhao, Y., et al., *High Tensile Ductility and Strength in Bulk Nanostructured Nickel*. Advanced Materials, 2008. **20**(16): p. 3028-3033.
40. Zhu, Y.T., et al., *Twinning partial multiplication at grain boundary in nanocrystalline fcc metals*. Applied Physics Letters, 2009. **95**(3): p. 031909.
41. Zhu, Y.T., X.Z. Liao, and X.L. Wu, *Deformation twinning in bulk nanocrystalline metals: Experimental observations*. JOM, 2008. **60**(9): p. 60-64.
42. Wu, X.L. and Y.T. Zhu, *Partial-dislocation-mediated processes in nanocrystalline Ni with nonequilibrium grain boundaries*. Applied Physics Letters, 2006. **89**(3): p. 031922.
43. Wang, J. and H. Huang, *Shockley partial dislocations to twin: Another formation mechanism and generic driving force*. Applied Physics Letters, 2004. **85**(24): p. 5983-5985.

44. Zhu, Y.T., X.Z. Liao, and R.Z. Valiev, *Formation mechanism of fivefold deformation twins in nanocrystalline face-centered-cubic metals*. Applied Physics Letters, 2005. **86**(10): p. 103112.
45. Liao, X.Z., et al., *Deformation twins in nanocrystalline Al*. Applied Physics Letters, 2003. **83**(24): p. 5062-5064.
46. Zhu, Y.T., et al., *Formation of single and multiple deformation twins in nanocrystalline fcc metals*. Acta Materialia, 2009. **57**(13): p. 3763-3770.
47. Dregia, S.A. and J.P. Hirth, *A rebound mechanism for Lomer dislocation formation in strained layer structures*. Journal of Applied Physics, 1991. **69**(4): p. 2169-2175.
48. Fu, H.H., D.J. Benson, and M.A. Meyers, *Analytical and computational description of effect of grain size on yield stress of metals*. Acta Materialia, 2001. **49**(13): p. 2567-2582.
49. Asaro, R.J. and S. Suresh, *Mechanistic models for the activation volume and rate sensitivity in metals with nanocrystalline grains and nano-scale twins*. Acta Materialia, 2005. **53**(12): p. 3369-3382.
50. Shan, Z., et al., *Grain Boundary-Mediated Plasticity in Nanocrystalline Nickel*. Science, 2004. **305**(5684): p. 654-657.
51. Wu, X.L. and Y.T. Zhu, *Inverse Grain-Size Effect on Twinning in Nanocrystalline Ni*. Physical Review Letters, 2008. **101**(2): p. 025503.

52. Zhang, J.-Y., et al., *Double-inverse grain size dependence of deformation twinning in nanocrystalline Cu*. Physical Review B, 2010. **81**(17): p. 172104.
53. Zhu, Y.T., et al., *Nucleation and growth of deformation twins in nanocrystalline aluminum*. Applied Physics Letters, 2004. **85**(21): p. 5049-5051.
54. Zhu, Y.T., et al., *Nucleation of deformation twins in nanocrystalline face-centered-cubic metals processed by severe plastic deformation*. Journal of Applied Physics, 2005. **98**(3): p. 034319.
55. Van Swygenhoven, H., P.M. Derlet, and A.G. Froseth, *Stacking fault energies and slip in nanocrystalline metals*. Nature Materials, 2004. **3**(6): p. 399-403.
56. Hu, S., C.H. Henager Jr, and L. Chen, *Simulations of stress-induced twinning and detwinning: A phase field model*. Acta Materialia, 2010. **58**(19): p. 6554-6564.
57. Siegel, D.J., *Generalized stacking fault energies, ductilities, and twinnabilities of Ni and selected Ni alloys*. Applied Physics Letters, 2005. **87**(12).

## Chapter 3

### Experimental Techniques

In this chapter, experimental methods used to fabricate, deform and characterize the metallic thin film heterostructures are demonstrated. Pulsed laser deposition (PLD) technique was the only approach to fabricate metallic thin films in the present study. The deformation of the as-grown thin film heterostructures were conducted by tensile test facilities. The morphology and film quality were first characterized by optical microscope (OM) and scanning electron microscope (SEM). Then X-ray diffraction (out-of-plane) was performed as the structural characterization method of the thin film heterostructures. More detailed microstructure study and defect analysis were performed by transmission electron microscopy (TEM) and high-resolution transmission electron microscopy (HRTEM). A brief description of each relevant experimental technique is given in this chapter.

#### 3.1 Substrate Preparation

In the present study, Si (100)/(111), sapphire and coarse-grained Cu sheets were used as substrates for thin film growth. During transportation and storage, organic impurities and dust particles may stick onto the substrate surface, and then discourage the nucleation and epitaxial growth of thin films on substrates. Therefore before the

thin film deposition process, substrate cleaning is of great importance. The thickness of Cu and Si substrates were  $\sim 1500$  and  $\sim 500$   $\mu\text{m}$ , respectively. To remove dust particles and organic impurities, the substrates were agitated for 10 minutes in an ultrasonic bath using acetone. Subsequently, the substrates were rinsed and vapor-cleaned in acetone and then with methanol to further remove the organic impurities. Finally, the substrates were dried by high-purity nitrogen over the surface. HF was used in some cases to remove the native oxidation layer on the substrate surface. After cleaning, the substrates were immediately loaded into the pulsed laser deposition chamber to decrease contamination. The substrates were mounted onto the substrate heater using a fast drying silver paste to provide a good thermal contact.

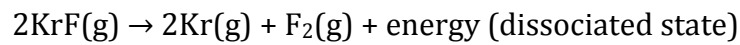
### **3.2 Pulsed Laser Deposition (PLD)**

The term LASER is an acronym for “light amplification by stimulated emission of radiation”. Generally, a laser source generates coherent light in a narrow low divergent beam, with a well-defined wavelength. Therefore, lasers can be focused and directed effectively for material processing. The peak power of most commercial lasers is inversely correlated with the duration of the laser pulse. Since ablation of most materials requires very high energy densities, typically nanosecond/femtosecond-lasers are used for pulsed laser deposition. PLD is a non-equilibrium physical vapor deposition (PVD) technique for thin film growth. It has been widely used for the fabrication of a variety of thin film heterostructures, such as metals, oxides and nitrides

[1]. PLD adopts a high-powered laser, focuses it on a target so that the target material interacts with the laser. After the interaction, the material is evaporated locally and a highly energetic plasma is formed [2, 3], which is referred to as laser ablation. A plume is formed in the direction normal to the target surface, due to the ejection of the ablated material. The material in this plume is deposited on the substrate when it reaches the substrate surface. PLD technique was the only method employed in the present study to fabricate metallic thin film heterostructures. The laser, the vacuum chamber and the optics that control the laser are the most important three components in the PLD system.

Nd:YAG [4, 5] and the excimer laser [6, 7] are the most important lasers used for PLD. Nd:YAG is a solid state neodymium-doped yttrium aluminum garnet laser, whose fundamental frequency is 1064 nm. If the fundamental wavelength is doubled, tripled or quadrupled, it can be changed to 532 nm, 355 nm and 262 nm. Since high energy densities with high energy photons can be delivered by excimer lasers, they are most frequently used for PLD. The emission wavelength of excimer lasers are determined by the gas composition in the laser chamber. For PLD technique, ArF (193 nm) and KrF (248 nm) excimer lasers are most frequently used. An excimer laser (sometimes more correctly called an exciplex laser) is a form of ultraviolet laser, commonly used in micromachining, eye surgery, and the production of microelectronic devices. The term excimer is a short form of excited dimer. Lasing action in these systems is activated by the population inversion between a repulsive ground state and a bound excited state.

Induced by an electric discharge, inert gas forms temporarily bound molecules with the halide or themselves to form the excited state. Then by means of stimulated emission, the excited state gives up its energy to form the dissociated ground state molecules. The process happens within picoseconds, and results in a population inversion between the ground and excited state molecules. For KrF excimer laser, the lasing process can be depicted by the following equations:



### 3.2.1 Laser-solid interaction mechanism

The underlying physics for a PLD system is a complicated process, involving the laser-solid interaction, creation and expansion of the plasma. Based on the interaction of the laser with the target material, the laser ablation process at energy densities above the threshold for vaporization can be divided into three stages [3]:

**1): Evaporation:** the laser beam interacts with the target material, resulting in evaporation of the surface layers.

**2): Plume formation:** after the surface layers get evaporated, the laser beam interacts with the evaporated material to form a high-temperature isothermal expanding plasma

plume. This process initiates with the evaporation of the target material and continues until the end of the pulse.

**3): Plume expansion:** when the laser pulse terminates, the plume has an anisotropic three-dimensional adiabatic expansion, resulting to the characteristic forward nature of the plume.

The three stages are discussed in details as follows:

**1): Evaporation (initial interaction between laser and target):**

The electromagnetic energy of the laser excites free electrons in the target material, when a laser beam hits the target. The target material then evaporates due to the thermal energy generated by the electron-phonon coupling. The reaction time for this process to occur is on the order of picoseconds [3]. The target must be suitably prepared for a better laser-solid coupling. High roughness, high absorption coefficient and low reflectivity are typical features contributing to an efficient laser-solid coupling, which lowers the threshold energy for vaporization. Typical values of threshold energy vary from 0.11 to 0.40 J/cm<sup>2</sup> [8], depending on the laser wavelength and the surface roughness of the target. The energy deposited by the laser beam are consumed as the conduction heat loss in the target, the energy loss due to laser absorption by the expanding plasma and energy required to evaporate the target material. Therefore the

thickness of the target for which evaporation ( $\Delta X_t$ ) takes place can be calculated based on the energy balance [3, 8]:

$$\Delta X_t = (1-R) (E-E_{th}) / (\Delta H + C_v \Delta T)$$

In which R is the reflectivity,  $E_{th}$  is the threshold energy,  $\Delta H$  is the latent heat,  $C_v$  is the volume heat capacity and  $\Delta T$  is the maximum rise in temperature. For most metallic and semiconducting targets, the validation condition for this equation is that the thermal diffusion length  $(2Dt)^{0.5}$  is larger than the light penetration depth ( $L = 1/\alpha_t$ ) [3]. (D is thermal diffusion constant, t is laser pulse duration,  $\alpha_t$  is the absorption coefficient). For non-metallic targets with low thermal diffusivities, evaporation depth mainly depends on the attenuation distance of the laser beam [8] and thermal diffusivity does not play an important role.

## **2): Plasma formation and initial isothermal expansion:**

A surface temperature in the range of 2000-3200 K will be generated by the laser interaction with the target material. Positive ions and electrons are emitted from the free surface due to this high temperature. The formation of a plasma extending normal to the target surface is happening together with the ablation of the target. Charged and neutral species of atoms and molecules comprise the plasma and interact with the incoming laser, resulting to temperatures higher than the vaporization temperature in the plasma. The electron-ion collisions lead to absorption of laser energy by the plasma. An inverse Bremsstrahlung process involving absorption of a photon by a free electron

is the major reason for absorption[9]. The absorption coefficient ( $\alpha_p$ ) of the plasma can be calculated as follows:

$$\alpha_p = 3.69 \times 10^8 (Z^3 n_i^2 / T^{0.5} \nu^3) [1 - \exp(-h\nu/KT)]$$

In which Z is the average charge,  $n_i$  is the ion density, T is the temperature of the plasma, h is Planks constant, K is the Boltzmann constant and  $\nu$  is the free energy of the laser light. The laser light will be heavily absorbed close to the target surface, where the density of the ionized species is high, since the absorption coefficient ( $\alpha_p$ ) is proportional to  $n_i^2$ . In this region, evaporated particles are continuously injected into the plasma, a dynamic self-regulating equilibrium exists between the rapid transfer of thermal energy into kinetic energy (due to injection of evaporated particles of the target into the plume) and the plasma absorption coefficient. These compensating mechanisms result in the isothermal temperature obtained by the plasma near the target surface [3]. In contrast, the leading edge of the plume consists of low densities of electrons and ions with high expansion velocities, consequently transparent to the laser beam. The  $[1 - \exp(-h\nu/KT)]$  term considers the losses due to stimulated emission depending on the plasma temperature and laser wavelength [3]. Impact ionization, thermal ionization, photo ionization, and electronic ionization are processes that affect the extent of ionization of the laser generated species.

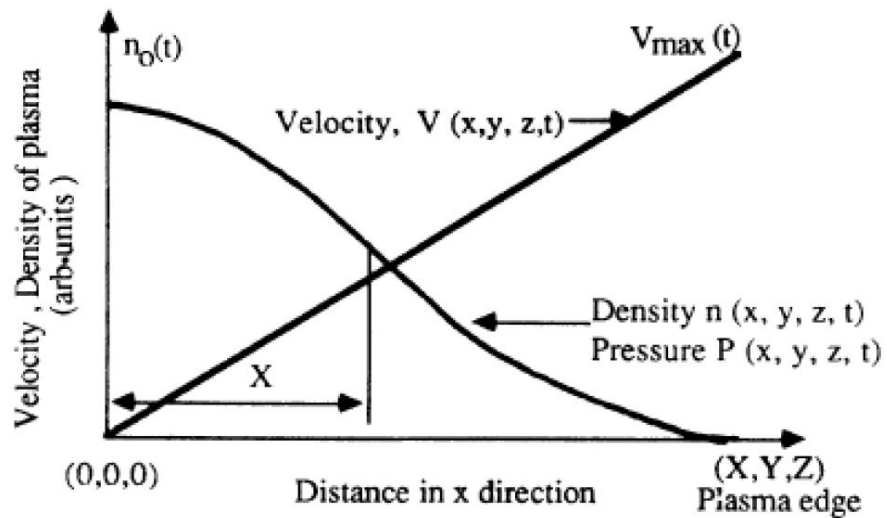


Figure 3.1 Schematic illustration demonstrating the variation of the density ( $n$ ), pressure ( $P$ ), and velocity ( $V$ ) as a function of distance away from the target surface.

The variation of pressure, density and velocity as the function of distance from the target surface perpendicular to it is summarized Figure 3.1 [3].  $X$  axis stands for the direction perpendicular to the target surface. The particle density in the plasma close to the surface is an approximated Gaussian function. The velocity of particles near the target is minimum, while the density of particles is maximum. During the initial interaction stages the velocity of the particles is low but their acceleration is relatively high. Sequentially, when the expansion velocity increases, the acceleration decreases and eventually reaches zero. This is the reason for the elongated shape of the plasma.

The initial dimensions of the plasma are larger in the transverse direction when compared to the longitudinal direction.

### **3): Plume expansion (adiabatic expansion of the plasma):**

The plasma plume expands adiabatically into the vacuum after the plasma formation and isothermal expansion. As soon as the laser pulse terminates, the adiabatic expansion of the plasma begins. During this regime the laser is no longer being absorbed by the plume, and there is no injection of particles from the target into the plume as well. Since the thermal energy has been converted to kinetic energy, the expanding plasma is associated with very high velocities. There is a balance between energy gain from recombination of ions in the plasma, and cooling due to expansion. The loss in thermal energy leads to a drop in temperature, determined by the balance. The developing shape of the plume in the adiabatic regime is schematically illustrated in Figure 3.2.

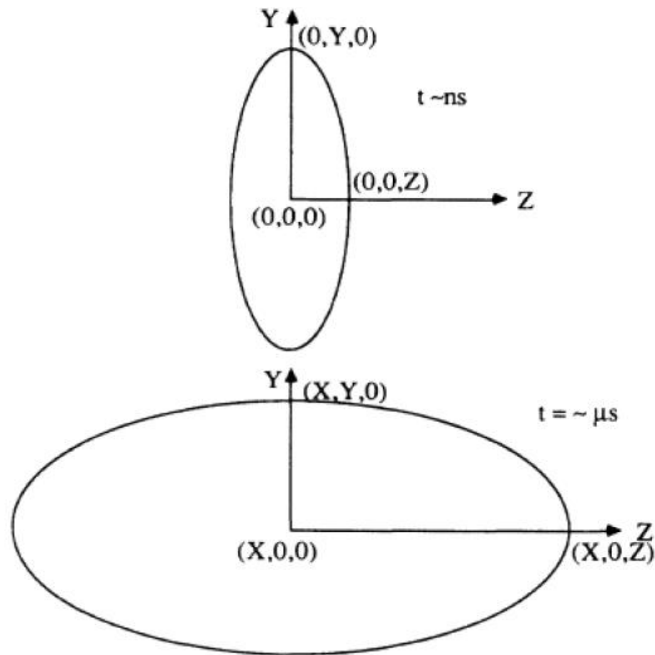


Figure 3.2: (a) Schematic illustration of the plasma shape right after the laser pulse terminates. (b) Final shape of the plasma when it hits the substrate.

The initial dimension of the plasma along the longitudinal  $x$  direction is minimal. In contrast, the initial dimensions of the plume along transverse directions ( $y$  and  $z$ ) are larger. The transverse dimensions are on the order of a few millimeters, while along the longitudinal direction it's only about 20-100 microns. At first the plasma is elliptically shaped with  $y$  axis being the major axis. Then the longitudinal  $x$  dimension expands rapidly during the adiabatic expansion stage, resulting in the characteristic PLD plume. The plasma pressure drops rapidly and most of the thermal energy is converted to kinetic energy. Then the plasma elongates in the shorter dimension because the plume

has no more energy for expansion. Eventually, the plume is still elliptical-shaped, but z dimension turns to be the major axis.

### **3.2.2 Advantages of PLD**

Due to the high energy of the ablated species, PLD turns to be a popular thin film deposition technique with several advantages. The energy of the ablated species can be as high as 10 to 100 eV, while for thermal or e-beam evaporation techniques, the energy of the ejected species is about 0.1 eV at 1200 K. Some advantages of PLD technique is listed as following:

1. The PLD-grown films are relatively contamination free since PLD is a clean process. The energy source, which is the laser, is placed outside of the deposition system. The vacuum chamber has no filaments and other sources of contamination, such that the interaction between the laser and gas species in the vacuum chamber is minimal. The spatial confinement of laser-solid interaction also renders PLD a clean process.
2. Complex metastable phases can be fabricated by PLD, since PLD is a highly non-equilibrium process and the plume has high energy. These phases are difficult to be obtained by other equilibrium evaporation techniques.
3. It's easy to use PLD to fabricate multi-layered heterostructures. Multiple (up to 6) targets can be mounted onto the target carousel simultaneously and easily

- manipulated, such that multi-layered films can be produced without breaking the vacuum.
4. High-quality epitaxial films can be produced by PLD at lower temperatures, thanks to the high energy of the plume. Some important nitrides, such as epitaxial TiN, can be routinely fabricated on Si (100) by PLD at 600 °C[10], while temperature as high as 900 °C is required for CVD growth of TiN.
  5. The fabricated film by PLD will have a very similar stoichiometry with that of the target material for multi-component systems. The material ablation from the target is too fast to be affected by the vapor pressures of individual components, due to the high energy density of the laser. Furthermore, the forward directed nature of the plume also helps to reproduce the stoichiometry of the target.
  6. The growth rate of the as-deposited film can be controlled by the repetition rate of the laser. By controlling the impingement rate, the nucleation site density can be increased to a level much higher than those formed in MBE or sputter deposition technique. The increasing number of nucleation sites will contribute to better films with uniform thickness and improved smoothness.
  7. PLD is conceptually easy to understand and any material can be used as a target, as long as its absorption coefficient is large enough for the laser.

### 3.2.3 Drawbacks of PLD

PLD also suffers from some disadvantages. The mostly noticed drawbacks of PLD are listed below:

1. Small sample size: the area of a typical PLD-grown sample is only about 1 cm<sup>2</sup>, which makes it not suitable as a large-scale manufacturing tool for industries.
2. Non-uniformity in film thickness: for large substrates, the film thickness has a  $\cos n\theta$  type of thickness dependence, where  $n \sim 8-12$ . This results from the forward directed nature of the plume.
3. Formation of chunks during ablation: chunks are large particulates or globules of molten material that can be detrimental to film quality [8]. Various mechanisms including exfoliation, subsurface boiling, and expulsion of the liquid layer by shock wave recoil are involved in improper ablation, which leads to the formation of these undesirable chunks [3, 8].

Various methods can be used to make up for these drawbacks. By rastering the laser beam over a large target and/or rotation/translation of the substrate, uniformity of film thickness can be achieved to some extent and the scale of the sample size can be increased [11]. For chunk control, increasing the absorption coefficient and thermal conductivity of the target material is a possible approach. The size and number of chunks can also be minimized to some extent [8] by careful adjustment of the laser

parameters. A compact target with better cohesion of the grains will also contribute to fewer chunks.

### 3.3 X-Ray Diffraction

X-ray diffraction (XRD) is one of the important nondestructive characterization techniques used to provide sample information, such as the phase composition, the crystal structure and orientation of solids, lattice parameter, grain size, defects, and lattice strain, etc.. For diffraction to occur, the incident wave should have a wavelength close to the repeat distance of a periodic structure. The atomic distances of crystals are usually on the order of a few angstroms, therefore X-rays are used to study the crystallographic information since they have wavelengths of the same order. When a monochromatic X-ray beam with a wavelength  $\lambda$  and an incidence angle  $\theta$  interacts with a periodic lattice structure, diffraction occurs either constructively or destructively, depending on the path difference. There will be sharp XRD peaks corresponding to the set of specifically oriented planes when constructive diffraction occurs. This criterion is the basic mechanism of XRD technique and is referred to as Bragg's law [12]:

$$2d \sin\theta = n\lambda$$

Where  $d$  is the inter-planar spacing,  $\theta$  is the incident angle,  $n$  is an integer indicating the order of reflection, and  $\lambda$  is the wavelength of the X-ray beam. For

structural analysis using X-ray of known wavelength  $\lambda$ , we can determine the spacing  $d$  of various planes in the crystal by measuring  $\theta$ . The diffraction peaks are characteristic to the material and the crystal structure (e.g. the shape and size of the unit cell), which determines the diffraction pattern and the relative intensities of different peaks. The relative intensity of the diffracted beam can be written as

$$I = |F_{klm}|^2 P [(1-\cos \nu)/\sin^2\theta \cos\theta]$$

Where  $P$  is the multiplicity factor that represents the relative proportion of the planes contributing to the same reflection. The whole term in the square brackets is the Lorentz polarization factor.  $F$  is the structure factor of the crystal, representing the complex amplitude of the electromagnetic field scattered by one unit cell of the crystal. Structure factor has the general expression of the form

$$F_{klm} = \sum f_n \exp\{2\pi i(hx_n + ky_n + lz_n)\}$$

Where  $f_n$  is the atomic scattering factor,  $x_n$ ,  $y_n$ , and  $z_n$  are the coordinates of the  $n^{\text{th}}$  atom in the unit cell. The equation is suitable for any specific lattice and structure factor  $F$  is related to the symmetric properties of the unit cell.

The common experimental methods of XRD include Laue method, rotating-crystal method, moving-film method, powder method and X-ray diffractometer, which is widely used for the characterization of thin films. Three common measurement strategies are adopted in the diffractometer method to detect the intensity of the diffracted x- ray beam:

1. Both the crystal and the detector are fixed.

2. Only the detector is fixed at the appropriate  $2\theta$  angle, while the crystal is rotated slowly through its reflecting range about the detector axis ( $\omega$  scan).
3. Both the crystal and the detector are rotated through the diffractometer axis ( $\omega$ ,  $2\theta$  scan) and suitably coupled for each reflection.

In the present work, a Rigaku D-MAX/A diffractometer with Cu  $K\alpha$  radiation is used for  $\theta$ - $2\theta$  scans. This instrument is a two-circle diffractometer, in which the sample can be rotated along one of the axis ( $\theta$ -axis) and the detector can be rotated independently ( $2\theta$ -axis), based on Bragg-Brentano parafocusing diffraction geometry. In this geometry, the angles between the incident beam and the detector and the sample surface are  $2\theta$  and  $\theta$ , respectively. The normal to sample surface, the incident beam, and the detector are all in the same plane. This diffractometer geometry can only be used to get diffraction information from the planes parallel to sample surface, due to the restricted rotation of the sample merely along  $\theta$ -axis. Another reason is that the diffracted beam always lies in the same plane containing the incident beam and plane normal.

## **3.4 Transmission Electron Microscopy**

### **3.4.1 Introduction**

Transmission electron microscopy (TEM) is a microscopy technique in which a beam of electrons is transmitted through an ultra-thin specimen, interacting with the

specimen as it passes through. TEM allows detailed micro-structural morphology examination through high-magnification, high-resolution imaging. It also enables the study of orientations, chemical compositions, and crystal structures in areas of interest through x-ray, electron diffraction, and electron-energy analysis. TEM is the most powerful tool to identify the Burgers vector for a dislocation and to investigate defects, such as stacking faults, twins, grain boundaries, interstitial atoms, vacancies and precipitates, etc.

### **3.4.2 Basic operating principles**

TEM utilizes electromagnetic lenses to focus and direct an electron beam. After the electron beam passes through the sample, data is generated and collected.

According to the classic Raleigh criterion for image resolution:

$$\delta = 0.61 \lambda / \beta$$

in which  $\delta$  is the resolution,  $\lambda$  is the wavelength and  $\beta$  is the semi-angle of collection of the magnifying lens, the resolution of a microscope is directly related to the wavelength ( or the energy) of the radiation. The shorter the wavelength, the better the resolution is. This is why TEM chooses electron beam as the radiation source, instead of a light beam. According to de Broglie's theory of the wave-particle duality, the wavelength  $\lambda$  of a particle is determined by its momentum  $p$ :

$$\lambda = h/p$$

In which  $h$  is the Planck's Constant. Since  $p$  is determined by the accelerating voltage  $V$  of the electron microscope,  $\lambda$  can be expressed as following:

$$\lambda = h/(2m_0eV)^{0.5}$$

Where  $m_0$  is the rest mass of electron and  $e$  is the electron charge. For a TEM operating at 200 KV, the electron beam will have a wavelength as small as 0.03 Å. Hence the resolution of a TEM is at atomic level (i.e. on the order of few angstroms). However, the real resolution of TEM is also limited by equipment defects, such as spherical aberration, chromatic aberration, and stigmatism etc..

Electron guns are used to generate the source radiation. After a beam of electrons is generated, it is then focused into a tight, coherent beam by multiple electromagnetic lenses and apertures. To maintain the electron beam undisturbed, the TEM column always needs to be kept at high-vacuum conditions. Any vacuum leakage should be avoided at any cost for the normal operation of TEM. The stray electrons are eliminated by the lens system, during the focus process. After the focused electron beam hits the sample, information is produced due to the interaction of the incoming electron beam and the sample. The information from the transmittal electrons can then be collected by various techniques. For example, a fluorescent screen is used to form an image, which is then recorded on photographic film or with a CCD camera linked to a computer.

Figure 3.3 shows the important components of a TEM. The illumination system and image system are the two critical components of A TEM. The illumination system takes the electrons from the source and transfers them to the sample in the form of

either a broad beam or a focused beam. The image system utilizes the combination of apertures and magnetic lens for taking the electrons that are scattered from the specimen to form the final image or diffraction patterns on the screen.

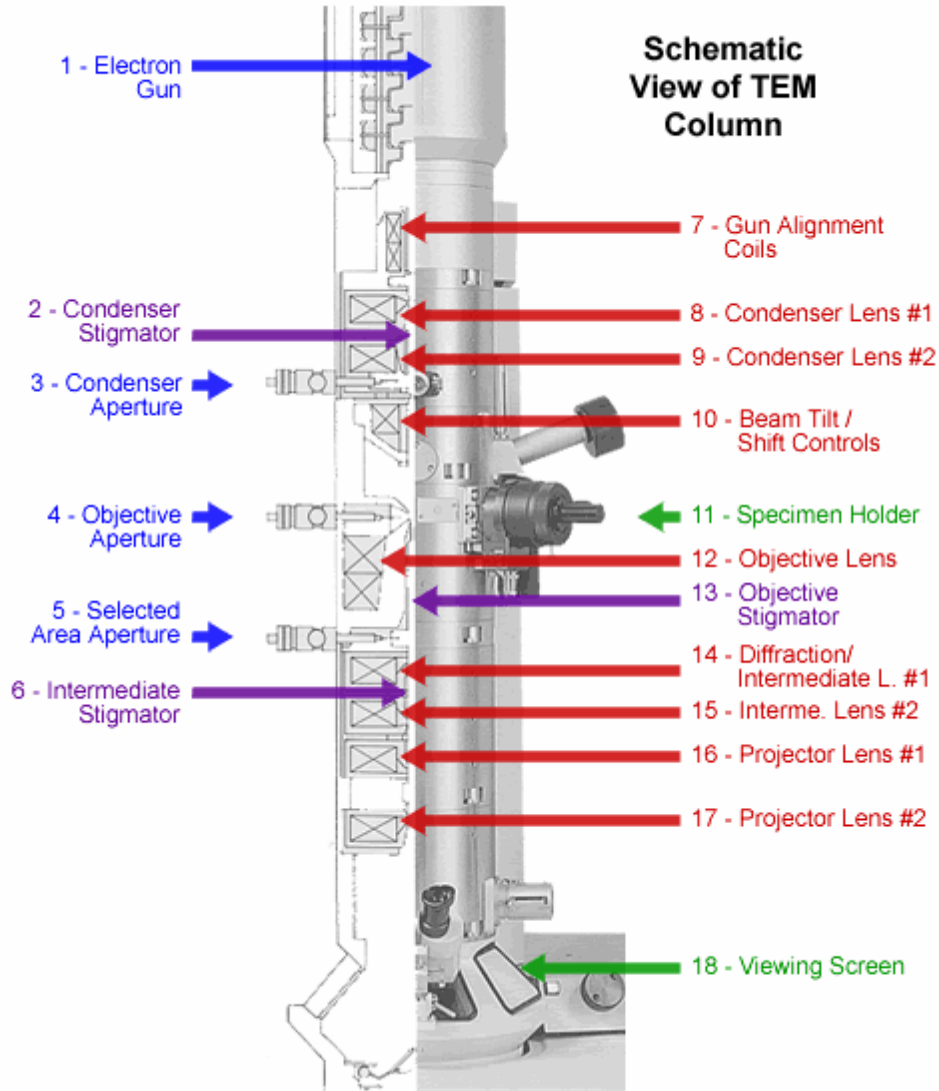


Figure 3.3: Schematic view of the TEM column

### **3.4.3 TEM Sample preparation**

A wide range of solid-state materials, (e.g. metals, minerals, ceramics, polymers, biological Materials etc.) can be analyzed by TEM successfully. TEM samples need to meet the following two requirements: 1): The thickness of the sample should be small enough for electrons to penetrate without excessive energy loss (i.e. electron transparent). 2): The TEM sample should be representative of the original specimen in any respects, including structure and composition. Any form of artifacts, contamination, secondary deformation or heat treatment should be avoided.

TEM sample preparation from an arbitrary material is very difficult. For a typical metal, ceramic, or semiconductor specimen, the prepared TEM sample should be less than 100 nm thick for a 200 kV electron beam to penetrate. More demanding, the TEM sample should have a large electron-transparent thin area, be robust enough to be easily handled, and be flat. There are three typical approaches to prepare TEM samples for a wide variety of possible materials.

#### **a) Site-specific TEM specimens by focused ion beam (FIB) milling**

FIB is a very useful tool for the preparation of site-specific TEM specimens. Typical examples are the examination of a particular region, such as the microstructure of the crack tip in fracture and fatigue experiments, the deformation area around a nanoindentation, an integrated circuit, etc.. A typical FIB uses a gallium ion beam, originating from a liquid metal ion source. This ion beam is then accelerated and rastered over the specimen's surface to perform the site-specific milling. Modern FIBs

have both electron and ion beam (dual-beam) columns, gas-injection systems (GIS) and an Omniprobe for imaging and ion-beam sectioning of a thin lamella.

The typical TEM sample preparation by FIB consists of the following steps: (1) identification of the area of interest; (2) adjustment of the specimen to eucentric height; (3) platinum bar (length  $\sim 15\ \mu\text{m}$ , breadth  $\sim 2\ \mu\text{m}$  and thickness  $\sim 2\ \mu\text{m}$ ) deposition using GIS (the thickness is controlled by deposition time); (4) ion milling with gallium ions at  $\sim 30\ \text{kV}$  to create a lamella structure under the platinum coating; (5) lift-out of the lamella using an Omniprobe, (6) attachment of the lamella onto the TEM grid by welding with platinum; (7) final thinning of the lamella to the thickness of  $\sim 150\text{-}200\ \text{nm}$ , with a low energy gallium beam (at  $5\ \text{kV}$  or lower) to decrease the damage by high-voltage milling.

Although FIB is an efficient approach to prepare site-specific TEM specimen, it has some drawbacks compared to other sample preparation techniques: (1) gallium ions are heavier and more energetic than the argon ions used in PIPS, such that implantation damage of the sample is more severe than that in PIPS; (2) low energy gallium ion beam imaging is difficult to handle due to its bad contrast; (3) artifacts including droplets, curtaining effects on the milled surfaces etc. can appear, due to the ion beam damage. Consequently, the FIB-prepared specimen can be further cleaned in a PIPS with low-energy argon ions for several minutes, using single modulation mode of operation. Since the ion beam sputters the surface, electron beam imaging is always preferred and ion beam imaging is only for taking snapshots when necessary. A careful bonding

between the lift-out lamella and the copper grid with platinum is also important, because the lamella can be lost during handling or cleaning in the PIPS.

## **b) Mechanical Preparation**

Compared with the FIB method, the mechanical preparation approach is more time-consuming. The mechanical preparation usually involves a combination of the following steps:

### **(1) Preparation of slices:**

Epitaxial films grown on (001) silicon or GaAs can be cleaved using a diamond cutter along  $\langle 110 \rangle$  directions. The cleaving is performed on a clean flat surface, from the side of the substrate. The specimens are sliced into small rectangular pieces (length  $\sim 10$  mm, breadth  $\sim 2.5$  mm) and then cleaned with acetone and methanol.

### **(2) Preparation of sandwich structures:**

A sandwich structure is prepared by bonding two slices, with the films facing each other, by a fast-curing epoxy. The epoxy is applied to the surface of the multilayers, and the sandwich structure is held with pressure to obtain good mechanical bonding between the slices. The epoxy layer should be thin enough for a good bonding. Hence epoxy is only applied on one piece, and then a gentle sliding of the two pieces with respect to each other helps spread the epoxy on the second piece.

### **(3) Mechanical polishing:**

Mechanical polishing produces flat and smooth surfaces from large objects. It is used to reduce specimen thickness, such that they can be further processed by other

techniques. The objective is to obtain a flat scratch-free surface with minimum mechanical damage. This process is based on the mechanical action of abrasion. The friction of grains of a material harder than the object to be polished enables precise removal of material. It is necessary to use a fluid as both a lubricant and a cooling agent. The specimen is fixed on a heavy mounting block (metal cylinder), either mechanically locked or held with glue or wax. The specimen holder is held and pressed by hand or rubs against the rotating abrasive disc under its own weight. A counterweight fitted arm can be used to adjust the rubbing force applied to the specimen for commercial automatic machines. A lubricant flow is necessary all over the plate to reduce heat produced by friction and eliminate wastes. Polishing begins with a coarse abrasive and then carries on gradually with finer abrasive grains, which produces a surface of decreasing roughness with homogeneous erosion. An optical microscope must be used to locate residual scratches and to check the polish quality, during these successive steps. Rotation speed, abrasive, penetration force and polishing time can be controlled to minimize mechanical damage.

(4)           Dimpling:

Dimpling is performed to reduce the thickness of the disc in the central portion, in order to decrease the time for ion beam thinning and to obtain large regions with electron transparent thicknesses. Dimpling can be performed either on one side or both sides of the disc. A dimple grinder is needed for dimpling. The sample mount can be fixed onto a magnetic turntable of the dimple grinder, which rotates at a constant but

adjustable speed. A grinding wheel rotates with variable speeds, orthogonal to the rotation of the turntable. The dimple grinder has an in-built micrometer and dial indicator to set up the depth of the dimple and also to examine the progress of the dimpling with the help of a light microscope. It has two cross-wires and their intersection point is aligned using a calibration port. The disc is then positioned at the center of the cross-wires. After centering, the point of contact between the grinding wheel and the disc will be on the axis of rotation of the disc. A small quantity of diamond paste is spread on the disc with a toothpick. Both the wheels are then switched on and the wheel is slowly lowered on to the specimen. After a couple of minutes, the wheel is raised to exam the formation of the dimple. The diamond paste should always spread as a film on the grinding wheel during the process. Otherwise, the grinding wheel directly touches the disc and physically rubs the sample, resulting in mechanical damage. Once the dimple of a desired depth is obtained, the dimpling process should be stopped. The grinding wheel is then replaced with a polishing wheel. A few drops of alumina polishing suspension are applied on the disc and the dimple is buffed for final polishing. This process can last for 5 minutes. To further reduce the time for ion beam thinning, the second surface of the sample can be dimpled. The singlesided dimpled disc is wax-bonded to the specimen mount with the dimpled surface facing it. The centers of dimples on both surfaces are to be matched in order to reduce the thickness of the disc effectively. The important parameters that control the dimpling

rate of a sample are: counterweight, particle size of the diamond paste, and rotation speed of the arm-wheel.

(5) Ion milling:

Ion milling is a sputtering process in which energetic neutral atoms and ions from a cathode hit on the disc at a small angle, knocking off the atoms of the sample. The goal of ion milling is to obtain electron transparent regions from the dimpled discs. The important parameters controlling the thinning rate are beam current, incidence angle, energy and nature of the bombarding ions, and nature of the sample. Ion milling usually takes several hours, due to a thinning rate on the order of a few  $\mu\text{m}/\text{hour}$  for optimal conditions. A precision ion polishing system (PIPS) is used for ion beam thinning. High purity argon gas is used as the ion source. Artifacts can be introduced, if the sample is heat-sensitive, because the continuous transfer of kinetic energy of neutrals/ions to the sample disc may introduce heat. The heating effect can be minimized by employing the ion beam modulation feature in which the sample is not exposed to the ion beam continuously, or by cooling the specimen using a liquid nitrogen stage. For PIPS, the disc is loaded in a holder and ion milled with typical conditions as follows: 1) gun angles:  $4^\circ$  for planar specimens and  $\pm 4^\circ$  for cross-sectional specimens; 2) voltage: 4.5 kV initially; and final polishing at 2 kV for 5 minutes. Further polishing at low kV ( $\sim 0.1\text{-}0.2$  kV) can be used to reduce the amorphous layers on the specimen's surface.

### **c) Suspension method for powder samples**

Powder samples are generally prepared by suspension in a liquid. The suspension is dropped onto a mounting grid, which disperses the powder across it. The solvent, which is unreactive with the sample material, evaporates and leaves the powder ready for investigation. Methanol and Acetone are two such solvents commonly used.

#### **3.4.4 Operation Mode**

In TEM there are two important systems: (i) the illumination system that controls the electron source (intensity) and (ii) the imaging system that collects the electrons scattered and transmitted from the sample. TEM can be operated in two basic modes: imaging and diffraction. Depending on the operation mode the electrons collected by the imaging system can either form a diffraction pattern or an image. The two modes of operation of TEM are:

- (1) Image mode, in which a TEM image is observed as a magnified image of a specimen;
- (2) Diffraction mode, in which an electron beam diffraction pattern is focused at the back focal plane of the objective lens, and then projected onto the screen by the imaging lens system and observed. This mode is sometimes referred to as the selected area electron diffraction (SAED) mode.

The switching between image and diffraction mode is achieved by changing the strength of the intermediate lens.

## Imaging Modes

The diffraction pattern of an amorphous specimen consists of diffuse rings, whereas a crystalline specimen generates diffraction spots. These spots are formed due to the constructive interference between the diffracted beams at Bragg condition. Depending on the different diffraction spots contributing to the image formation, bright-field (BF) or dark-field (DF) images can be obtained. TEM image contrast comes from the scattering of the incident electron beam by the specimen. Since the change of the electron wave can be in amplitude and phase, two types of contrasts exist: amplitude contrast and phase contrast. Amplitude contrasts consist of two principal ways, one is mass-thickness contrast and the other one is diffraction contrast. These contrasts are based on the number of the scattering atoms along the propagation direction of the electron beam and the scattering cross-section of the atomic species in the specimen. BF and DF imaging are the two basic ways to form amplitude-contrast images. For example, in BF images, strongly scattering regions of the specimen (heavy elements, large thickness) show darker contrast than weakly scattering regions (light elements, small thickness). Mass-thickness contrast occurs due to the incoherent elastic scattering of electrons. This type of contrast is important if a non-crystalline sample is observed. Diffraction contrast occurs due to the coherent elastic scattering at Bragg angles. Phase contrast is very sensitive to many factors such as small change in thickness, orientation, scattering factor of specimen and variations in the focus of the objective lens. This sensitivity is also the reason that phase contrast can be used to

image the atomic structure of thin specimens. To form a phase-contrast image, one needs to select more than one beam. Generally, the higher the resolution of image is required, the more beams need to be collected. Consequently three imaging methods have been developed for TEM: Bright Field, Dark Field and High-Resolution Imaging.

### **Bright-field imaging**

Bright field imaging mode is the most common mode of operation for TEM. In this mode, the contrast is formed directly by occlusion and absorption of electrons in the sample. In order to examine samples in bright-field, the objective aperture must be inserted. The objective aperture is a metal plate with holes of various sizes machined into it. The aperture is inserted into the back focal plane, the same plane at which the diffracted image is formed. The back focal plane is located just below the sample and objective lens. When the aperture is inserted, it only allows the electrons in the transmitted beam to pass and contribute to the resulting bright field image. Regions with a larger thickness or a higher atomic number will appear dark, while regions with no sample in the beam path will appear bright – hence the term "bright field". A BF image is formed by selecting only the direct beam, using the objective aperture, which is inserted in the back focal plane of the objective lens. For BF imaging, scattering and diffraction contrast can be produced with objective apertures  $\alpha_0$  ranging from 5 to 20 mrad.

## **Dark-field imaging**

In BF imaging, the unscattered beam is combined with the deflected beams to form the final image. As smaller objective lens apertures are used to eliminate more of the deflected electrons, contrast will increase. If the objective aperture is moved off axis, only the scattered electrons are selected by the aperture while the unscattered electrons are now eliminated. This is a crude form of dark field illumination, since the scattered electrons pass through the objective lens on off-axis trajectories, which worsens the chromatic aberration and the image quality. This problem can be solved by tilting the illumination system, such that the primary beam hits the specimen at an angle. Now the objective aperture can be normally centered, but accept only the scattered, on-axis electrons. The image is produced by electrons scattered into an on-axis cone of aperture. Asymmetries in the dark-field image can be avoided by swiveling the direction of tilt around a cone, or conical illumination can be produced by introducing an annular diaphragm in the condenser lens. DF micrographs usually need a longer exposure time because scattered electrons are less.

Applications of DF imaging include the identification of defects in crystals. It is possible to determine not only the position of defects, but also the type of defects by carefully selecting the orientation of the sample. If the sample is orientated in a way that a particular plane is only slightly tilted away from the strongest diffracting angle, any distortion of the crystal plane that locally tilts the plane to the Bragg angle will produce strong contrast variations.

## **High-Resolution Imaging**

Crystal structure can also be investigated by High Resolution Transmission Electron Microscopy (HRTEM), also known as phase contrast. When utilizing a Field emission source, the images are formed due to the differences in phase among the various electron beams scattered by the sample in order to produce contrast. Image contrast is defined in terms of the difference in intensity between the two adjacent areas. Image formation is given by the complex modulus of the incoming electron beams. Consequently the image is not only dependent on the number of electrons hitting the screen, making direct interpretation of phase contrast images more complex. This effect can be used to provide more information about the sample, such as in complex phase retrieval techniques.

## **Diffraction Mode**

The diffraction phenomenon is based on the diffraction of the electron beam to certain angles by a crystalline lattice. By changing the strength of magnetic lenses, the back focal plane of the objective lens coincides with the object plane of the projector lens, such that a magnified representation of the diffraction pattern is then produced on the fluorescent screen. For single crystalline samples, a diffraction pattern consists of a series of dots, dependent upon the orientation of the specimen. The central bright spot represents non-scattered rays while the peripheral spots represent rays scattered at various angles. The distances from the bright central spot to the scattered spots are inversely proportional to the spacings of different crystalline lattice planes. A crystal

with small lattice spacings will diffract the electrons to greater angles, and thus generate spots far from the central spot. Based on the position at which the diffraction spots appear and the observed image symmetries, information including the crystal's orientation to the beam path and the space group symmetries in the crystal can be obtained. In specimens containing crystals of unknown composition, the diffraction technique may be used to measure the spacing of the atomic crystalline lattice and to determine the composition of the crystal, since different crystals have unique spacings of their lattices. For the case of a polycrystalline material, the diffraction pattern will consist of a series of rings.

In summary, bright-field, dark-field, and high-resolution TEM images provide microstructural information such as dislocations, stacking faults, twins, precipitates, second phase, grain and domain boundaries, and film/substrate interfaces. Electron-diffraction patterns provide crystallographic information of the specimen areas from several nanometers to several microns.

#### **3.4.5 Astigmatism, beam shift and tilt**

While only off-axis object points appear asymmetric for conventional glass lenses, electron lenses are truly asymmetric. They show astigmatism for all object points. This astigmatism can be corrected by means of a stigmator. Instead of one point focus, an astigmatic electron lens forms two line foci perpendicular to each other. A cylindrical lens acts as an astigmatism corrector with its axis at a right angle to the inherent defect

of the astigmatic lens. It brings the rays to a common focus. Therefore an astigmatic electron lens behaves like the combination of a spherical and a cylindrical lens. An electron beam passing a homogeneous magnetic field perpendicularly is deflected from its original axis. The total deflection angle  $\theta$  is called Beam Tilt. A combination of two beam tilts in opposite direction results in a Beam Shift. The total beam shift distance is determined by the distance of the beam tilt coils. A perpendicular combination of two beam tilt coils allows for simultaneous deflection in two planes.

#### **3.4.6 Scanning transmission electron microscope (STEM)**

A scanning transmission electron microscope (STEM) is one kind of TEM, because the electrons pass through a sufficiently thin specimen. However, STEM is different from conventional TEM by focusing the electron beam into a narrow spot, which is then scanned over the sample in a raster. The rastering of the beam across the sample makes STEM suitable for various analysis techniques such as annular dark-field imaging (ADF), electron energy loss spectroscopy (EELS) and energy dispersive X-ray (EDX) spectroscopy. With the addition of EELS, elemental identification, electronic structure determination and chemical bonding detection of atomic columns are possible. The low-angle inelastically scattered electrons used in EELS complements the high-angle scattered electrons in ADF images, allowing the simultaneous detection of both signals. The simultaneous detection of these signals allows direct linkage between image and

quantitative data. One appealing feature of STEM is the directly interpretable z-contrast atomic resolution image where the contrast is directly related to the atomic number, by utilizing a STEM and a high-angle detector. In contrast, the conventional HRTEM uses phase-contrast, producing atomic resolution images that need simulation to interpret. A STEM can be modified from a conventional TEM by adding scanning coils, detectors and circuitry. The addition of an aberration corrector to STEM enables the utilization of electron probes with sub-angstrom diameters, which makes the identification of individual atom columns with unprecedented clarity possible. The high-energy convergent electron beam in STEM provides local information of the sample, even down to atomic dimensions.

### **3.5 Magnetic characterization**

Magnetic properties of the as-deposited samples were characterized using superconducting quantum interference device (SQUID) magnetometer, which is very sensitive and used to measure extremely subtle magnetic fields as low as  $5 \times 10^{-18}$  T with a time span of a few days. The noise levels are as low as  $3 \text{ fT} \cdot \text{Hz}^{-1/2}$  [13], while a typical refrigerator magnet produces  $10^{-2}$  T. SQUID is based on superconducting loops involving Josephson junctions (also known as “weak link”), which is a superconducting ring with a small portion replaced by a thin insulating layer such that electrons can

tunnel through. Due to its high sensitivity, SQUID is one of the most commonly used characterization techniques for nanostructured magnetic materials.

In this project, both traditional magnetization curves at varied temperatures and zero-field-cooling (ZFC)/field-cooling (FC) magnetization curves were obtained. For ZFC and FC magnetization curves, the samples in zero magnetic field need to be first cool down from room temperature to 10 K. ZFC curve is then obtained by applying a small magnetic field of 50 Oe to the sample and measuring the magnetization when the temperature is increased step by step back to room temperature. Sequentially at the same small field (50 Oe), the samples were cooled to 10 K again, while the magnetization was measured as a function of temperature, generating the FC curve.

## References

1. D. B. Chrisey, G.K.H., ed. *Pulsed Laser Deposition of Thin Films*. 1994, Wiley-Interscience: New York.
2. Eason, R., ed. *Pulsed laser deposition of thin films : applications-led growth of functional materials*. 2007, Wiley-Interscience: New York.
3. Singh, R.K. and J. Narayan, *Pulsed-laser evaporation technique for deposition of thin films: Physics and theoretical model*. *Physical Review B*, 1990. **41**(13): p. 8843-8859.
4. Chen, M.Y. and P.T. Murray, *Deposition and characterization of sic and cordierite thin films grown by pulsed laser evaporation*. *Journal of Materials Science*, 1990. **25**(11): p. 4929-4932.
5. Macquart, P., F. Bridou, and B. Pardo, *Carbon tungsten multilayers for x-ray UV optics deposited by laser evaporation- preparation and interface characterization*. *Thin Solid Films*, 1991. **203**(1): p. 77-86.
6. Wu, X.D., et al., *Low-temperature preparation of high Tc superconducting thin films*. *Applied Physics Letters*, 1988. **52**(9): p. 754-756.
7. Kingston, J.J., et al., *Multilayer YBa<sub>2</sub>Cu<sub>3</sub>O<sub>x</sub>-SrTiO<sub>3</sub>-YBa<sub>2</sub>Cu<sub>3</sub>O<sub>x</sub> films for insulating crossovers*. *Applied Physics Letters*, 1990. **56**(2): p. 189-191.

8. Singh, R.K., O.W. Holland, and J. Narayan, *Theoretical model for deposition of superconducting thin films using pulsed laser evaporation technique*. Journal of Applied Physics, 1990. **68**(1): p. 233-247.
9. Willmott, P.R. and J.R. Huber, *Pulsed laser vaporization and deposition*. Reviews of Modern Physics, 2000. **72**(1): p. 315-328.
10. Narayan, J., *Recent progress in thin film epitaxy across the misfit scale (2011 Acta Gold Medal Paper)*. Acta Materialia, 2013. **61**(8): p. 2703-2724.
11. Greer, J.A. and M.D. Tabat, *Large area pulsed laser deposition: Techniques and applications*. Journal of Vacuum Science & Technology A: Vacuum, Surfaces, and Films, 1995. **13**(3): p. 1175-1181.
12. Cullity, B.D., ed. *Elements of X-Ray Diffraction*. 1982, Addison-Wesley Publishing Co. Inc.
13. Drung, D., et al., *Highly sensitive and easy-to-use SQUID sensors*. IEEE Transactions on Applied Superconductivity, 2007. **17**(2): p. 699-704.

## **Chapter 4**

### **Grain size effect on twin density in as-deposited nanocrystalline Cu film**

In this chapter, the formation of twins and grain size dependence of twin density in NC copper films fabricated by pulsed laser deposition is reported. It is found that the percentage of grains containing twins decreases with decreasing grain size in the grain size range of 2-10 nm. Surprisingly, although the twins were formed during the deposition process without mechanical deformation, detailed analysis suggests that they are most likely deformation twins formed under high internal stress existing in the NC Cu films. This phenomenon may also happen in other NC metallic thin films where internal stresses are high.

#### **4.1 Introduction**

Formation of twins in NC metals [1-3] plays a critical role in their physical and mechanical properties, such as electrical resistivity, strength and ductility. For example, recent experiments show that introduction of nano-twins in ultrafine-grained Cu can

produce an unusual combination of ultrahigh strength (1 GPa) and high ductility [4-10]. Chen et. al. [11] introduced nano-scale twins into Cu grains to change the grain-boundary structure and atomic-diffusion behavior along the boundary. The triple points where twin boundaries meet grain boundaries slowed down electromigration by one order of magnitude, which retarded the electromigration-induced atomic transport. Behrens et al. [12] created active sites of methanol synthesis over industrial catalysts by terminating twin boundaries at the Cu surface to produce steps. They showed that undistorted pure Cu or flat Cu (111) surfaces were inactive in methanol synthesis, whereas stepped sites produced by twin boundaries provide lower energy barriers for intermediates to bind on and improve catalytic efficiency.

When grain size is below 100 nm, twinning was frequently observed even in materials such as copper and nickel with medium to high stacking fault energies [3]. Therefore, twinning becomes one of the important deformation mechanisms for NC materials [13, 14]. The grain size effect on twinning in NC fcc Ni was systematically investigated by Wu and Zhu [15], who observed that the twinning propensity first increases then drops with increasing grain size in the range of 10–75 nm. Similar grain size effect on twinning in NC fcc Cu was later observed in other systems [16, 17]. These observations correlate well with the prediction made by an analytical model of Zhu et. al. [18, 19]. Schiøtz and Jacobsen have observed by molecular dynamic ( MD )

simulation for NC metals that the critical grain size for inverse Hall-Petch for Cu was 7.5 nm, which indicates the importance of grains smaller than 10 nm [20].

However, there have been no experimental reports regarding the grain size effect on the formation of twins during the synthesis of NC metal films. In this paper, we have investigated the grain size effect on twin density in NC copper films synthesized by pulsed laser deposition, where grain size ranged from ~2 nm to ~10 nm. The characteristics and number density of twins were studied as a function of grain size, using transmission electron microscopy (TEM) and high-resolution transmission electron microscopy (HRTEM). The internal strain inside the NC Cu thin film was calculated from X-ray  $\theta$  -  $2\theta$  scan diffraction pattern using the Williamson and Hall analysis [21]. Our analysis indicates that the observed twin density dependence on grain size is consistent with deformation twins instead of pure growth twins. The rationale for this phenomenon is discussed in terms of internal strains present in as-deposited films.

## **4.2 Experimental Approach**

Pulsed laser deposition (PLD) of NC Cu thin film was carried out in a multi-target stainless-steel laser deposition chamber using a pulsed KrF excimer laser (wavelength 248 nm, pulse duration 25 ns, repetition rate 10 Hz). The targets were 4N pure Cu sheet

purchased from ESPI Metals Inc. The PLD chamber was evacuated by a turbo-molecular pump to a vacuum of  $1.33 \times 10^{-4}$  Pa. The laser beam was focused onto the targets at a  $45^\circ$  incidence angle and had a square spot size of 2 mm  $\times$  3 mm. The laser was excited from its source under “High Voltage Constant” mode so that the exciting voltage was maintained at 23.8keV, and the energy of laser beam at the front of the chamber was 0.29-0.30 J. As a result, the energy density of the laser beam was estimated to be  $4.8 - 5 \times 10^4$  J m<sup>-2</sup>. The Si substrates were initially cleaned through a multi-step procedure including boiling in acetone at 150° C for 5 min., ultrasonic cleaning in acetone for 5 min, and ultrasonic cleaning in methanol for 5 min. The Si substrates, which were subsequently cleaned with HF to remove the native SiO<sub>2</sub> layer, were held parallel to the target during deposition. The cleaned substrates were fully dried by nitrogen gun, and then loaded into the deposition chamber where the target–substrate distance was 4cm. During deposition, the target was rotated in order to provide a uniform ablation and avoid pitting on the target surface. The thickness of Cu film was controlled by the number of ablation pulses of the laser beam, which is 2000 in this study.

The microstructural characterization of the as-deposited films was performed by Transmission Electron Microscopy (TEM), using a JEOL-2000FX analytical electron microscope and High-Resolution Transmission Electron Microscopy (HRTEM), using a JEOL-2010F analytical electron microscope equipped with a Gatan image filter (GIF) tuning attachment, which has a point-to-point resolution of 0.18 nm. The samples for

TEM observation were prepared using conventional sample preparation techniques including mechanical polishing, dimpling, and Ar ion milling by using Precision Ion Polishing System (PIPS) at beam voltage of 5 kV, incidence angle of 5° during the initial stage and beam voltage of 3 kV, incidence angle of 2° during the final stage. The sample for HRTEM observation was further ion-milled for 15 mins at beam voltage of 3 kV and incidence angle of 1°. X-ray  $\theta - 2\theta$  scan diffraction pattern was used to calculate the lattice micro-strain by Williamson and Hall analysis, assuming that the total broadening of the peaks can be considered as a simple convolution of grain size broadening and strain broadening.

## **4.3 Results and Discussion**

### **4.3.1 Grain size distribution**

Based on TEM cross-section observations, the Cu film has an average thickness of  $9.8 \pm 1$  nm, and the sizes of grains are less than 10 nm. Based on statistical analysis of more than 300 grains using HRTEM micrographs, the grain size range of NC Cu in this film is found to vary from  $2 \pm 0.5$  nm to  $8 \pm 0.5$  nm. Figure 4.1 (a) shows a NC Cu grain that contains a twin. The size of this grain is approximately 5.7 nm. The mirror relationship of the crystal planes at two sides of the twin boundary is clearly marked by the white lines. The angle between the crystal planes at two sides of the twin boundary

is measured to be  $\sim 141^\circ$ , which is consistent with a typical twin in fcc-structured materials. Only one twin boundary with small twin thickness is observed in the grain, possibly because of the small grain size. As a comparison, Figure 4.1 (b) shows an HRTEM image of another twin in a larger Cu grain ( $\sim 40\text{-}50$  nm), which was found in another Cu film grown on Si substrate using TiN as the buffer layer. In the latter film, Cu grains can easily reach the size of 100 nm and the twins are more likely to grow thicker. Multiple twin boundaries can be found instead of only one in a single Cu grain.

The grain size distribution of  $\sim 300$  grains in the NC Cu film is shown in Figure 4.2 (a). The number of grains within each size range first increases with increasing grain size from  $\sim 2$  nm and reaches a maximum value when the grain size is between 4 and 5 nm. Then it decreases with decreasing grain size. The grain size distribution was fitted by B-N model [22] based upon thermodynamic free energy, as shown in Figure 4.2 (b). In this model, the particle size distribution is derived from thermodynamic effects, neglecting all the possible kinetic influence. The particle size distribution is described by the following function:

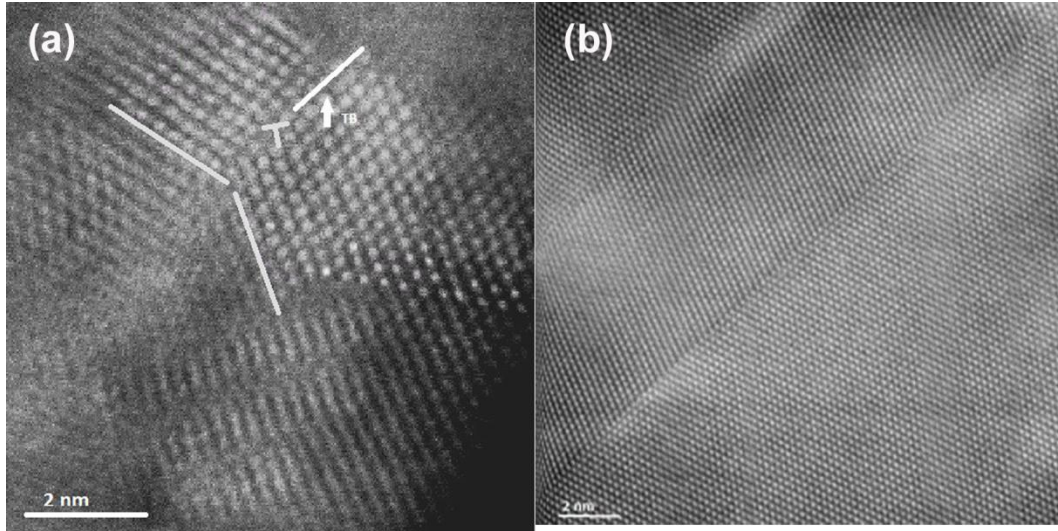


Figure 4.1 (a) HRTEM micrograph of a NC Cu grain in which a twin exists. (b) HRTEM micrograph of a twin in large Cu grains (~40-50 nm).

$$f(d) = A \exp \left[ - \left( \frac{d_c}{d} + 2 \frac{d}{\langle d \rangle} + \frac{d}{d_m} \right) \right]$$

Where  $f(d)$  is the grain size distribution frequency,  $A$  is a constant,  $d$  is the grain size (diameter),  $d_c$  is the critical size corresponding to the mean Gibbs free energy  $E$  of grains,  $\langle d \rangle$  is the average particle size and  $d_m$  is the upper limit of grain size. It is worth noting that the above equation is suitable for distribution of both particles and grains [22]. Both  $\langle d \rangle$  and  $d_m$  can be experimentally determined. The value of the critical size is obtained from the maximum value of the particle size distribution function, which is located at  $d = d^*$ , by the following equation:

$$d_c/d^{*2} = 2 / \langle d \rangle + 1 / d_m$$

In which  $d^*$  is the grain size where  $f(d)$  reaches the maximum value. In this fitting,  $A=25.891$ ,  $d_m = 9$  nm,  $\langle d \rangle = 4.86$  nm,  $d^* = 4.5$  nm so that  $d_c$  is calculated to be 10.7 nm from the above equation.

As demonstrated in Figure 4.2 (b), although the general trend of the grain size distribution is described, there is a discrepancy between the experimental results and the B-N model. This discrepancy results from the fact that PLD is a non-equilibrium deposition technique, which indicates that kinetic effects need to be considered for the thin-film situation. Since the film is only one to two grains thick, the large misfit strain energy between the film and the substrate has to be accommodated within such a short distance, mostly by grain boundaries, which are abundant in this film as NC Cu grains are smaller than 10 nm. The strain energy at grain boundaries would consequently influence the orientation and sizes of grains. Furthermore, this strain energy would activate the slip of partial dislocations from grain boundaries and grain boundary junctions, which will be addressed in the following section.

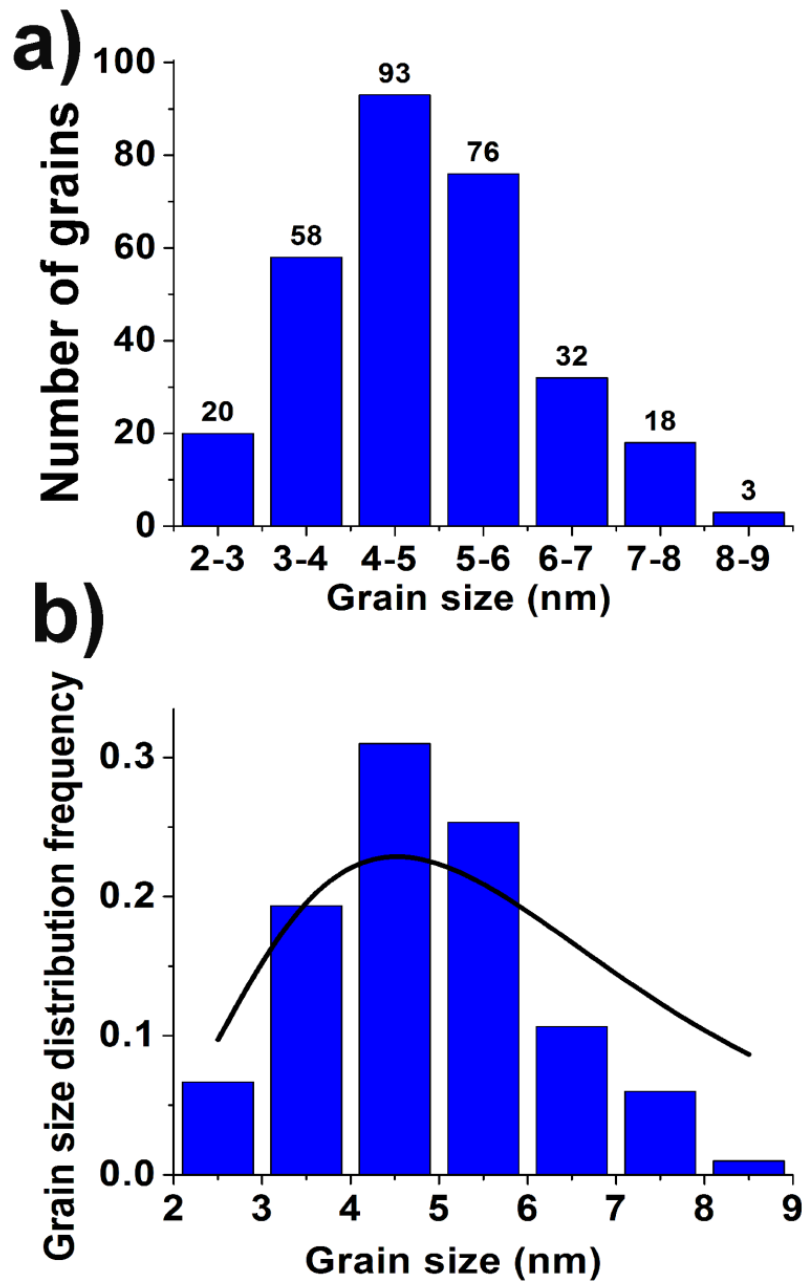


Figure 4.2 (a) Grain size distribution of the NC Cu film on Si. (b) B-N model fitting of the grain size distribution of NC Cu film on Si.

### 4.3.2 Grain size effect on twin density in NC Cu grains

Figure 4.3 (a) shows the dependence on grain size of NC Cu grains containing twins. The number of grains containing twins first increases with increasing grain size from  $\sim 2$  nm and reaches a maximum value when grain size is between 4 and 5 nm. Then it decreases with decreasing grain size. Compared with Figure 4.2 (a), it is apparent that the distribution of the number of grains containing twins is closely related to the total grain size distribution. For a simple growth process like PLD, one would intuitively draw the conclusion that the observed twins are all growth twins. If twins in these NC copper films are comprised of only growth twins in nature, the number of twins in NC Cu grains should be proportional to the surface area of the grains in which they exist. This is because the growth twins are likely to be formed by movements of Shockley Partials on adjacent slip planes, and when grain size is small, grain boundaries become the primary source for the generation of Shockley Partials [23, 24]. Given the ratio between the number of twins ( $n$ ) and grain surface area ( $A$ ) to be the area density of twins ( $\rho_A$ ),  $\rho_A$  should be a constant for grains with different sizes. Assume that the grains are spherical and thus the surface area of grains in each size range is proportional to  $d^2$ , in which  $d$  is the average diameter of the grains, the dependence of  $\rho_A$  on  $d^2$  for each grain size range is displayed in Figure 4.3 (b). ( $\rho_A = 4n/\pi d^2$ ). It is clear that the area density of twins ( $\rho_A$ ) varies dramatically with grain size, suggesting that growth twins are not predominant in these NC Cu grains.

To have a clearer understanding of the grain size effect on twin density, the percentage of grains containing twins is calculated for each size range, which is shown in Figure 4.3 (c). The percentage of grains containing twins decreases monotonically with decreasing grain size in the observed grain size range of 3 nm to 8 nm. The fact that no twins were found in the size range of 8 nm to 9 nm is due to statistical problem. In other words, the total number of grains in this size range is too small. This observation is consistent with the reported inverse grain size effect on deformation twins [15, 16].

In an analytical model by Zhu et al [3, 19], it is predicted that the optimum grain size for deformation twinning in NC Cu is 38-54 nm, below which twinning becomes more difficult with decreasing grain size, i.e. the inverse grain size effect. The model by Zhu et al is based on the assumption that twins are formed by the emission of partial dislocations from grain boundaries [3, 18, 19] and these twins are of deformation twins in nature. The optimum grain size range can be calculated from the equation [19]:

$$[(2.09-\nu) Ga^2] / [54.99 (1-\nu) \gamma] \leq d_{op} / \ln (2^{0.5} d_{op} / a) \leq [(3.73+\nu) Ga^2] / [97.0 (1-\nu) \gamma]$$

Where  $G$  is the shear modulus,  $\nu$  is the Poisson's ratio,  $a$  is the lattice constant,  $d_{op}$  is the optimum grain size for twinning, and  $\gamma$  is the stacking fault energy.

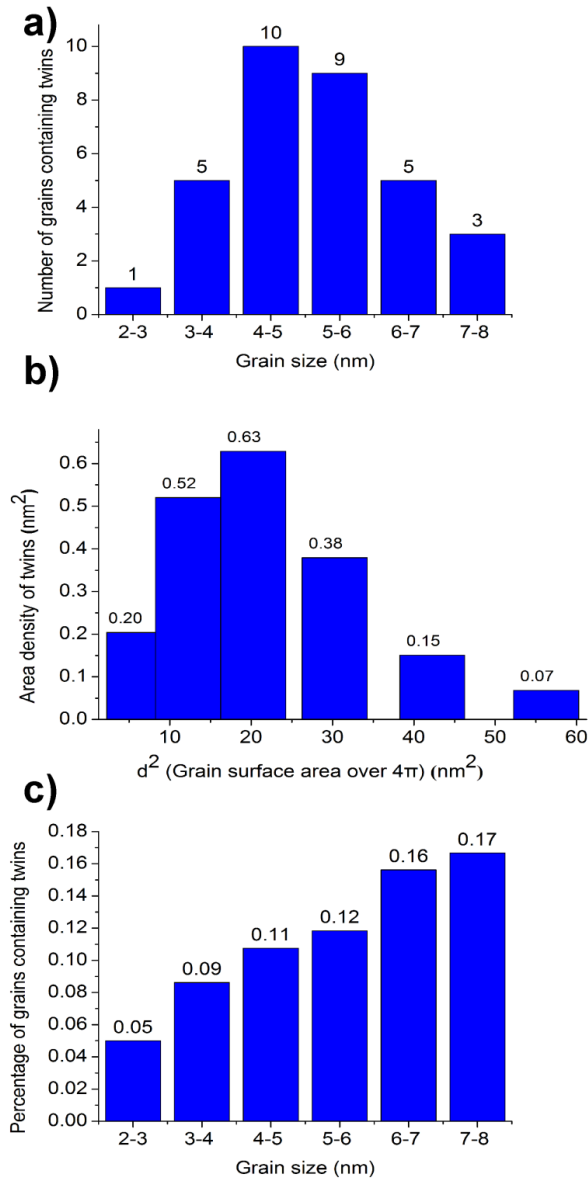


Figure 4.3 (a) The distribution of number of grains that contain twins as a function of grain size. (b) Dependence of surface area density of twins on  $d^2$  (grain surface area over  $4\pi$ ) for different grain size ranges. (c) Percentage of grains containing twins for different grain sizes.

The optimum grain size range in the above equation takes all types of dislocations into consideration, i.e. screw dislocations, 60° dislocations and their mixtures in an fcc metal [19]. The average optimum grain size can be calculated by [3]:

$$d_m / \ln (2^{0.5} d_m / a) = [(9.69-\nu) Ga^2] / [254(1-\nu) \gamma]$$

For Cu, taking the Poisson's ratio to be 0.36, lattice constant 3.61 Å, stacking fault energy 45 mJ/m<sup>2</sup> and shear modulus 54.6 Gpa, the average optimum grain size is calculated to be 47 nm. Consequently when grain size of NC Cu is below 47 nm, the twinning propensity will decrease with decreasing grain size, which is consistent with the observation shown in Figure 4.3 (c). The size range in the present experiment represents the initial portion of the grain size effect depicted by the model. It is interesting that the twins formed during a deposition process in this study have a similar grain size effect with deformation twins in NC metals. This suggests that most of twins observed in the NC Cu grains are likely deformation twins. It is worth noting that growth twins should also exist in the NC Cu film, because growth twins have been extensively reported in NC Cu [4, 25].

The above observation and analysis raise a critical question: how could deformation twins form in the NC Cu synthesized by the physical deposition process? For a deformation twin to form, partial dislocations usually need to be emitted from the grain boundaries under an applied stress. To clarify this issue, we performed analysis

of X-ray peak broadening to measure the internal residual elastic strain and stress in the as-deposited Cu-film samples, using the Williamson and Hall analysis, which assumes that the combined effect of size broadening  $\beta_L$  and strain broadening  $\beta_e$  could be determined by convolution (a simple summation of them).  $\beta_L$  and  $\beta_e$  vary quite differently with respect to Bragg angle as follows,

$$\beta_L = k \lambda / (d \cos \theta)$$

$$\beta_e = \varepsilon \tan \theta$$

Therefore the total broadening  $\beta_{\text{total}}$  can be represented by the equation:

$$\beta_{\text{total}} \cos \theta = (\beta_L + \beta_e) \cos \theta = k \lambda / d + \varepsilon \sin \theta$$

where  $\beta$  is the measured integral width,  $\theta$  is the peak maximum position,  $k$  is a constant,  $\lambda$  is the wavelength, and  $\varepsilon$  is the micro-strain. By plotting  $\beta_{\text{total}} \cos \theta$  versus  $\sin \theta$  we obtain the strain component from the slope, which is  $\sim 3.6\%$  for the film. The result shows that significant amount of strain remains in the as-deposited film. Three peaks (Cu(111), (200) and (400)) were adopted for the linear fitting, which is reasonable. However, errors may exist since the peak broadening contributions from dislocation density and sample anisotropy are neglected. Indeed Williamson and Hall plot has shown good linear fitting for nanocrystalline Cu as well [26]. Based on the stress – strain relationship in thin films [27]:

$$\tau = 2 G \varepsilon (1 - \nu) / (1 + \nu)$$

in which  $\tau$  is the stress,  $G$  is the shear modulus,  $\nu$  is the Poisson's ratio and  $\varepsilon$  is the strain, the internal stress inside the Cu film is calculated to be  $\sim 1.8$  GPa. Similar high stress is also found in as-deposited NC Ni-W films by Tiffany et. al. [28, 29]. In fact, they reported that the residual stress in as-deposited NC Ni-W films can reach values as high as 2.3 GPa [29]. At low temperature, the critical stress for partial dislocation emission in Cu (grain size=10 nm) is predicted to be 0.42 GPa [30], and the critical stress for deformation twinning formation is predicted to be 0.37 GPa [3]. Consequently the high stress in our NC Cu film is the main cause for driving partial dislocations from grain boundaries to form deformation twins. It should be noted that the critical stress for twinning increases with decreasing grain size, which makes smaller grains more difficult to deform by twinning, leading to the observed inverse grain size effect below the optimal grain size for twinning [15]. The twins are formed most likely by the successive emissions of partials from grain boundaries, as reported in recent papers [1, 31].

Since the high internal strain of the film is accommodated mostly by grain boundaries, high densities of extrinsic dislocations will exist along the grain boundaries to relax the strain energy. Grain boundaries in NC materials are considered to be at non-equilibrium state if high densities of extrinsic (extra) dislocations exist [32, 33]. These dislocations are referred to as extrinsic because they are not geometrically necessary.

On the contrary, intrinsic dislocations are those necessary to accommodate the geometrical misorientations between adjacent grains [34]. We indeed observed extrinsic dislocations in our PLD Cu films.

#### **4.4 Conclusions**

In summary, twins formed in PLD-deposited NC Cu films, where grain size ranged from 2 nm to 10 nm. Deformation twins are considered dominant in the films because of the following three reasons: 1) the similar grain size effect with that of deformation twins; 2) the deviation of the grain surface area density of twins ( $\rho_A$ ) from a constant; 3) the high internal stress existing in the NC Cu films. This is contrary to our intuition that growth twin should be dominant in these NC Cu films because the twins were formed by crystalline growth during a physical deposition process. Our observation here indicates that deformation twins could be formed easily since the internal stress in the film is high. This phenomenon could also exist in other nanocrystalline films produced by deposition methods.

## References

- [1] Y.T. Zhu, J. Narayan, J.P. Hirth, S. Mahajan, X.L. Wu, X.Z. Liao, *Formation of single and multiple deformation twins in nanocrystalline fcc metals*. *Acta Mater.* 2009;57(13):3763-3770.
- [2] J. Narayan, Y.T. Zhu, *Self-thickening, cross-slip deformation twinning model*. *Appl. Phys. Lett.* 2008;92(15):151908.
- [3] Y.T. Zhu, X.Z. Liao, X.L. Wu, *Deformation twinning in nanocrystalline materials*. *Progress in Materials Science* 2012;57(1):1-62.
- [4] L. Lu, Y.F. Shen, X.H. Chen, L.H. Qian, K. Lu, *Ultrahigh strength and high electrical conductivity in copper*. *Science* 2004;304(5669):422-426.
- [5] K. Lu, L. Lu, S. Suresh, *Strengthening Materials by Engineering Coherent Internal Boundaries at the Nanoscale*. *Science* 2009;324(5925):349-352.
- [6] E. Ma, Y.M. Wang, Q.H. Lu, M.L. Sui, L. Lu, K. Lu, *Strain hardening and large tensile elongation in ultrahigh-strength nano-twinned copper*. *Appl. Phys. Lett.* 2004;85(21):4932-4934.
- [7] Y.H. Zhao, J.E. Bingert, X.Z. Liao, B.Z. Cui, K. Han, A.V. Sergueeva, A.K. Mukherjee, R.Z. Valiev, T.G. Langdon, Y.T. Zhu, *Simultaneously increasing the ductility and strength of ultra-fine-grained pure copper*. *Adv. Mater.* 2006;18(22):2949.

- [8] Z.W. Wang, Y.B. Wang, X.Z. Liao, Y.H. Zhao, E.J. Lavernia, Y.T. Zhu, Z. Horita, T.G. Langdon, *Influence of stacking fault energy on deformation mechanism and dislocation storage capacity in ultrafine-grained materials*. Scripta Mater. 2009;60(1):52-55.
- [9] Y.H. Zhao, X.Z. Liao, Z. Horita, T.G. Langdon, Y.T. Zhu, *Determining the optimal stacking fault energy for achieving high ductility in ultrafine-grained Cu-Zn alloys*. Mater. Sci. Eng. A 2008;493:123-129.
- [10] X.L. Wu, X.Z. Liao, S.G. Srinivasan, F. Zhou, E.J. Lavernia, R.Z. Valiev, Y.T. Zhu, *New deformation twinning mechanism generates zero macroscopic strain in nanocrystalline metals*. Phys. Rev. Lett. 2008;100(9):095701-.
- [11] K.C. Chen, W.W. Wu, C.N. Liao, L.J. Chen, K.N. Tu, *Observation of atomic diffusion at twin-modified grain boundaries in copper*. Science 2008;321(5892):1066-1069.
- [12] M. Behrens, F. Studt, I. Kasatkin, S. Kuhl, M. Havecker, F. Abild-Pedersen, S. Zander, F. Girgsdies, P. Kurr, B.L. Kniep, M. Tovar, R.W. Fischer, J.K. Norskov, R. Schlogl, *The active site of methanol synthesis over Cu/ZnO/Al<sub>2</sub>O<sub>3</sub> industrial catalysts*. Science 2012;336(6083):893-897.
- [13] X.Z. Liao, A.R. Kilmametov, R.Z. Valiev, H.S. Gao, X.D. Li, A.K. Mukherjee, J.F. Bingert, Y.T. Zhu, *High-pressure torsion-induced grain growth in electrodeposited nanocrystalline Ni*. Appl. Phys. Lett. 2006;88(2):021909.
- [14] X.Z. Liao, Y.H. Zhao, S.G. Srinivasan, Y.T. Zhu, R.Z. Valiev, D.V. Gunderov, *Deformation twinning in nanocrystalline copper at room temperature and low strain rate*. Appl. Phys. Lett. 2004;84(4):592-594.

- [15] X.L. Wu, Y.T. Zhu, *Inverse grain-size effect on twinning in nanocrystalline Ni*. Phys. Rev. Lett. 2008;101(2):025503.
- [16] J.Y. Zhang, G. Liu, R.H. Wang, J. Li, J. Sun, E. Ma, *Double-inverse grain size dependence of deformation twinning in nanocrystalline Cu*. Phys. Rev. B 2010;81(17):172104.
- [17] S. Ni, Y.B. Wang, X.Z. Liao, H.Q. Li, R.B. Figueiredo, S.P. Ringer, T.G. Langdon, Y.T. Zhu, *Effect of grain size on the competition between twinning and detwinning in nanocrystalline metals*. Phys. Rev. B 2011;84(23):235401.
- [18] Y.T. Zhu, X.Z. Liao, S.G. Srinivasan, Y.H. Zhao, M.I. Baskes, F. Zhou, E.J. Lavernia, *Nucleation and growth of deformation twins in nanocrystalline aluminum*. Appl. Phys. Lett. 2004;85(21):5049-5051.
- [19] Y.T. Zhu, X.Z. Liao, S.G. Srinivasan, E.J. Lavernia, *Nucleation of deformation twins in nanocrystalline face-centered-cubic metals processed by severe plastic deformation*. J. Appl. Phys. 2005;98(3):034319.
- [20] J. Schiotz, K.W. Jacobsen, *A maximum in the strength of nanocrystalline copper*. Science 2003;301(5638):1357-1359.
- [21] G.K. Williamson, W.H. Hall, *X-Ray Line Broadening from Fined Aluminium and Wolfram*. Acta Metallurgica 1953;1(1):22-31.
- [22] R.R. Bitti, P.E. Di Nunzio, *On the shape of the particle size distribution in coarsening processes*. Scripta Mater. 1998;39(3):335-340.
- [23] Y.T. Zhu, X. Liao, *Nanostructured metals: Retaining ductility*. Nature materials 2004;3(6):351-352.

- [24] Z. Budrovic, H. Van Swygenhoven, P.M. Derlet, S. Van Petegem, B. Schmitt, *Plastic deformation with reversible peak broadening in nanocrystalline nickel*. Science 2004;304(5668):273-276.
- [25] X.H. Chen, L. Lu, K. Lu, *Electrical resistivity of ultrafine-grained copper with nanoscale growth twins*. J. Appl. Phys. 2007;102(8):083708.
- [26] S. Sheibani, A. Ataie, S. Heshmati-Manesh, G.R. Khayati, *Structural evolution in nanocrystalline Cu synthesized by high energy ball milling*. Materials Letters 2007;61(14-15):3204-3207.
- [27] J. Narayan, *Recent progress in thin film epitaxy across the misfit scale (2011 Acta Gold Medal Paper)*. Acta Materialia 2013;61(8):2703-2724.
- [28] U. Welzel, J. Kümmel, E. Bischoff, S. Kurz, E.J. Mittemeijer, *Nanoscale planar faulting in nanocrystalline Ni-W thin films: Grain growth, segregation, and residual stress*. Journal of Materials Research 2011;26(19):2558-2573.
- [29] T.D. Ziebell, C.A. Schuh, *Residual stress in electrodeposited nanocrystalline nickel-tungsten coatings*. Journal of Materials Research 2012;27(09):1271-1284.
- [30] R.J. Asaro, P. Krysl, B. Kad, *Deformation mechanism transitions in nanoscale fcc metals*. Philosophical Magazine Letters 2003;83(12):733-743.
- [31] Y.T. Zhu, X.L. Wu, X.Z. Liao, J. Narayan, S.N. Mathaudhu, L.J. Kecskes, *Twinning partial multiplication at grain boundary in nanocrystalline fcc metals*. Appl. Phys. Lett. 2009;95(3):031909.

[32] X.L. Wu, Y.T. Zhu, *Partial-dislocation-mediated processes in nanocrystalline Ni with nonequilibrium grain boundaries*. Appl. Phys. Lett. 2006;89(3):031922.

[33] J.Y. Huang, Y.T. Zhu, H. Jiang, T.C. Lowe, *Microstructures and dislocation configurations in nanostructured Cu processed by repetitive corrugation and straightening*. Acta Mater. 2001;49(9):1497-1505.

[34] R.Z. Valiev, V.Y. Gertsman, O.A. Kaibyshev, *Grain-Boundary Structure and Properties under External Influences*. Phys. Stat. Sol. a 1986;97(1):11-56.

## **Chapter 5**

### **Twin intersection mechanisms in nanocrystalline fcc metals**

Deformation twins have been reported to produce high strength and ductility. Intersections of deformation twins may affect the microstructural evolution during plastic deformation and consequently influence mechanical properties. However, the mechanisms governing twin-intersection behavior remain poorly understood. In this chapter, we investigated twin intersection mechanisms by observing twin transmission across the boundary of another twin using high-resolution transmission electron microscopy. Based on the experimental observations, mechanisms were proposed for twin-twin intersections and associated dislocation reactions in nanocrystalline fcc materials.

#### **5.1 Introduction**

When one twin meets another twin, what mechanism governs their intersection? This problem is interesting because deformation twinning in nanocrystalline (NC) materials is of both fundamental and technological significance. Experimental observations [1-4] and molecular dynamics (MD) simulations [5, 6] reveal that

deformation twins will interact with gliding dislocations, which simultaneously increases the strength and ductility of NC materials [2, 7]. In NC face-centered cubic (fcc) metals, deformation twinning has been observed under various deformation conditions, including low temperature [8], high strain rate [9], high-pressure torsion [10-12], uniaxial tensile testing [13] and cryogenic ball milling [14]. Moreover, it has been reported that for NC fcc metals, twinning becomes a major deformation mechanism within a range of grain sizes [15-19].

When multiple twinning systems are activated in fcc metals, interactions between various twinning systems become inevitable. This not only affects the microstructural evolution but also is expected to affect the mechanical behavior of the material during deformation. Twin intersections have been observed in fcc stainless steel [20] and Hadfield steel single crystals [21]. These experimental observations raise a critical question: what is the dislocation mechanism associated with the observed twin intersections?

To answer the above question, we studied intersections of twins in NC Cu film and Cu-30 wt% Zn-0.8 wt% Al alloy (Brass 260, Cartridge Brass) samples using high-resolution transmission electron microscopy (HRTEM). These two material systems were selected because NC Cu has been reported to easily form deformation twins [22-24], and the Brass 260 alloy has lower stacking fault energy than Cu and also easily forms deformation twins and twin intersections [25]. To study the intersection

mechanism of twins, we have obtained clear HREM images at locations where one twin transmits across the coherent boundary of another twin. This requires a low dislocation density around the observed region to reduce lattice distortions. Detailed sample preparation procedures to meet this requirement are described in the next section.

## 5.2 Experimental Approach

Both an NC Cu film and NC Brass 260 alloy samples were used in this study. The NC Cu film was deposited on a coarse-grained Cu substrate using pulsed laser deposition (PLD). The coarse-grained Cu substrate was used so that it deformed evenly with the NC Cu film under uniaxial tension to a designated strain. The PLD processing parameters can be found in a previous paper [26]. The NC Cu film was strained under tension together with the substrate at a strain rate of  $2.5 \times 10^{-4} \text{ s}^{-1}$  to a plastic strain of 1.5%. Such a small tensile strain was chosen to reduce the density of accumulated dislocations at twin boundaries so that clear HREM images can be obtained from the area of twin intersections.

The NC Brass 260 alloy was processed by cryo-milling and spark plasma sintering (SPS). The SPS serves two purposes: to consolidate the alloy powder for easier HRTEM sample preparation and to reduce dislocation density for higher quality HRTEM images. Dislocations formed during cryo-milling are mostly annihilated during the high-

temperature SPS process so that the deformation twin boundaries become more coherent and straight [25]. The detailed processing parameters can be found in a previous publication [25].

Special care was taken during the sample preparation so that no extra dislocations were introduced into the final TEM sample. TEM specimens were prepared by mechanical grinding and dimpling, followed by ion milling. Low-energy ion beam was used for ion milling to minimize the irradiation damage by the ion beam and to remove the deformed surface layer on the TEM sample. HRTEM investigations were performed on JEOL analytical electron microscopes operating at 200 kV, with point to point resolution of 0.18 nm. Details on HRTEM sample preparation can be found in our previous publications [25, 26].

## **5.3 Results and Discussion**

### **5.3.1 TEM and HRTEM observation of twin transmission across twin boundary**

Figure 5.1 (a) is a typical HRTEM image showing a twin transmitting across the boundary of another twin in the NC Cu film that was fabricated by PLD and subsequently deformed to plastic strain of 1.5 % by uniaxial tension. Figure 5.1 (b) is an HRTEM image enlarged from the twin transmission area in Figure 5.1 (a) and is marked for the convenience of description.

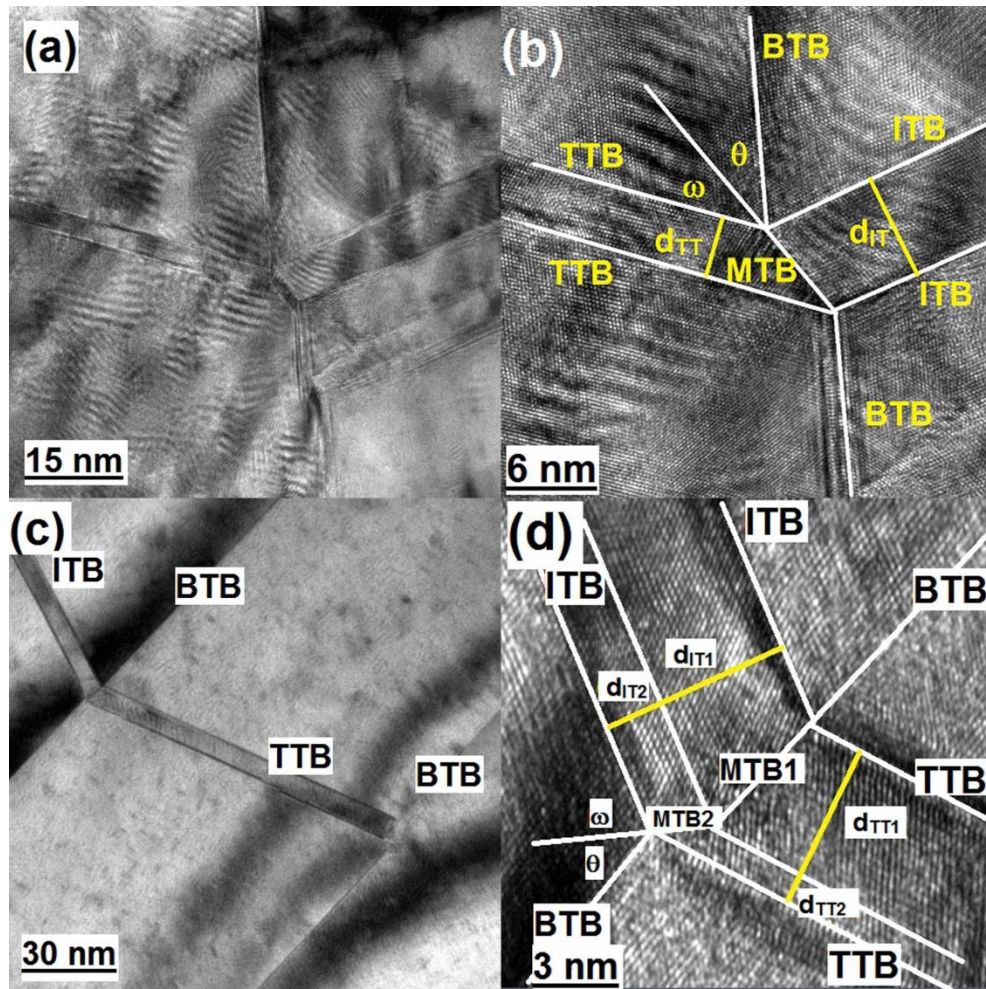


Figure 5.1 (a) A typical HRTEM image showing twin transmission phenomenon in NC Cu films processed by PLD and the subsequent uniaxial elongation; (b) The HRTEM image showing the transmission area shown in (a) with marks added; (c) A typical TEM image showing twin transmission phenomenon in NC Brass 260 alloy processed by cryo-milling and the following SPS; (d) The HRTEM image showing the twin transmission area in (c) with marks added.

The ITB and TTB stand for the incident twin boundary and transmittal twin boundary, respectively. BTB and MTB represent the barrier twin boundary and the migrated twin boundary of the barrier twin, respectively.  $\omega$  is the angle between the TTB and MTB, and  $\theta$  is the angle between the BTB and MTB. The  $d_{IT}$  and  $d_{TT}$  are the twin thicknesses of incident twin (IT) and transmittal twin (TT), respectively. Suppose the upper section of BTB is the original BTB before twin transmission and IT is the twin to whose side that BTB migrates. As shown in Figure 5.1 (b), the IT penetrates the BTB from the right side of BTB and after reactions with the BTB, it transforms into a TT on the left-hand side of the BTB.

The twinning planes for IT and TT are different  $\{111\}$  planes so that the ITB forms an angle of  $\sim 141^\circ$  with the TTB. The BTB, ITB and TTB are coherent twin boundaries on  $\{111\}$  slip planes, while MTB deviate from the original BTB. As shown in Figure 5.1 (b), the reaction between IT and BTB caused the migration of the BTB towards the IT side to form MTB when IT transmitted across the BTB. The MTB in Figure 5.1 (b) is a straight line lying between the IT and TT, and is also the bisector of the angle between BTB and TTB, which in this case means  $\omega = \theta = 35.25^\circ$ .  $d_{IT}$  and  $d_{TT}$  were measured from the HRTEM micrograph as  $6.3 \pm 0.5$  nm and  $3.6 \pm 0.5$  nm, respectively, which leads to a ratio of  $d_{IT}/d_{TT} \cong 1.7$ .

Figure 5.1 (c) is a typical TEM image showing twin transmission in Brass 260 alloy processed by cryo-milling and spark plasma sintering. An incident twin (IT) first

penetrates the BTB from the top left corner of the image and after reacting with the BTB, transforms into a TT along another  $\{111\}$  plane. The TT then meets and reacts with another BTB, but does not transmit across the second BTB. Figure 5.1 (d) is an HRTEM image enlarged from the MTB area in Figure 5.1 (c). Unlike the situation shown in Figure 5.1 (b), the MTB here can be divided into two sections. In the upper section (marked as MTB1), no migration of BTB occurred and therefore MTB1 coincide with the BTB. Both  $d_{TT1}$  and  $d_{IT1}$  were measured from the HRTEM micrograph to be  $3.8 \pm 0.3$  nm, which indicates that the thickness of the IT is maintained as it transmitted across the BTB to form TT. In the second section, the MTB2 deviates from the BTB by an angle of  $\theta \approx 43^\circ$ . We measured  $d_{IT2}$  and  $d_{TT2}$  from the Figure 5.1 (d) as  $1.7 \pm 0.2$  nm and  $0.8 \pm 0.1$  nm, respectively, which leads to a ratio of  $d_{IT2}/d_{TT2} \cong 2$ .

### 5.3.2 Possible dislocation reactions at the intersection of two twin boundaries

To better understand the twin transmission mechanism, we need to refer to the double Thompson tetrahedron [27, 28], which is shown in Figure 5.2. The ITB, BTB and TTB planes correspond to BCD, ABC and BCD' planes in Figure 5.2, respectively.  $\alpha$ ,  $\beta$ ,  $\gamma$  and  $\delta$  stand for centroids of triangles in the Thompson tetrahedron. For the formation of ITB, Shockley partials need to be emitted from grain boundaries and glide on BCD planes toward the ABC plane under an applied stress.

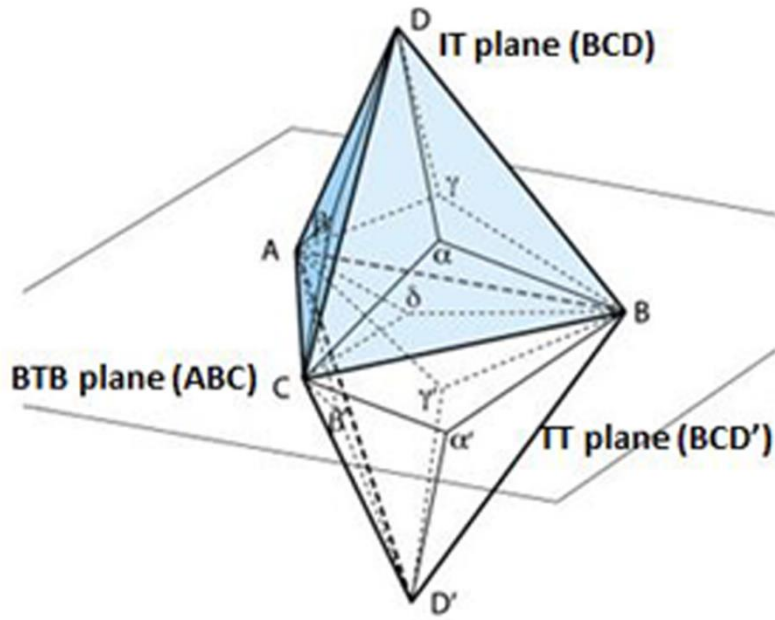
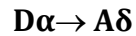


Figure 5.2 Schematic illustration of a double Thompson tetrahedron.

When a Shockley partial reaches the ABC plane, its dislocation line runs parallel to the intersection line of plane BCD and ABC, which is line BC ( $\langle 110 \rangle$  direction). The Shockley partial can be of the following two types: (1) a  $30^\circ$  Shockley partial dislocation (either  $\mathbf{C}\alpha$  or  $\mathbf{B}\alpha$  on BCD plane), or (2) a  $90^\circ$  Shockley partial dislocation ( $\mathbf{D}\alpha$  on BCD plane). The Shockley partials can either cross-slip onto the ABC plane or transmit onto the BCD' plane and then glide away from plane ABC to form a TT. Since the twin transmission occurs due to dislocation reactions at the intersection of two twin boundaries, the reactions of twin partial dislocations are actually interactions between

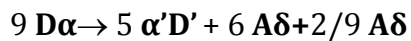
dislocations and the twin boundary, which have been analyzed in our previous paper [28]. As described in the paper [28], four types of dislocation reactions are possible to occur:



The first two equations describe the transmission and cross-slip mechanisms of a 30° Shockley partial dislocation gliding on the BCD plane. Both of them generate a sessile stair-rod dislocation, which will stay on the ABC plane. The last two equations describe the transmission and cross-slip mechanisms of a 90° Shockley partial dislocation gliding on the BCD plane. When a Shockley partial dislocation on the BCD plane cross-slips onto the ABC plane, its sequential movement will move BTB by one atomic plane. The energy barriers for these dislocation-twin reactions have been discussed in the previous publication [28].

### 5.3.3 Explanation of the experimentally observed twin transmissions

The experimentally observed twin transmission phenomena can be understood with the help of HRTEM images and the above analysis. From Figure 5.1 (b), we found that the IT is 30 atomic planes thick, while the TT is only 17 atomic planes thick. This means that a total of 30 partials glided on different BCD planes to form the IT, but only 17 of them transmitted across the BTB. Suppose M and N are the numbers of planes inside IT and TT, respectively, the ratio of M to N is  $\cong 1.76$ . It is worth noting that planes in IT and TT are all  $\{111\}$  planes so that the ratio between  $d_{IT}$  and  $d_{TT}$  are equal to the ratio of M to N. The MTB in Figure 5.1 (b) bisects the angle between BTB and TTB, so that  $\theta = 35.25^\circ$ . This configuration is schematically illustrated in Figure 5.3 (a), in which  $M=9$  and  $N=5$  lead to a ratio of 1.8 between M and N, which is close to the experimentally obtained ratio. Various combinations of dislocation reactions may lead to this configuration. However, a combination of five dislocation reactions according to the third equation and four reactions according to the fourth equation produces an MTB with the lowest energy, i.e. the lowest residual dislocation content on the MTB:



This equation generates six  $90^\circ$  Shockley partial dislocations on plane ABC so that the gliding of them will move BTB by six atomic planes, which is consistent with the schematic illustration in Figure 5.3 (a). The residual dislocation on MTB is only  $2/9 A\delta$

for every 9 partials on adjacent BCD planes, which makes this MTB energetically very stable.

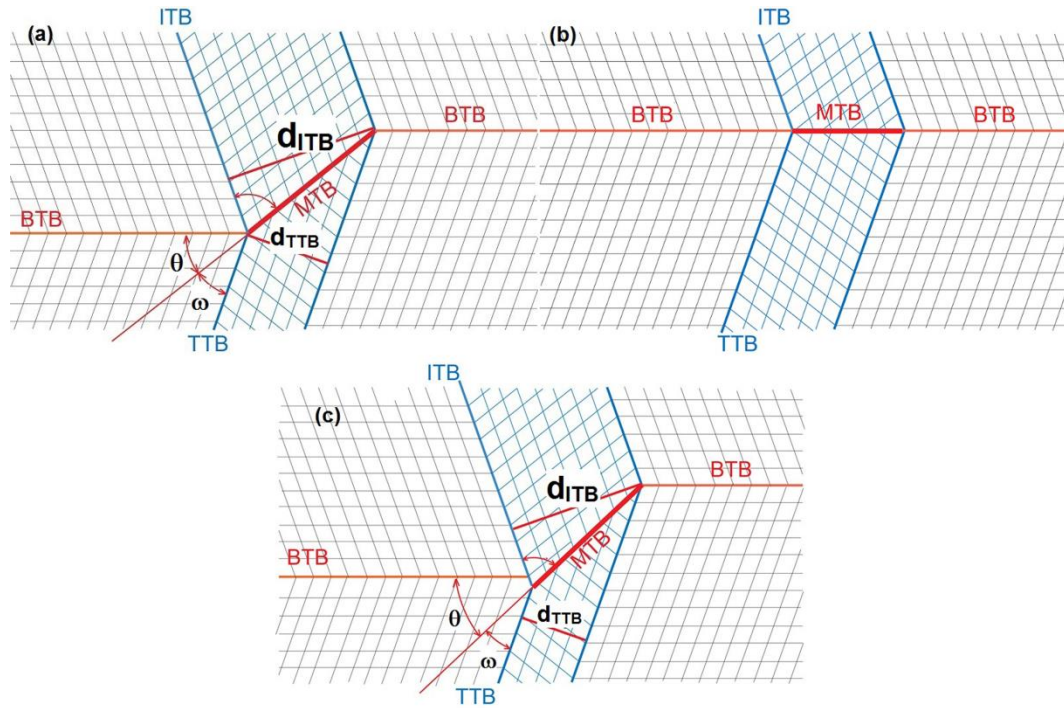


Figure 5.3 Schematic illustrations of twin transmission phenomena with (a)  $\theta = 35.25^\circ$ , (b)  $\theta = 0^\circ$ , and (c)  $\theta = 43^\circ$ .

The twin transmission phenomenon in Brass 260 alloy processed by cryo-milling and SPS can also be explained with similar analysis of the HRTEM image shown in Figure 5.1 (d). As discussed earlier, the MTB here has two sections. The MTB1 coincides

with the original BTB, for which both the IT and TT have the same thickness of 18 atomic planes. This indicates that a total of 18 partials gliding on BCD planes reached plane ABC, and all of them transmitted across the BTB, which led to an M to N ratio of 1. This scenario is schematically illustrated in Figure 5.3 (b), in which M=N=6. As shown in Figure 5.3 (b), the ITB, TTB and BTB are all coherent twin boundaries, but the MTB is a semi-coherent twin boundary in nature. Since no steps were generated on BTB, the possible dislocation reaction is described by the third equation, and this reaction happens on every slip plane for the twin to transmit across the BTB. This also led to a  $4/9 A\delta$  residual dislocation on every plane at the MTB1. Therefore, this MTB is a high-energy boundary.

In the second section, the BTB migrates towards the IT side to form MTB2 in Figure 5.1 (d) with an angle of  $\theta \sim 43^\circ$  with the original BTB. From the previous discussion, the ratio of  $M/N = d_{IT2}/d_{TT2} = 2/1$ . This is schematically illustrated in Figure 5.3 (c), in which M=8, N=4. However, MTB is incoherent in this case, which is caused by the high residual dislocation content, as described below. This twin transmission phenomenon can be produced by a combination of equal number of dislocation reactions described by the second and third equations:

$$4 \mathbf{B}\alpha + \mathbf{D}\alpha = 4 \mathbf{B}\delta + 4\delta\alpha + 4 \alpha'\mathbf{D}' + \mathbf{A}\delta + 7/9 \mathbf{A}\delta$$

For every eight twinning partials gliding on the BCD planes, four of them are transmitted to the BCD' planes and 5 partials are generated on plane ABC so that BTB migrates towards the IT side by 5 atomic planes, which is consistent with the illustration in Figure 5.3 (c). The residual dislocations on MTB are  $7/9 \mathbf{A}\delta$  and  $4 \mathbf{\delta}\alpha$ . Therefore, compared with the MTB in Figure 5.3 (a), this MTB has a higher energy.

The proposed dislocation-reaction mechanisms have residual dislocation components on the MTB, which causes lattice distortion (elastic strain) near MTB and consequently reduces the coherency of MTB, as illustrated schematically in Figure 5.3. The lattice distortion in the MTB region is clearly visible in the HRTEM images, as shown in Figure 5.4, which are enlarged from the MTB areas in Figure 5.1. The contrast difference around the MTB regions also shows evidence of elastic strain. Figure 5.4 (a) shows the region of the  $35^\circ$  MTB from Figure 5.1 (b). It can be seen that the MTB is not as sharp or as straight as a coherent twin boundary. Based on fast fourier transform (FFT) analysis, we found that a total of 3 dislocations exist on MTB. Furthermore, they appear regularly spaced by 9 to 11  $\{111\}$  planes. This is consistent with the proposed mechanism. Due to the low density of residual dislocations at MTB, i.e., a  $2/9 \mathbf{A}\delta$  residual dislocation for every 9 slip planes, the lattice distortion is relatively low. This configuration is stable and has the lowest energy.

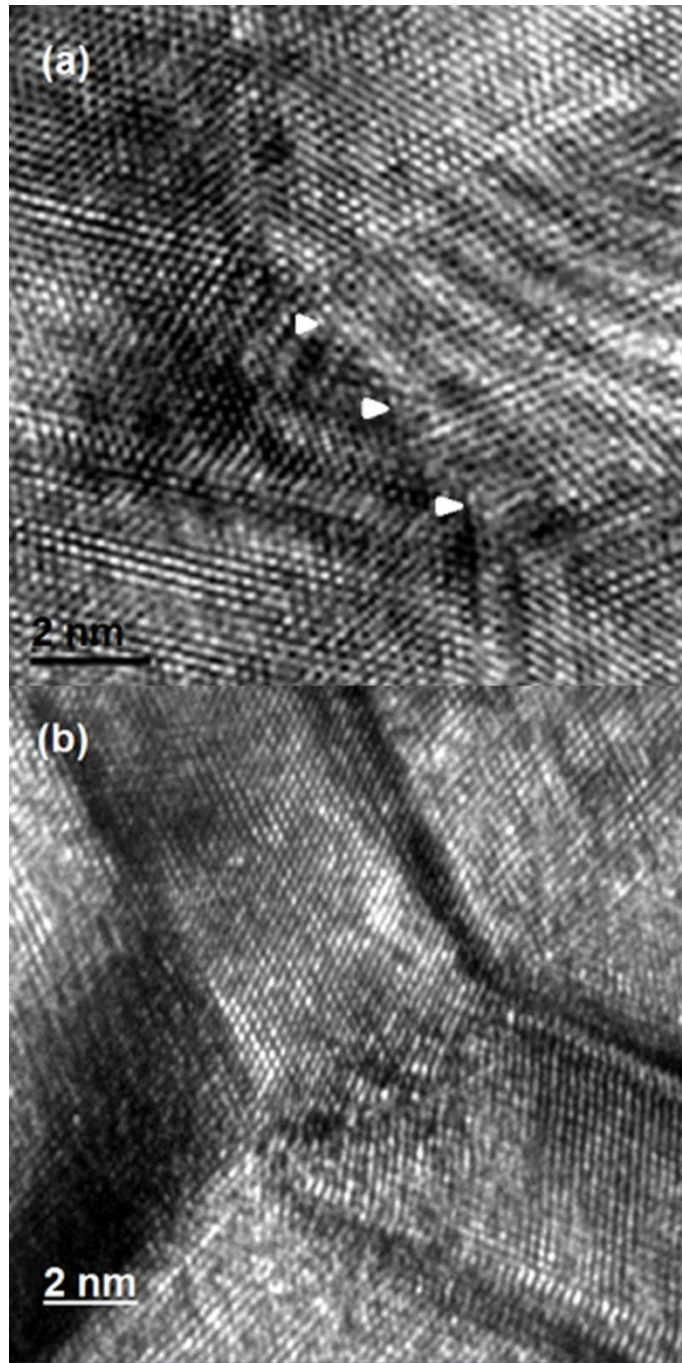


Figure 5.4 (a) An HRTEM image enlarged from the MTB area in Figure 5.1 (a); (b) An HRTEM image enlarged from the MTB area in Figure 5.1 (c).

Figure 5.4 (b) shows the enlarged region of MTB in Figure 5.1 (d), in which MTB first coincides with BTB and then forms an angle of  $\sim 43^\circ$  with BTB. As shown, the atomic image close to the MTB is more blurred than those far away from the MTB, indicating a high lattice distortion caused by high local elastic strain. This is consistent with the high residual dislocation content on the MTB as discussed previously. In addition, both the  $43^\circ$  MTB and  $0^\circ$  MTB appear crooked instead of linear because these two configurations have relatively high energy and are not stable. This is also evident in the schematic illustration in Figure 5.3 (c), in which lattice cannot match perfectly at MTB.

Generally speaking, if an MTB deviates from the BTB, the twin thickness ( $d_{IT}$  and  $d_{TT}$ ), the number of planes (M and N), and  $\theta$  will have the following relationship according to the geometric relationship shown in Figure 5.3 (a):

$$d_{IT} / d_{TT} = M / N = \sin(109.5^\circ - \theta) / \sin(70.5^\circ - \theta)$$

The above equation can be used to analyze twin transmission phenomenon in other twin transmission scenarios observed in the future, allowing the prediction of  $\theta$  and other variables.

## 5.4 Conclusions

In an fcc system, twin transmission occurs through partial dislocation reactions at the twin boundary. If not all of the partials transmit across the twin boundary, the twin boundary will deviate from the original configuration. The deviation angle is related to the ratio between the number of incident partials and that of transmitted partials. Therefore, the observations and mechanisms reported here can be used to explain twin intersections in fcc metals.

## References

- [1] K. Lu, L. Lu, S. Suresh, *Strengthening Materials by Engineering Coherent Internal Boundaries at the Nanoscale*. Science 2009;324(5925):349-352.
- [2] L. Lu, Y.F. Shen, X.H. Chen, L.H. Qian, K. Lu, *Ultrahigh strength and high electrical conductivity in copper*. Science 2004;304(5669):422-426.
- [3] M. Sennour, S. Lartigue-Korinek, Y. Champion, M.J. Hytch, *HRTEM study of defects in twin boundaries of ultra-fine grained copper*. Philosophical Magazine 2007;87(10):1465-1486.
- [4] Y.T. Zhu, J. Narayan, J.P. Hirth, S. Mahajan, X.L. Wu, X.Z. Liao, *Formation of single and multiple deformation twins in nanocrystalline fcc metals*. Acta Materialia 2009;57(13):3763-3770.
- [5] J. Jin, S.A. Shevlin, Z.X. Guo, *Multiscale simulation of onset plasticity during nanoindentation of Al (001) surface*. Acta Materialia 2008;56(16):4358-4368.
- [6] I. Shabib, R.E. Miller, *Deformation characteristics and stress-strain response of nanotwinned copper via molecular dynamics simulation*. Acta Materialia 2009;57(15):4364-4373.
- [7] Y.H. Zhao, Y.T. Zhu, X.Z. Liao, Z. Horita, T.G. Langdon, *Tailoring stacking fault energy for high ductility and high strength in ultrafine grained Cu and its alloy*. Applied Physics Letters 2006;89(12).

- [8] J.W. Christian, S. Mahajan, *Deformation twinning*. Progress in Materials Science 1995;39(1-2):1-157.
- [9] M.A. Meyers, O. Vohringer, V.A. Lubarda, *The onset of twinning in metals: A constitutive description*. Acta Materialia 2001;49(19):4025-4039.
- [10] X.Z. Liao, Y.H. Zhao, Y.T. Zhu, R.Z. Valiev, D.V. Gunderov, *Grain-size effect on the deformation mechanisms of nanostructured copper processed by high-pressure torsion*. Journal of Applied Physics 2004;96(1):636-640.
- [11] X.Z. Liao, Y.H. Zhao, S.G. Srinivasan, Y.T. Zhu, R.Z. Valiev, D.V. Gunderov, *Deformation twinning in nanocrystalline copper at room temperature and low strain rate*. Applied Physics Letters 2004;84(4):592-594.
- [12] Y.T. Zhu, X.Z. Liao, *Formation mechanism of fivefold deformation twins in nanocrystalline face-centered-cubic metals*. Applied Physics Letters 2005;86(10).
- [13] X. Wu, Y.T. Zhu, M.W. Chen, E. Ma, *Twinning and stacking fault formation during tensile deformation of nanocrystalline Ni*. Scripta Materialia 2006;54(9):1685-1690.
- [14] X.Z. Liao, F. Zhou, E.J. Lavernia, D.W. He, Y.T. Zhu, *Deformation twins in nanocrystalline Al*. Applied Physics Letters 2003;83(24):5062-5064.
- [15] Z. Shan, E.A. Stach, J.M. Wiezorek, J.A. Knapp, D.M. Follstaedt, S.X. Mao, *Grain boundary-mediated plasticity in nanocrystalline nickel*. Science 2004;305(5684):654-657.
- [16] S. Hai, E.B. Tadmor, *Deformation twinning at aluminum crack tips*. Acta Materialia 2003;51(1):117-131.

- [17] R.J. Asaro, S. Suresh, *Mechanistic models for the activation volume and rate sensitivity in metals with nanocrystalline grains and nano-scale twins*. *Acta Materialia* 2005;53(12):3369-3382.
- [18] X. Wu, Y. Zhu, *Inverse Grain-Size Effect on Twinning in Nanocrystalline Ni*. *Physical Review Letters* 2008;101(2).
- [19] J.-Y. Zhang, G. Liu, R.H. Wang, J. Li, J. Sun, E. Ma, *Double-inverse grain size dependence of deformation twinning in nanocrystalline Cu*. *Physical Review B* 2010;81(17).
- [20] T. Roland, D. Reintant, K. Lu, J. Lu, *Enhanced mechanical behavior of a nanocrystallised stainless steel and its thermal stability*. *Materials Science and Engineering a-Structural Materials Properties Microstructure and Processing* 2007;445281-288.
- [21] C. Efstathiou, H. Sehitoglu, *Strain hardening and heterogeneous deformation during twinning in Hadfield steel*. *Acta Materialia* 2010;58(5):1479-1488.
- [22] Y.T. Zhu, X.Z. Liao, X.L. Wu, *Deformation twinning in nanocrystalline materials*. *Progress in Materials Science* 2012;57(1):1-62.
- [23] Y.T. Zhu, X.Z. Liao, S.G. Srinivasan, E.J. Lavernia, *Nucleation of deformation twins in nanocrystalline face-centered-cubic metals processed by severe plastic deformation*. *Journal of Applied Physics* 2005;98(3):034319.
- [24] Y.T. Zhu, X.Z. Liao, X.L. Wu, J. Narayan, *Grain size effect on deformation twinning and detwinning*. *J Mater Sci* 2013;48(13):4467-4475.

- [25] H.M. Wen, E.J. Lavernia, *Twins in cryomilled and spark plasma sintered Cu-Zn-Al*. Scripta Materialia 2012;67(3):245-248.
- [26] F. Wu, Y. Zhu, J. Narayan, *Grain size effect on twin density in as-deposited nanocrystalline Cu film*. Philosophical Magazine 93 (35), 4355-4363.
- [27] Y.B. Wang, B. Wu, M.L. Sui, *Dynamical dislocation emission processes from twin boundaries*. Applied Physics Letters 2008;93(4).
- [28] Y.T. Zhu, X.L. Wu, X.Z. Liao, J. Narayan, L.J. Kecskés, S.N. Mathaudhu, *Dislocation-twin interactions in nanocrystalline fcc metals*. Acta Materialia 2011;59(2):812-821.

## Chapter 6

### Macroscopic strain by twinning in nanocrystalline Cu

Most deformation twins in nanocrystalline fcc metals are reported to produce zero-macrostrain, which is attributed to either random activation of partials (RAP) or cooperative slip of three partials (CSTP). In this chapter we found that when the RAP mechanism is suppressed, ~44% twins in nanocrystalline Cu produced zero-macrostrain via the CSTP mechanism. This indicates that both RAP and CSTP are major mechanisms to generate zero-macrostrain twins. In addition, our results also indicate that stress state affects the twinning mechanism in nanocrystalline fcc metals, and monotonic activation of partials with the same Burgers vector dominates twin formation under monotonic stress.

#### 6.1 Introduction

Nanocrystalline (NC) materials deform via mechanisms that are different from their coarse-grained counterparts [1, 2]. For example, deformation twinning has been frequently observed even in NC face-centered cubic (fcc) materials that do not deform

by twinning in their coarse-grained counterparts [2, 3]. Formation of twins in NC metals [2, 4, 5] plays a critical role in their physical and mechanical properties, such as good electrical conductivity, and excellent resistance to current-induced diffusion [6, 7]. The interactions between twins and gliding dislocations at twin boundaries have been observed both experimentally [7-14] and by molecular dynamics (MD) simulations [15-18] to result in an unusual combination of ultrahigh strength and high ductility [7, 9, 19-24]. In NC materials, MD simulations [25-27] have predicted that single or multiple deformation twins can be formed by emission of Shockley partial dislocations on adjacent  $\{111\}$  planes from grain boundaries. This formation mechanism has been confirmed later by abundant experimental evidence [3, 28-34].

One of the most salient features of deformation twins in NC fcc metals is that most of them produce very little or even zero macroscopic strain [23, 35-39]. A deformation twin is formed by the slip of multiple partials. While the slip of an individual partial produces local strain, the net strain from slips of multiple partials could sum to zero on a macroscopic scale, producing a deformation twin with zero macro-strain. This is in sharp contrast to a deformation twin in conventional coarse-grained fcc metals, which is usually produced by the slip of partials with the same Burgers vectors and produce a macroscopic strain. Whether deformation twins in NC metals produce macroscopic strain may have significant effect on their microstructural evolution and mechanical behavior during tensile testing. For example, it is known that grain rotation [40-42]

and grain boundary sliding [40] occurs extensively during the deformation of NC metals, which may lead to grain growth. Deformation twins that do not produce macroscopic strain will result in a smooth grain boundary [23], which will make grain rotation and grain boundary sliding easier. Therefore, it is of great importance to understand how the microstructures and stress conditions affect the formation of twins with zero macroscopic strain.

Two mechanisms have been proposed for deformation twins with zero macroscopic strain. One is the random activation of partials (RAP) mechanism by Wu et al. [23], in which partial dislocations with different Burgers vectors are randomly activated. The RAP mechanism was proposed to require the change of local stress orientation with time during deformation, so that the resolved shear stress on partials with different Burgers vectors varied with time during the deformation. Grain rotation and grain boundary sliding were believed to promote the RAP mechanism. The other mechanism was proposed by Wang et al. [35-38] and Li et al [39], which involved the cooperative slip of three partials (CSTP) with the sum of their Burgers vectors equaling zero, generating twins with zero macrostrain. This mechanism does not require the variation of local stress orientation. This raises a critical issue: which mechanism plays a major role in the formation of deformation twins with zero macrostrain in NC fcc metals? To complicate this issue further, monotonic activation of partial dislocations (MAP) with

the same Burgers vector was also found in NC fcc metals [19]. Although the MAP twins are in small percentage, they form under the same condition as the CSTP twins.

To solve this issue, the RAP in NC Cu grains is suppressed by a design of a layer-by-layer microstructure, to deter the grain rotation and grain boundary sliding of NC Cu grains during the deformation. In addition, the nanograins are textured to have their {111} planes parallel to the film surface, and the residual stress is oriented to have resolved shear stress on one type of partial dislocations only. Such a microstructure and stress state not only suppresses the RAP mechanisms, but also should promote the CSTP mechanism and the MAP mechanism. This unique experimental design should be able to clarify if CSTP or RAP or both mechanisms play a significant role in the formation of twins with zero macrostrain. If most twins still produce a zero-macrostrain when RAP is suppressed, the CSTP mechanism should be the dominating mechanism. On the other hand, if only a very small fraction of twins produce zero-macrostrain, the RAP mechanism is likely the dominating mechanism in the previous report [23], and the MAP mechanism should be the dominant mechanism in the current experiment. However, if the fraction of twins that produce zero-macrostrain is close to, but less than, 50%, both RAP and CSTP mechanisms should have played a significant role in the formation of zero-macrostrain twins reported earlier [23].

## 6.2 Experimental Approach

The Cu/Ta multilayer nanostructures were produced using PLD in a multi-target stainless-steel chamber using a pulsed KrF excimer laser (wavelength 248 nm, pulse duration  $25 \times 10^{-9}$  s, repetition rate 10 Hz). The targets were 4N purity Cu sheet and Ta sheet obtained from ESPI Metals Inc. The detailed PLD parameters and process can be found in our previous publications [12, 43]. The Ta layer was introduced in a controlled way to interrupt the growth of the columnar structure of Cu, and to constraint the equiaxed Cu grains. The thicknesses of Cu and Ta layers were controlled by manipulating the exposure durations of Cu and Ta targets to the laser beam.

X-Ray Diffraction (XRD) analysis was carried out using a Rigaku X-ray diffractometer with Cu-K $\alpha$  radiation ( $\lambda=0.154$  nm). XRD  $\theta$ - $2\theta$  scan patterns were utilized to determine the out-of-plane orientation and planar spacing of the Cu films, which were used to calculate the in-plane and out-of-plane strain of Cu films. Si (400) peaks were used as the internal reference standard for the estimation of strain. The strains for Si/Cu systems are limited to regions of the order of 10 nm, close to the Cu/Si interface. Since x-ray diffraction probes distances of the order of microns, the Si (400) peaks can provide the internal standard without being affected by interfacial strains. These strains will contribute slightly to the width of the peak, but the positions of Si (400) peaks will remain unchanged. The microstructures of these films were characterized using a JEOL-2000FX Transmission Electron Microscope (TEM). Twins in

Cu films and NC Cu grains were observed from the cross-section of the film using a JEOL-2010F High-Resolution Transmission Electron Microscope (HRTEM), equipped with a Gatan image filter (GIF) tuning attachment, which has a point-to-point resolution of 0.18 nm. The sample for TEM observation was prepared using conventional sample preparation techniques including mechanical polishing, dimpling, and Ar ion milling by using Precision Ion Polishing System (PIPS) at beam energy of 5 KeV, incidence angle of 5° during the initial stage and beam energy of 3 KeV, incidence angle of 2° during the final stage. The sample for HRTEM observation was further ion-milled for 15 minutes at beam energy of 3 KeV and incidence angle of 1°.

## **6.3 Results and Discussion**

### **6.3.1 Texture and Stress State of the Cu Film**

XRD analysis was used to determine the texture and residual stress of the Cu films. Figure 6.1 shows the XRD  $\theta$ - $2\theta$  scan patterns for 5 different Cu/Ta multilayer films integrated on Si substrates. Only a single Cu {111} peak appears in these 5 patterns, indicating that the NC Cu grains inside these multilayer films are highly textured with the {111} planes parallel to the film surface. However, the position of the {111} peak varies from sample to sample, suggesting a variation in the spacing of the {111} planes

that are parallel to the surface. Take film 1 as an example, the Cu {111} peak is measured to be located at the position of  $2\theta = 43.0869^\circ$ .

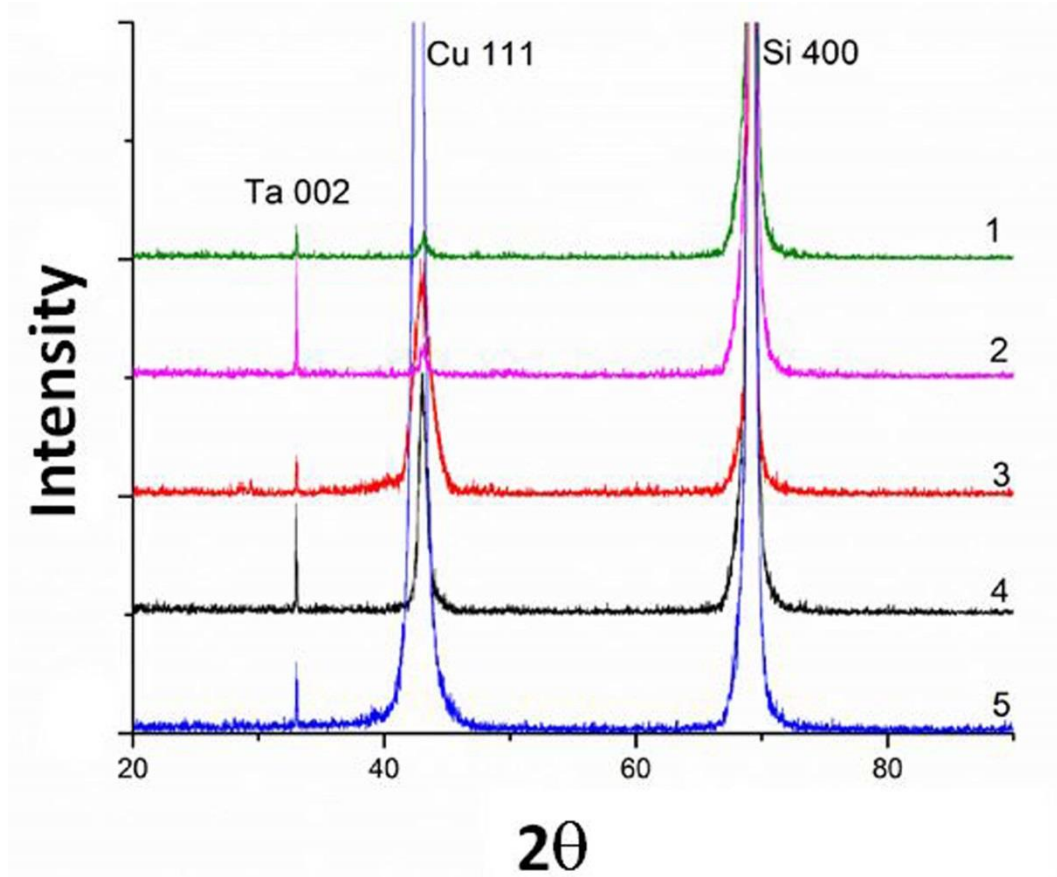


Figure 6.1: XRD  $\theta$ - $2\theta$  scan patterns for 5 different Cu/Ta multilayer films integrated on Si substrates.

According to the Bragg Law ( $2d \sin\theta = \lambda$ ), the planar spacing of Cu {111} planes parallel to the surface is calculated to be  $d_{//} = 2.0977\text{\AA}$ . Consequently the lattice constant of Cu along the out-of-plane direction is  $a_{zz} = \sqrt{3}d_{//} = 3.6333\text{\AA}$ . Since the standard lattice constant of Cu is  $3.610\text{\AA}$ , the out-of-plane strain  $\varepsilon_{zz}$  of the Cu film can thus be calculated to be  $0.6448\%$  (See Figure 6.2 for the orientation of coordinates).

According to the generalized relationship between stress and strain tensors in cubic crystals [44], the stresses and strains along different directions are related to each other [45]. Combine these relationships with the equation among the out-of-plane strain  $\varepsilon_{zz}$ , in-plane strain  $\varepsilon_{xx}$ ,  $\varepsilon_{yy}$  and Poisson's ratio  $\nu$ , i.e.,  $(\varepsilon_{zz} / (\varepsilon_{xx} + \varepsilon_{yy})) = -\nu / (1-\nu)$  [45], we can obtain the in-plane and out-of-plane stresses in film 1:  $\sigma_{xx} = \sigma_{yy} = -1.17\text{ GPa}$ , and  $\sigma_{zz} = 0\text{ GPa}$ . The routine procedure to calculate in-plane and out-of-plane stresses in thin films from out-of-plane strain can also be found in the text [46]. Note that these values calculated from X-ray data may not be very accurate and can only be considered qualitative. The residual stress in thin film heterostructures results from three sources: lattice mismatch, thermal mismatch and defects [45]. Since the Cu films are not epitaxial layers on Si and the PLD depositions were conducted at room temperature, thermal and lattice mismatches can not be the strain sources for Cu films in this case. Consequently, the accumulated compressive in-plane stresses within Cu films are due to defects in the Cu layers or at the Cu/Ta interfaces.

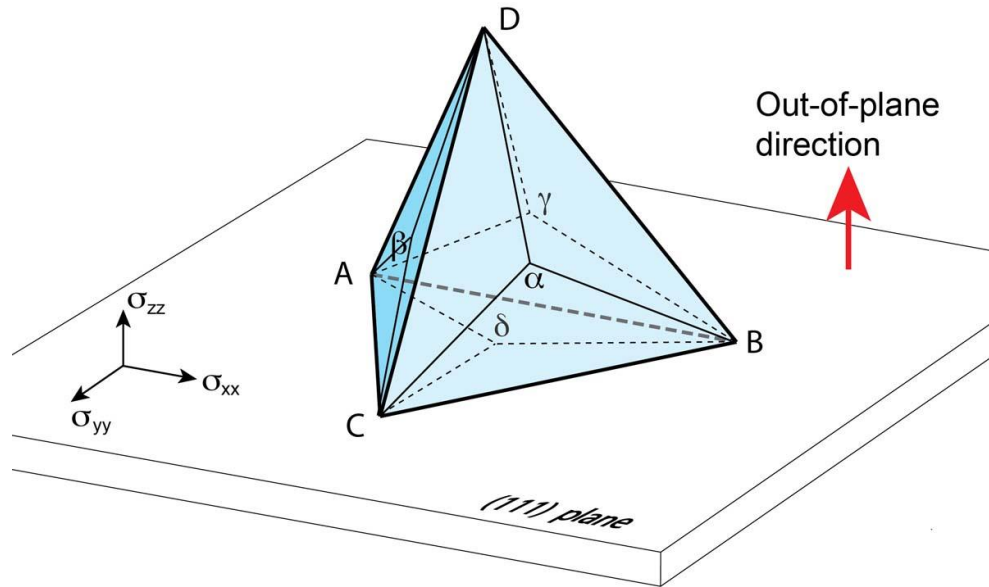


Figure 6.2: Schematic illustration of  $\sigma_{xx}$ ,  $\sigma_{yy}$ ,  $\sigma_{zz}$  and different  $\{111\}$  planes of Cu within the multilayer structure.

The orientations of  $\sigma_{xx}$ ,  $\sigma_{yy}$ ,  $\sigma_{zz}$  and different  $\{111\}$  planes of Cu within the multilayer structure are illustrated in Figure 6.2. Since  $\sigma_{xx}$ ,  $\sigma_{yy}$  and  $\sigma_{zz}$  are all normal stresses, the Shockley partial dislocations on ABC plane cannot glide. However, since planes BCD, ABD and ACD form an angle of  $70.5^\circ$  with plane ABC, the shear components of  $\sigma_{xx}$ ,  $\sigma_{yy}$ , and  $\sigma_{zz}$  will encourage the partial dislocations to glide on them and possibly generate twins. Consider plane BCD in film 1 as an example, the shear stress on Shockley partial  $\alpha\mathbf{D}$  can be calculated as 1.10 GPa, which is much higher than the stress needed to activate twinning [47]. Therefore, the twins observed here are deformation

twins. In addition, the statistical grain size effect on the twin density also indicates that the twin in the NC CU are mostly deformation twins [43]. The shear stresses on Shockley partial dislocations  $B\alpha$  or  $C\alpha$  are 0.55 GPa, which is close to the critical shear stress. Therefore, for the majority of NC Cu grains in these multilayer films, the emission and slip of  $\alpha D$  partial dislocations will be dominant on the BCD planes. For the same reason,  $\beta D$  partial dislocations will be dominant on the ACD planes and  $\gamma D$  partial dislocations will be dominant on the ABD planes. This indicates that the strain condition within our films drives the CSTP mechanism and the MAP mechanism, while suppressing the RAP mechanism.

### 6.3.2 Microstructure in the Cu/Ta Film

Figure 6.3 (a) shows the cross-sectional dark field (DF) image of a Cu/Ta/Si multilayer structure, in which 26 layers of thin Cu films are separated by 25 much thinner layers of Ta. The Cu grains inside each layer of the film were constrained by the thin Ta layers, such that columnar growth of Cu was interrupted and a majority of near equi-axed NC grains were obtained. In addition, the grain rotation and grain boundary sliding in the NC Cu are confined by the Ta layers, making it difficult for them to rotate along the thickness direction. Figure 6.3 (b) is the cross-sectional DF image of another Cu/Ta/Si multilayer structure, in which 50 layers of NC Cu are separated by 49 much

thinner layers of Ta. Based on the TEM observation of the as-grown Cu/Ta/Si multilayer structures, we found that the majority of the NC Cu grains were equi-axed and the grain sizes of these NC Cu grains range from  $\sim 10$  to  $\sim 80$  nm. The layer thicknesses and grain size ranges for films 1 to 5 are summarized in Table 6.1. A typical  $\langle 110 \rangle$  zone-axis selected area diffraction pattern (SADP) of one Si/Cu/Ta multilayer heterostructure is shown in Figure 6.3 (c). The  $\langle 110 \rangle$  zone-axis pattern of Si reveals the single-crystal nature of the substrate. However, the scattered diffraction points on the red circle shows that Cu layers are  $\{111\}$  textured. Ta layers are too thin to show visible diffraction spots on the SADP. Figure 6.3 (d) is the corresponding HRTEM image showing the structure of Cu/Ta layers and the interface morphology. The Ta layers appear darker than Cu layers due to mass contrast, which results from the higher atomic number of Ta. Ta layers are only a few monolayers thick, and their crystal structure is highly defected. The interfaces between Cu and Ta layers are clean and smooth. As shown, each Cu layer is made of a monolayer of Cu grains between adjacent Ta layers. Ta can effectively prevent Cu diffusion, because Cu and Ta are almost completely immiscible and will not react to form any compounds according to their phase diagram [48].

Table 6.1 The layer thicknesses and grain size ranges for films 1 to 5

<b>Film</b>	<b>Layer thickness (nm)</b>	<b>Grain size range(nm)</b>
#1	6~18	5~20
#2	20~30	18~30
#3	45~49	30~50
#4	62~66	50~68
#5	80~85	60~85

The reason for the activation of the RAP [23] has been attributed to the unique deformation behavior of NC materials, i.e. variation with time of the local shear stresses [23]. The grain boundary sliding and grain rotation can alter local stress state [49] or change the orientation of the twinned grain, which can promote the random emission of partial dislocations [23]. In our NC Cu/Ta films, the Cu-Ta interface restricts the rotation of the Cu grains, which consequently suppresses the RAP mechanism.

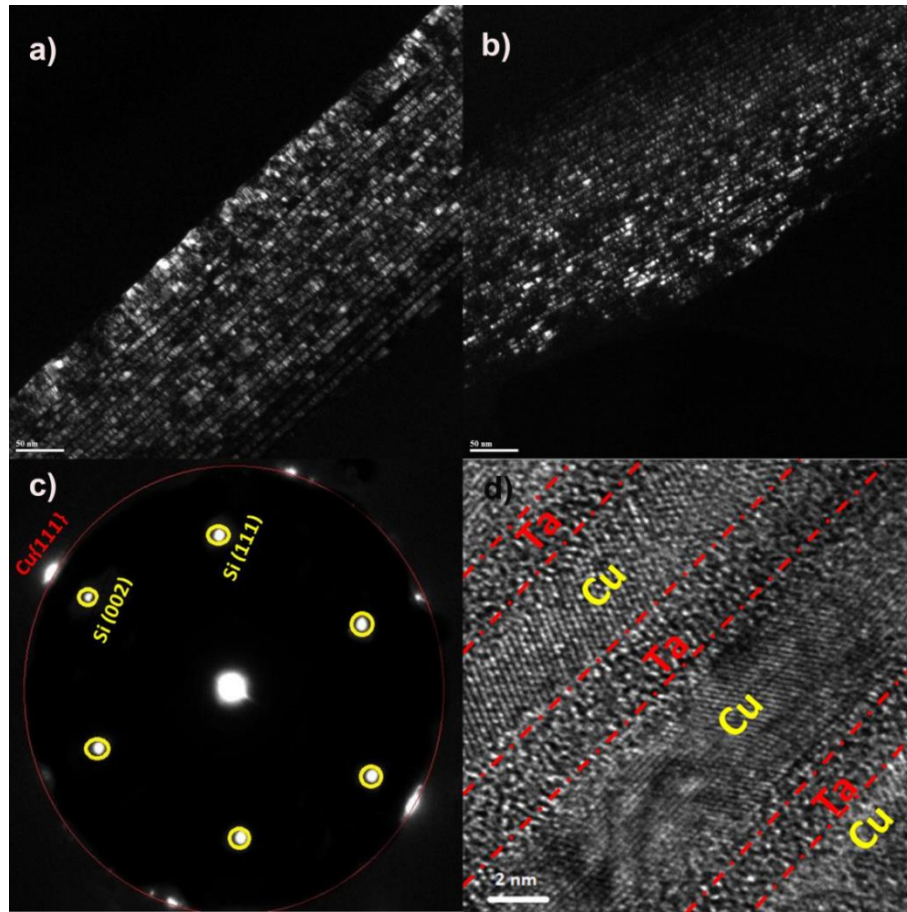


Figure 6.3 a) Cross-sectional dark field (DF) image of a typical Cu/Ta multilayer film on Si substrate. b) Cross-sectional dark field (DF) image of another Cu/Ta multilayer structure on Si substrate. c). The typical  $\langle 110 \rangle$  zone-axis selected area diffraction pattern (SADP) of the Si/Cu/Ta multilayer heterostructure. Cu layers are  $\{111\}$  textured, while Ta layers are too thin to show diffraction spots on the SADP. d) The typical HRTEM image showing the structure of Cu/Ta layers and the interface morphology.

### 6.3.3 Twins with Zero Macrostrain

Twins with zero macroscopic strain can be identified by the smooth grain boundary segments at locations where they intersect the twin boundaries (TB) [23]. Figure 6.4 shows HRTEM images of typical NC Cu grains containing twins with zero macroscopic strain. In Figure 6.4 (a), Shockley partials were emitted from the grain boundary, which glided on successive  $\{111\}$  planes across the whole grain to the other side of the grain. The grain boundary was smooth at the intersection locations with TBs, indicating a zero macroscopic strain. In Figure 6.4 (b), the Shockley partials were emitted from the grain boundary and glided on successive  $\{111\}$  planes but terminated inside the grain. Except for some Moire fringes on the left side of the grain boundary, no shape change of the grain boundary occurred, indicating again a zero macroscopic strain associated with the twinning process. Considering that the RAP mechanism [18] has been suppressed in our films, the zero-macrostrain twins were more likely to be formed via the CSTP mechanism, in which groups of three Shockley partial dislocations with different Burgers vectors cooperatively glide [35]. Assuming  $\mathbf{b}_1$ ,  $\mathbf{b}_2$  and  $\mathbf{b}_3$  are the three possible Shockley partial dislocations in a group, then  $\mathbf{b}_1+\mathbf{b}_2+\mathbf{b}_3=\mathbf{0}$ .

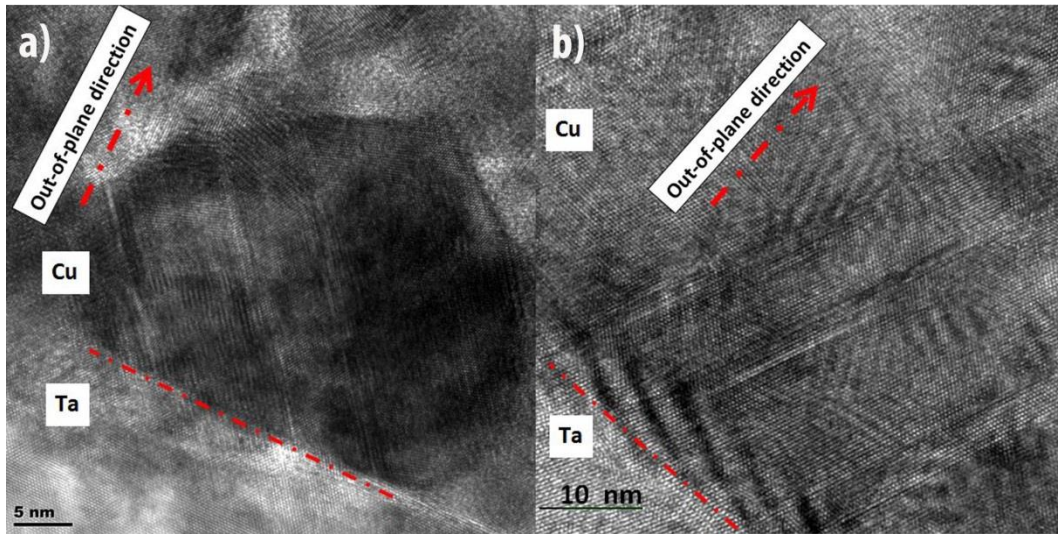


Figure 6.4: Typical NC Cu twinned grains with zero macroscopic strains, as manifested by smooth grain boundaries. The out-of-plane direction is shown as the arrow.

#### 6.3.4 Twins with Macrostrain

Most twins in our films were found to generate macroscopic strains, as manifested by the shape change of grain boundaries. To study the occurring frequencies of twinning with and without macrostrain, we observed 54 grains containing twins, among which 24 have smooth grain boundaries and the other 30 have kink angles on their boundaries. In other words, macrostrains were generated in  $\sim 56\%$  of the twinned grains due to the twinning process, which is in sharp contrast with previous reports in

NC materials [23, 35-39]. This result shows that with RAP suppressed, zero-macrostrain twins cease to dominate in our NC Cu grains. This indirectly proves that the RAP mechanism played a significant role in producing deformation twins with zero macrostrain. The result also means that the CSTP mechanism accounted for at least 44% of the deformation twins with zero-macrostrain in the current experiment, suggesting that CSTP is also a major mechanism for producing deformation twins with zero macrostrain.

The activation condition of the RAP mechanism is different from that of the CSTP [35-39] mechanism. The former requires the dynamic change in stress orientation so that partials with different Burgers vector can be activated randomly from the grain boundaries. In contrast, if the local stress remains unidirectional without change in orientation, the monotonic activation of partials (MAP) will be favored to produce macroscopic twinning strain, while at the same time the CSTP mechanism will be also favored to produce twins with zero macrostrain, as observed in this experiment. During the deformation of a NC fcc metal, some grains may rotate. In other words, both RAP and CSTP are major mechanisms for producing deformation twins with zero macrostrain.

Figure 6.5 shows typical NC Cu grains in which macroscopic strains were generated by twins. In Figure 6.5 (a), multiple twins are adjacent to each other and a large shear strain exists at each location where the TB intersects with the grain

boundary. Two kink angles of the shear-strained grain boundary can be readily measured, where the upper kink angle is  $145^{\circ} \pm 2^{\circ}$  and the lower kink angle is close to  $141^{\circ}$ . In Figure 6.5 (b) there is only one kink angle on the grain boundary and it is found to be close to  $141^{\circ}$ . Figure 6.5 (c) shows an elongated grain whose width (i.e. the distance between the left and right sides of the grain) is about 14 nm. Two twins are adjacent to each other and the Shockley partial dislocations were emitted from one side of the grain boundary and glided across the whole grain until they reach the other side of the grain boundary. A grain boundary kink exists at each location where the TB intersects with the grain boundary. The upper grain boundary kink angle is  $157^{\circ} \pm 2^{\circ}$ , and the lower kink angle is close to  $141^{\circ}$ . Figure 6.5 (d) shows a  $\sim 35$  nm NC Cu grain in which one TB intersects with both the top and bottom sides of the grain boundary, generating a macroscopic strain. Both the upper and lower kink angles are close to  $141^{\circ}$ .

The macrostrain of the grains containing twins can be generated through two mechanisms:

- 1) Monotonic activation of partials (MAP) [23], in which twinning partials with the same Burgers vector are emitted on every slip plane at the grain boundary to generate a twin with a large macroscopic strain [50]. For such a twin, the grain boundary kink angle will be  $141^{\circ}$  if viewed from the  $\langle 110 \rangle$  orientation perpendicular to the Burgers vector of the twinning partial, and it will be  $158^{\circ}$  if viewed from other possible  $\langle 110 \rangle$  orientations [50];

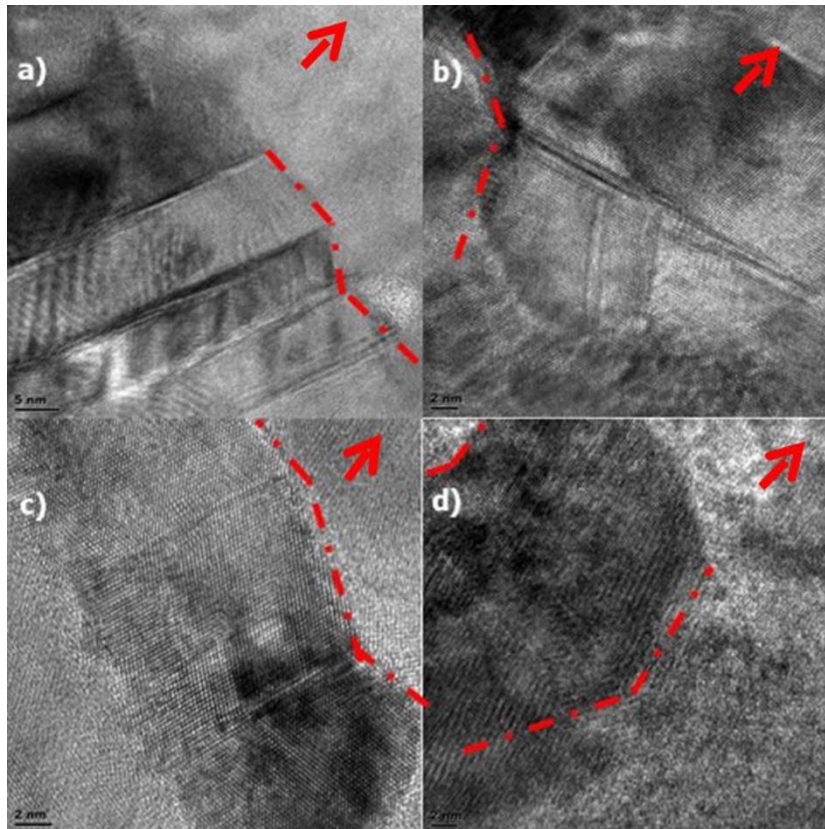


Figure 6.5: Typical NC Cu twinned grains with macroscopic strains, as manifested by shape change (kink angles) on grain boundaries. The out-of-plane direction for each part of the image is marked by the arrows.

2) The emission of partial dislocations with two different Burgers vectors, in which twinning partials with two different Burgers vectors are emitted alternatively at the grain boundary, such that the net sum of their Burgers vectors is equal to that of only one partial dislocation, and a twin with smaller shear strain is generated [50]. The grain

boundary kink angle will be  $158^\circ$  if viewed from the  $\langle 110 \rangle$  orientation perpendicular to the net sum of the two Burgers vectors of the twinning partial dislocations, and it will be  $169^\circ$  if viewed from other possible  $\langle 110 \rangle$  orientations [50].

It is also possible to form a twin by the mixture of the first and second mechanisms [50]. According to the above rationale, most of the twins in Figure 6.5 are formed by the MAP mechanism, while some may be formed by the second mechanism or a mixture of the two.

#### **6.4 Conclusions**

The Cu/Ta multilayer structure was carefully designed to obtain a texture and stress state to promote the monotonic activation of partials with the same Burgers vector and the cooperative slip of three partials. The confinement of grain boundary rotations helps maintain the local stress condition, such that the random activation of partials is suppressed. The results indicate that monotonic activation of partial dislocations with the same Burgers vector dominates twin formation under monotonic stress. The results also suggest that both random activation of partials and the cooperative slip of three partials are significant mechanisms for forming the previously reported zero-macrostrain twins in NC fcc metals.

## References

- [1] G.M. Cheng, W.Z. Xu, W.W. Jian, H. Yuan, M.H. Tsai, Y.T. Zhu, Y.F. Zhang, P.C. Millett, *Dislocations with edge components in nanocrystalline bcc Mo*. Journal of Materials Research 2013;28(13):1820-1826.
- [2] Y.T. Zhu, X.Z. Liao, X.L. Wu, *Deformation twinning in nanocrystalline materials*. Progress in Materials Science 2012;57(1):1-62.
- [3] X.Z. Liao, F. Zhou, E.J. Lavernia, S.G. Srinivasan, M.I. Baskes, D.W. He, Y.T. Zhu, *Deformation mechanism in nanocrystalline Al: Partial dislocation slip*. Applied Physics Letters 2003;83(4):632-634.
- [4] Y.T. Zhu, J. Narayan, J.P. Hirth, S. Mahajan, X.L. Wu, X.Z. Liao, *Formation of single and multiple deformation twins in nanocrystalline fcc metals*. Acta Materialia 2009;57(13):3763-3770.
- [5] J. Narayan, Y.T. Zhu, *Self-thickening, cross-slip deformation twinning model*. Applied Physics Letters 2008;92(15).
- [6] K.-C. Chen, W.-W. Wu, C.-N. Liao, L.-J. Chen, K.N. Tu, *Observation of Atomic Diffusion at Twin-Modified Grain Boundaries in Copper*. Science 2008;321(5892):1066-1069.
- [7] L. Lu, Y. Shen, X. Chen, L. Qian, K. Lu, *Ultrahigh Strength and High Electrical Conductivity in Copper*. Science 2004;304(5669):422-426.

- [8] X.Z. Liao, J.Y. Huang, Y.T. Zhu, F. Zhou, E.J. Lavernia, *Nanostructures and deformation mechanisms in a cryogenically ball-milled Al-Mg alloy*. Philosophical Magazine 2003;83(26):3065-3075.
- [9] K. Lu, L. Lu, S. Suresh, *Strengthening Materials by Engineering Coherent Internal Boundaries at the Nanoscale*. Science 2009;324(5925):349-352.
- [10] Y.B. Wang, M.L. Sui, *Atomic-scale in situ observation of lattice dislocations passing through twin boundaries*. Applied Physics Letters 2009;94(2).
- [11] Y.B. Wang, B. Wu, M.L. Sui, *Dynamical dislocation emission processes from twin boundaries*. Applied Physics Letters 2008;93(4).
- [12] F. Wu, H.M. Wen, E.J. Lavernia, J. Narayan, Y.T. Zhu, *Twin intersection mechanisms in nanocrystalline fcc metals*. Materials Science and Engineering: A 2013;585(0):292-296.
- [13] Y. Cao, Y.B. Wang, X.Z. Liao, M. Kawasaki, S.P. Ringer, T.G. Langdon, Y.T. Zhu, *Applied stress controls the production of nano-twins in coarse-grained metals*. Applied Physics Letters 2012;101(23):231903-231903-231905.
- [14] S. Ni, Y.B. Wang, X.Z. Liao, R.B. Figueiredo, H.Q. Li, S.P. Ringer, T.G. Langdon, Y.T. Zhu, *The effect of dislocation density on the interactions between dislocations and twin boundaries in nanocrystalline materials*. Acta Materialia 2012;60(6-7):3181-3189.
- [15] K.A. Afanasyev, F. Sansoz, *Strengthening in Gold Nanopillars with Nanoscale Twins*. Nano Letters 2007;7(7):2056-2062.
- [16] C.H. Henager Jr, R.G. Hoagland, *A rebound mechanism for misfit dislocation creation in metallic nanolayers*. Scripta Materialia 2004;50(5):701-705.

- [17] J. Jin, S.A. Shevlin, Z.X. Guo, *Multiscale simulation of onset plasticity during nanoindentation of Al (001) surface*. Acta Materialia 2008;56(16):4358-4368.
- [18] V. Yamakov, D. Wolf, S.R. Phillpot, H. Gleiter, *Dislocation–dislocation and dislocation–twin reactions in nanocrystalline Al by molecular dynamics simulation*. Acta Materialia 2003;51(14):4135-4147.
- [19] E. Ma, Y.M. Wang, Q.H. Lu, M.L. Sui, L. Lu, K. Lu, *Strain hardening and large tensile elongation in ultrahigh-strength nano-twinned copper*. Applied Physics Letters 2004;85(21):4932-4934.
- [20] Y.H. Zhao, J.E. Bingert, X.Z. Liao, B.Z. Cui, K. Han, A.V. Sergueeva, A.K. Mukherjee, R.Z. Valiev, T.G. Langdon, Y.T.T. Zhu, *Simultaneously increasing the ductility and strength of ultra-fine-grained pure copper*. Advanced Materials 2006;18(22):2949.
- [21] Z.W. Wang, Y.B. Wang, X.Z. Liao, Y.H. Zhao, E.J. Lavernia, Y.T. Zhu, Z. Horita, T.G. Langdon, *Influence of stacking fault energy on deformation mechanism and dislocation storage capacity in ultrafine-grained materials*. Scripta Materialia 2009;60(1):52-55.
- [22] Y.H. Zhao, X.Z. Liao, Z. Horita, T.G. Langdon, Y.T. Zhu, *Determining the optimal stacking fault energy for achieving high ductility in ultrafine-grained Cu-Zn alloys*. Materials Science and Engineering a-Structural Materials Properties Microstructure and Processing 2008;493(1-2):123-129.
- [23] X.L. Wu, X.Z. Liao, S.G. Srinivasan, F. Zhou, E.J. Lavernia, R.Z. Valiev, Y.T. Zhu, *New deformation twinning mechanism generates zero macroscopic strain in nanocrystalline metals*. Physical Review Letters 2008;100(9).

- [24] Y.H. Zhao, Y.T. Zhu, X.Z. Liao, Z. Horita, T.G. Langdon, *Tailoring stacking fault energy for high ductility and high strength in ultrafine grained Cu and its alloy*. Applied Physics Letters 2006;89(12).
- [25] V. Yamakov, D. Wolf, S.R. Phillpot, A.K. Mukherjee, H. Gleiter, *Deformation-mechanism map for nanocrystalline metals by molecular-dynamics simulation*. Nature Materials 2004;3(1):43-47.
- [26] V. Yamakov, D. Wolf, S.R. Phillpot, A.K. Mukherjee, H. Gleiter, *Dislocation processes in the deformation of nanocrystalline aluminium by molecular-dynamics simulation*. Nature Materials 2002;1(1):45-48.
- [27] V. Yamakov, D. Wolf, S.R. Phillpot, H. Gleiter, *Grain-boundary diffusion creep in nanocrystalline palladium by molecular-dynamics simulation*. Acta Materialia 2002;50(1):61-73.
- [28] M.W. Chen, E. Ma, K.J. Hemker, H.W. Sheng, Y.M. Wang, X.M. Cheng, *Deformation twinning in nanocrystalline aluminum*. Science 2003;300(5623):1275-1277.
- [29] X.Z. Liao, F. Zhou, E.J. Lavernia, D.W. He, Y.T. Zhu, *Deformation twins in nanocrystalline Al*. Applied Physics Letters 2003;83(24):5062-5064.
- [30] X.Z. Liao, Y.H. Zhao, S.G. Srinivasan, Y.T. Zhu, R.Z. Valiev, D.V. Gunderov, *Deformation twinning in nanocrystalline copper at room temperature and low strain rate*. Applied Physics Letters 2004;84(4):592-594.
- [31] X.L. Wu, E. Ma, *Deformation twinning mechanisms in nanocrystalline Ni*. Applied Physics Letters 2006;88(6).

- [32] Y.M. Wang, A.M. Hodge, J. Biener, A.V. Hamza, D.E. Barnes, K. Liu, T.G. Nieh, *Deformation twinning during nanoindentation of nanocrystalline Ta*. Applied Physics Letters 2005;86(10).
- [33] H. Rosner, J. Markmann, J. Weissmuller, *Deformation twinning in nanocrystalline Pd*. Philosophical Magazine Letters 2004;84(5):321-334.
- [34] X.L. Wu, Y.T. Zhu, *Inverse grain-size effect on twinning in nanocrystalline Ni*. Physical Review Letters 2008;101(2).
- [35] J. Wang, O. Anderoglu, J.P. Hirth, A. Misra, X. Zhang, *Dislocation structures of Sigma 3 {112} twin boundaries in face centered cubic metals*. Applied Physics Letters 2009;95(2).
- [36] J. Wang, N. Li, O. Anderoglu, X. Zhang, A. Misra, J.Y. Huang, J.P. Hirth, *Detwinning mechanisms for growth twins in face-centered cubic metals*. Acta Materialia 2010;58(6):2262-2270.
- [37] J. Wang, A. Misra, J.P. Hirth, *Shear response of Sigma 3{112} twin boundaries in face-centered-cubic metals*. Physical Review B 2011;83(6).
- [38] L. Liu, J. Wang, S.K. Gong, S.X. Mao, *High Resolution Transmission Electron Microscope Observation of Zero-Strain Deformation Twinning Mechanisms in Ag*. Physical Review Letters 2011;106(17).
- [39] B.Q. Li, B. Li, Y.B. Wang, M.L. Sui, E. Ma, *Twinning mechanism via synchronized activation of partial dislocations in face-centered-cubic materials*. Scripta Materialia 2011;64(9):852-855.

- [40] N.Q. Chinh, P. Szommer, Z. Horita, T.G. Langdon, *Experimental evidence for grain-boundary sliding in ultrafine-grained aluminum processed by severe plastic deformation*. *Advanced Materials* 2006;18(1):34-39.
- [41] X.Z. Liao, A.R. Kilmametov, R.Z. Valiev, H.S. Gao, X.D. Li, A.K. Mukherjee, J.F. Bingert, Y.T. Zhu, *High-pressure torsion-induced grain growth in electrodeposited nanocrystalline Ni*. *Applied Physics Letters* 2006;88(2).
- [42] Y.B. Wang, J.C. Ho, X.Z. Liao, H.Q. Li, S.P. Ringer, Y.T. Zhu, *Mechanism of grain growth during severe plastic deformation of a nanocrystalline Ni-Fe alloy*. *Applied Physics Letters* 2009;94(1).
- [43] F. Wu, Y.T. Zhu, J. Narayan, *Grain size effect on twin density in as-deposited nanocrystalline Cu film*. *Philosophical Magazine* 2013;1-9.
- [44] JP Hirth, J. Lothe, *Theory of dislocations*. (McGraw-Hill, New York, 1968).
- [45] J. Narayan, *Recent progress in thin film epitaxy across the misfit scale (2011 Acta Gold Medal Paper)*. *Acta Materialia* 2013;61(8):2703-2724.
- [46] S.S. L.B. Freund (Ed.) *Thin film materials: stress, defect formation, and surface evolution*, Cambridge University Press, New York 2003.
- [47] Y.T. Zhu, X.Z. Liao, S.G. Srinivasan, E.J. Lavernia, *Nucleation of deformation twins in nanocrystalline face-centered-cubic metals processed by severe plastic deformation*. *Journal of Applied Physics* 2005;98(3).
- [48] A.E. Kaloyeros, E. Eisenbraun, *Ultrathin diffusion barriers/liners for gigascale copper metallization*. *Annual Review of Materials Science* 2000;30(1):363-385.

[49] M.A. Meyers, A. Mishra, D.J. Benson, *Mechanical properties of nanocrystalline materials*. Progress in Materials Science 2006;51(4):427-556.

[50] Y.T. Zhu, X.L. Wu, X.Z. Liao, J. Narayan, S.N. Mathaudhu, L.J. Kecskes, *Twinning partial multiplication at grain boundary in nanocrystalline fcc metals*. Applied Physics Letters 2009;95(3).

## Chapter 7

# Controlled epitaxial growth of bcc and fcc Cu on MgO for integration on Si

The Cu/MgO interface plays a crucial role in applications. The fcc Cu has been reported to grow on MgO substrates (rock salt structure). However, no bcc(t) Cu has been stabilized on MgO. The special atomic structure of the bcc (bct)/rock salt interface contributes to superior thermal, mechanical and electrical properties. In this chapter, for the first time, the epitaxial growth of bcc(t) and fcc Cu on Si(100) and Si(111) substrates using MgO(100)/TiN(100) and MgO(111)/TiN(111) buffer layers by pulsed laser deposition. We find that the deposition temperature determines the structure of Cu. At high temperature, only fcc Cu grows on both MgO/TiN(100) and MgO/TiN(111) templates. At room temperature, an epitaxial layer of bcc(t) Cu grows pseudomorphically on a MgO(100) template up to the critical thickness, while on a MgO/TiN(111) template, the majority of Cu is fcc, and bcc(t) Cu exists occasionally in a three-dimensional island shape. The growth of these hetero-structures involves epitaxy across the misfit scale by matching MgO{200} planes with bcc(t) Cu{110} planes. The integration of Cu/MgO on the technologically important Si substrate holds tremendous

promise, because the novel bcc(t) Cu/MgO structure can be integrated with present-day microelectronic/nanoelectronic devices.

## 7.1 Introduction

Cu is the standard interconnection material in integrated circuits due to its superior electromigration resistance and lower bulk resistivity [1-3] compared to Al metallization [4-6]. However, due to the rapid diffusion of Cu into silicon [7-9], and the consequent degradation of the semiconductor devices, a barrier layer is needed [1]. MgO and TiN have been successfully utilized as good diffusion barriers for Cu for a long time [7, 10, 11]. Furthermore, the Cu/MgO interface is of great importance because it plays a crucial role in applications such as microelectronics packaging, coating and corrosion protection [12, 13], catalysis, metal–matrix composites, recording media, etc. [14]. The epitaxial growth of fcc Cu on MgO has been reported at different temperatures [15-18]. However, despite the growth of bcc Cu on substrates such as Nb [19], Ag [20] and Pd [21, 22], no bcc(t) Cu has been fabricated onto MgO, which has a rock salt structure. The special atomic structure of the fcc/bcc(t) interface is believed to contribute to superior thermal, mechanical and electrical properties [19, 23-25]. Consequently, the generation of bcc(t)/ rock salt interfaces between bcc(t) Cu and MgO is of great scientific significance, in addition to technological applications.

A MgO substrate is not suitable for practical applications[26] due to its high single-crystal cost, limited wafer size, and poor mechanical properties. By successfully fabricating an epitaxial MgO template on Si substrate using TiN as the buffer layer, we can fabricate the Cu/MgO stack for integration on the technologically-important silicon substrate, which is inexpensive, readily available, and widely used in present-day microelectronic devices. This holds tremendous promise because the novel bcc(t) Cu/MgO structure can be integrated with present-day microelectronic/nanoelectronic devices.

All of the previously reported bcc(t) Cu grow pseudomorphically on the substrates, either by matching the lattice [19], or by matching of the sides of a unit cell of bcc(t) Cu and a primitive square mesh on {001} planes of fcc substrates [20]. However, if bcc(t) Cu can be fabricated in a controlled way directly onto MgO(100) and MgO(111), domain matching epitaxy (DME) [27-29] should be considered along with the traditional lattice matching epitaxy(LME) due to the large lattice misfit (14.2%) between these two systems. For bcc(t) Cu/MgO(100), the interface planes are {100} planes for both Cu and MgO, thus the sides of a unit cell of bcc(t) Cu will match with the sides of a primitive square mesh on MgO{100}. For bcc(t) Cu/MgO(111), closed-packed atomic layers from both sides will be the interface planes for them, respectively[30]. This interface orientation relationship is in accord with the reported bcc/fcc systems[24, 31-33], and can be explained by the Kurdjumov-Sachs[34] (K-S) or Nishiyama-Wassermann (N-W)

orientation relationship. In both relationships, the common interface plane is  $\{111\}_{fcc} \parallel \{011\}_{bcc}$  [35]. However, for the K-S relationship, the perpendicular matching axes on the interfacial plane are  $[10-1]_{fcc} \parallel [11-1]_{bcc}$  and  $[-1-12]_{fcc} \parallel [-112]_{bcc}$ , while those for the N-W relationship are  $[1-10]_{fcc} \parallel [001]_{bcc}$  and  $[11-2]_{fcc} \parallel [01-1]_{bcc}$ .

In this chapter, I report the controlled epitaxial growth of bcc(t) and fcc Cu on both MgO(100)/TiN(100)/Si(100) and MgO(111)/TiN(111)/Si(111) by pulsed laser deposition (PLD). At high temperature, only fcc Cu grows on both MgO/TiN(100) and MgO/TiN(111) templates. At room temperature, bcc(t) Cu on MgO/TiN(100) template forms an epitaxial layer and grows pseudomorphically up to the critical thickness, corresponding to the transition where Gibbs free energy exceeds the strain free energy. However, the majority of Cu growing on a MgO/TiN (111) template is in the stable structure(fcc), and bcc(t) Cu will grow occasionally in a three-dimensional island. For both MgO/TiN(100) and MgO/TiN(111) templates, the growth of these heterostructures involves epitaxy across the misfit scale by matching MgO{200} planes with bcc(t) Cu{110} planes. To date, this is the first report in which bcc(t) Cu is obtained on fcc-structured MgO, and is the first systematic study on bcc(t) Cu on MgO templates with different orientations (MgO(100) and MgO(111)). This is also the first integration of Cu/MgO on the technologically important Si substrate. The orientation relationships between different phases were studied carefully by selected area diffraction patterns (SADP) and high resolution transmission electron microscopy (HRTEM).

## 7.2 Experimental Approach

Pulsed laser deposition (PLD) of each layer in the stack (Cu/MgO/TiN/Si) was carried out in a multi-target stainless-steel chamber using a pulsed KrF excimer laser (wavelength 248 nm, pulse duration 25 ns, repetition rate 10 Hz). Details about PLD can be found in earlier publications [36, 37]. The deposition of TiN film was done at 625 °C in vacuum ( $1 \times 10^{-6}$  Torr). After TiN deposition, the first few monolayers (for about 500 pulses) of MgO were deposited under vacuum ( $1 \times 10^{-6}$  Torr) at 575 °C. The remaining MgO was deposited at the same temperature with an oxygen pressure of  $6 \times 10^{-4}$  Torr. The deposition of Cu was carried out either at room temperature or  $\sim 300^\circ\text{C}$ . The deposition temperature determines the structure of Cu layer. The stable (fcc) structure of Cu is expected at high temperature because sufficient thermal energy is provided, while unstable (bcc(t)) structure of Cu is more likely to form at the Cu/MgO interface during room-temperature deposition. The microstructural characterization of the as-deposited films was performed by Transmission Electron Microscopy (TEM), and HRTEM [36]. TEM samples were prepared by the focused ion beam (FIB) technique.

## 7.3 Results and Discussion

To better understand the domain matching mechanism of bcc(t) Cu on a MgO buffer layer, both 3-D and 2-D atomic-structure models (viewed either parallel or

perpendicular to the interface plane) are shown in Figure 7.1. The phase with red balls stands for bcc(t) Cu, while the green phase stands for MgO. For bcc(t) Cu/MgO(100) system, the sides of a unit cell of bcc(t) Cu matches with the sides of a primitive square mesh on MgO(001) plane. The 3-D atomic-structure model demonstrating this crystallographic relationship is shown in Figure 7.1 (a), in which the unit cells of bcc(t) Cu and MgO are labeled and the interface plane is bcc(t) Cu{100}/MgO{100}. Figure 7.1 (b) is the 2-D atomic-structure model and the viewing direction is  $[001]_{\text{bcc(t) Cu}} \parallel [001]_{\text{MgO}}$ , perpendicular to the interface plane. Due to the 3% misfit between  $a_{\text{bcc Cu}}$  and  $a_{\text{MgO}}/\sqrt{2}$ , bcc(t) Cu will grow pseudomorphically on MgO so that the standard bcc unit cell will be elongated along x and y axes and compressed along z-axis. Figure 7.1 (c) is the 2-D atomic-structure model viewed from MgO[110]/bcc(t) Cu[100], parallel to the interface plane. The MgO{111} planes connect with bcc(t) Cu{110} planes, and the matching plane at the interface is MgO{200}/bcc(t) Cu{110}.

For comparison, the 3-D and 2-D atomic-structure models for bcc(t) Cu/MgO(111) system are shown on the right-hand side in Figure 7.1. Figure 7.1 (d) is the 3-D atomic-structure model demonstrating the crystallographic relationship between MgO and bcc(t) Cu. The interface plane is the close-packed planes for both materials (MgO{111} and bcc(t) Cu{110}) and the close-packed direction of MgO becomes the cube edge of bcc(t) Cu. Figure 7.1 (e) is the 2-D atomic-structure model viewed from  $\langle 011 \rangle_{\text{bcc(t) Cu}} \parallel \langle 111 \rangle_{\text{MgO}}$ , perpendicular to the  $\{110\}_{\text{bcc(t) Cu}} \parallel \{111\}_{\text{MgO}}$  interface plane.

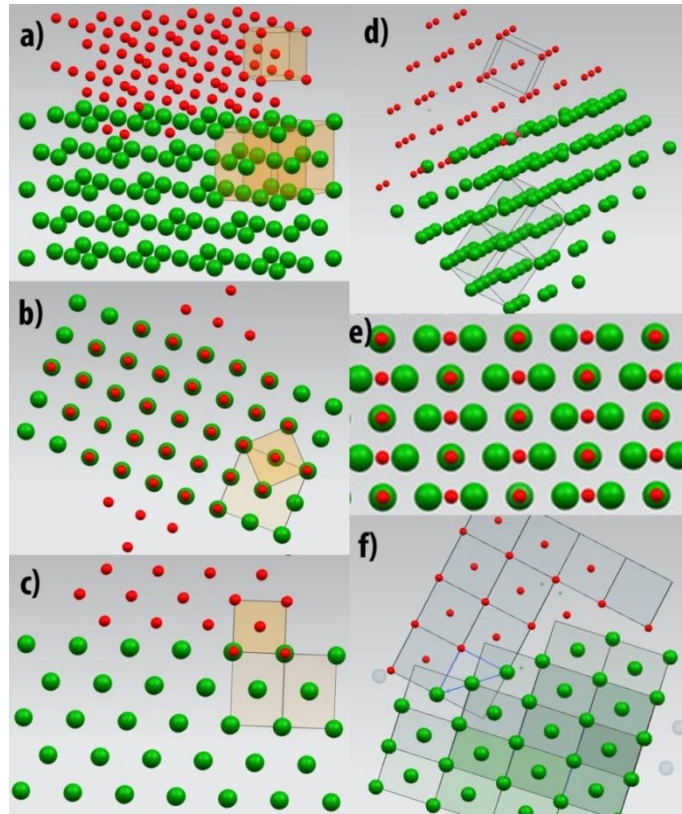


Figure 7.1: Schematic illustration of (a) 3-D atomic structure demonstrating the crystallographic relationship between bcc(t) Cu/MgO(100). (b) 2-D atomic structure of bcc(t) Cu/MgO(100), viewed along  $[001]_{\text{bcc(t) Cu}} \parallel [001]_{\text{MgO}}$ , perpendicular to the interface plane. (c) 2-D atomic structure of bcc(t) Cu/MgO(100), viewed parallel to the interface plane. (d) 3-D atomic structure demonstrating the crystallographic relationship between bcc(t) Cu/MgO(111). (e) 2-D atomic structure of bcc(t) Cu/MgO(111), viewed along  $[011]_{\text{bcc(t) Cu}} \parallel [-111]_{\text{MgO}}$ , perpendicular to the interface plane. (f) Schematic illustration of 2-D atomic structure of bcc(t) Cu/MgO(111), viewed parallel to the interface plane.

The {110} planes of bcc(t) Cu will be elongated along  $\langle 011 \rangle$  and  $\langle 100 \rangle$  directions to match with  $\langle 112 \rangle_{\text{MgO}}$  and  $\langle 110 \rangle_{\text{MgO}}$  respectively, corresponding to the N-W orientation relationship. Figure 7.1 (f) is the 2-D atomic-structure model viewed along  $[001]_{\text{bcc(t) Cu}} \parallel [110]_{\text{MgO}}$ , parallel to the interface plane. The  $\text{MgO}\{002\}$  planes connect with  $\text{bcc(t) Cu}\{110\}$  planes, such that planar spacing matching is accomplished. The planar spacing misfit between these two materials is calculated to be  $(d_{(002)\text{MgO}} - d_{(110)\text{bcc Cu}}) / d_{(002)\text{MgO}} = 3.19\%$ , much smaller than the lattice misfit ( $\sim 31.5\%$ ) between them.

Figure 7.2 (a) is a typical TEM bright-field cross-section image showing the whole stack Cu/MgO(100)/TiN(100)/Si(100). The Pt layer was deposited onto this stack for protection during the FIB sample preparation process. Individual Cu islands grow on the MgO(100) template, indicating a 3-D growth mode of Cu. The thicknesses of TiN, MgO and Cu are about 136 nm, 150nm and 40 nm, respectively. To study the microstructures of the buffer layers and the orientation relationships between them, selected area diffraction patterns (SADP) were obtained at each interface, as shown in Figure 7.2 (b) and (c). Figure 7.2 (b) shows the  $[110]$  zone-axis-pattern of Si/TiN interface, clearly demonstrating a cube-on-cube relationship between the TiN and Si substrate. Both  $\{002\}$  and  $\{111\}$  planes of TiN and Si align parallel to each other. The diffraction points corresponding to the same planes of TiN and Si split, but appear along the same directions due to the lattice misfit of 24.6% ( $a_{\text{Si}} = 5.43 \text{ \AA}$ ;  $a_{\text{TiN}} = 4.24 \text{ \AA}$  [38]). The interface is  $\text{TiN}\{001\} / \text{Si}\{001\}$ . The domain matching epitaxy (DME) [27-29]

between single-crystal TiN and Si substrate has been illustrated elsewhere [28]. Figure 7.2 (c) shows the [110] zone-axis-pattern of MgO/TiN interface. The overlapping of diffraction points along all three directions (due to their close lattice constants ( $a_{\text{MgO}} = 4.216 \text{ \AA}$ )) indicates clearly a cube-on-cube relationship between MgO and TiN. The interface is  $\text{TiN}\{001\}/\text{MgO}\{001\}$ . These diffraction patterns demonstrate the epitaxial growth of  $\text{MgO}(100)\parallel\text{TiN}(100)\parallel\text{Si}(100)$ .

To investigate the atomic structure between Cu and  $\text{MgO}(100)$  interface, we collected HRTEM images, as shown in Figure 7.2 (d). First, an epitaxial layer of bcc(t) Cu grows pseudomorphically on  $\text{MgO}(100)$ , then after it reaches the critical thickness, the Gibbs free energy exceeds the strain free energy and the unstable bcc(t) Cu phase transforms to the stable fcc structure. The atomic structure at the interface region is enlarged in Figure 7.2 (e). The viewing direction is  $\text{MgO}[110]/\text{bcc}(t)\text{Cu}[100]$ .

The bcc(t) Cu is  $7\pm 1$  monolayers thick and the bcc(t)  $\text{Cu}\{011\}$  planes connect with  $\text{MgO}\{111\}$  planes across the interface. The matching planes are  $\text{MgO}\{200\}/\text{bcc}(t)\text{Cu}\{110\}$ , in accord with the matching relationship between bcc Ni and MgO [39]. For comparison, the  $\text{Cu}/\text{MgO}(111)/\text{TiN}(111)/\text{Si}(111)$  hetero-structure was also investigated with TEM. Figure 7.3 (a) shows the whole stack, in which MgO and TiN layers are measured to be  $\sim 150\text{nm}$  thick, and the Cu layer is thinner than 50 nm. SADP of Si/TiN and MgO/TiN interfaces shown in Figure 7.3 (b) and (c) demonstrate the epitaxial growth of  $\text{MgO}(111)\parallel\text{TiN}(111)\parallel\text{Si}(111)$ .

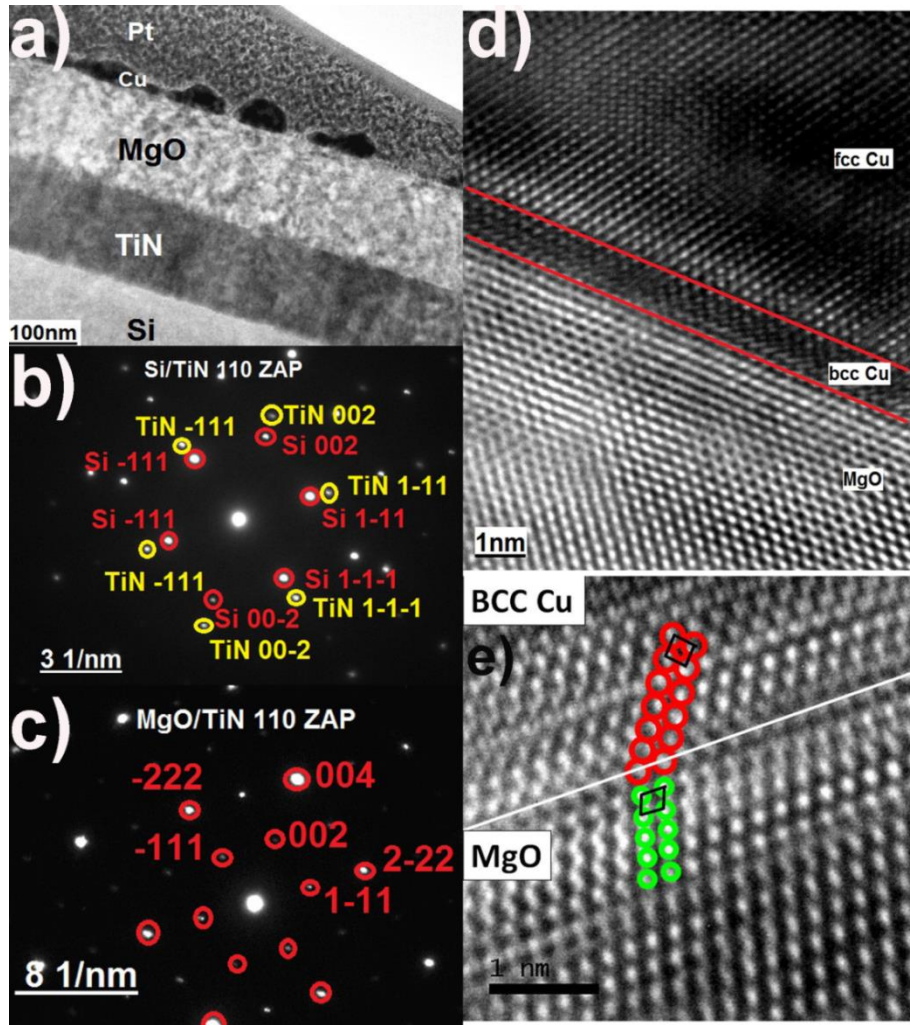


Figure 7.2 (a) Typical TEM bright-field cross-section image showing the whole stack Cu/MgO(100)/TiN(100)/Si(100). Pt layer was deposited for protection during the FIB sample preparation process. (b) [110] zone-axis-pattern (ZAP) of Si(100)/TiN(100) interface. (c) [110] ZAP of MgO(100)/TiN(100) interface. (d) A typical HRTEM image showing the Cu/MgO(100) interface. (e) A typical HRTEM image showing the atomic structure of bcc Cu at the Cu/MgO(100) interface region.

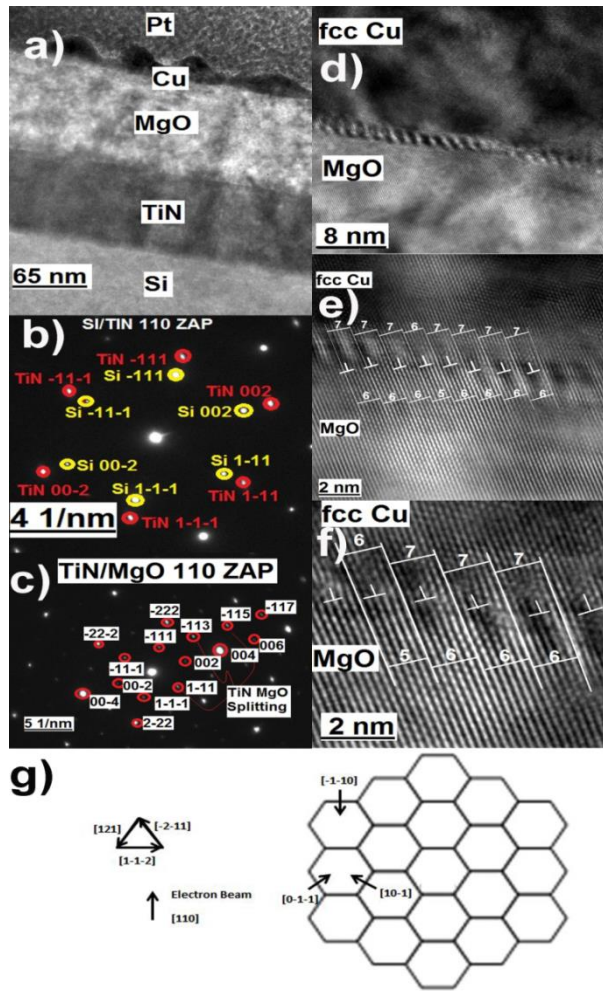


Figure 7.3 (a) Typical TEM bright-field cross-section image showing the whole stack Cu/MgO(111)/TiN(111)/Si(111). Pt layer was deposited for protection during the FIB sample preparation process. (b) [110] zone-axis-pattern (ZAP) of Si(111)/TiN(111) interface. (c) [110] ZAP of MgO(111)/TiN(111) interface. (d) - (f) HRTEM images of fcc Cu/ MgO (111) interface at different magnifications, viewed along [110] direction. (g) Schematic illustration of the hexagonal dislocation network on (111) planes between two close-packed lattices (fcc Cu/MgO) with a cube-on-cube relationship.

Figure 7.3 (d), (e) and (f) are HRTEM images showing the fcc Cu/MgO(111) interface at different magnifications and all of them are viewed along the [110] direction. Unlike the situation for the Cu/MgO(100) interface, the majority of the Cu phase remains fcc-structured on the MgO/TiN(111) template.

From Figure 7.3 (e) and (f), it can be seen that the fcc Cu/MgO(111) interface is atomically flat and sharp, without any secondary phase over a large area. Periodic contrast is visible along the interface due to the existence of misfit dislocations with a certain separation, indicating that the fcc Cu/MgO(111) interface is semi-coherent. The fcc Cu{002} planes connect with MgO{002} planes across the interface between the interfacial dislocations, and bend only within the localized width of the misfit dislocations. Since Cu has a large lattice misfit of 14.2% with respect to MgO, their matching should be explained by the DME [27-29] paradigm instead of the traditional LME, in which the misfit between the matching materials is typically less than 7-8% [29]. Two domains, in which 7 planes of fcc Cu{002} match with 6 planes of MgO{002} and 6 planes of fcc Cu{002} match with 5 planes of MgO{002} respectively, will alternate with a certain frequency. The domain matching mechanisms are illustrated in Figure 7.3 (e) and (f).

The highly-magnified HRTEM image shown in Figure 7.3 (f) demonstrates a periodic contrast variation along the [-112] direction. The misfit dislocations lying on the interfacial plane are clearly seen with an average separation of  $1.53 \pm 0.10$  nm. The

Burgers vector of the interfacial dislocations can be  $\frac{1}{2}\langle 10\bar{1} \rangle$ , which is a perfect lattice vector of both MgO and Cu. According to Bollmann's O-lattice theory [40], a hexagonal dislocation network, which is illustrated in Figure 7.3 (g), will exist on (111) planes between two close-packed lattices with a cube-on-cube relationship. The misfit dislocations are lying along  $\langle 112 \rangle$  directions, with Burgers vectors of  $\frac{1}{2}\langle 110 \rangle$ , such that all of them are edge dislocations, which are the most effective dislocations accommodating the lattice mismatch [40, 41]. The spacing between the dislocation lines can be calculated according to  $d = a_{\text{MgO}} a_{\text{Cu}} / 1.414 (a_{\text{MgO}} - a_{\text{Cu}})$  [41]. Taking the projection effect into consideration, the dislocation spacing viewed along [110] direction should be 1.56 nm for the Cu/MgO(111) interface, which matches with our observations.

Although the majority of the Cu phase growing on the MgO(111) template remains fcc-structured, 3-D island shaped bcc Cu grows on MgO(111) occasionally as well. Figure 7.4 (a) is a typical HRTEM image in which bcc(t) and fcc Cu coexist on MgO(111). The Cu/MgO(111) interface is drawn as a black line as a guide to the eyes. As easily seen from Figure 7.4 (a), the majority of the Cu phase remains fcc-structured and the MgO{002} planes match with Cu{002} planes as illustrated previously. However, within the red-circle region, bcc(t) Cu forms directly on MgO(111). After several monolayers of epitaxial growth, the unstable bcc-structured Cu turns back to its equilibrium structure again. The bcc(t) to fcc phase transformation of Cu can be understood as the competition between the strain energy and the Gibbs free energy associated with this

phase transformation. When the bcc(t) phase grows beyond the critical thickness, the strained layer will relax to its bulk structure by introduction of misfit dislocations. The region in which bcc(t) Cu lattice appears is enlarged as shown in Figure 7.4 (b). The critical thickness can be determined from the following equation [27, 42, 43]:

$$\frac{2\mu(1 + \nu)\epsilon_r^2(t_c)}{(1 - \nu)} \leq \Delta G_V$$

Where  $\epsilon_r$  is the residual strain which has a thickness dependence,  $\mu$  is the shear modulus,  $\nu$  is the Poisson's ratio and  $\Delta G_V$  is the Gibbs free energy difference between fcc and bcc(t) Cu. This model takes into account the strain distribution in the new phase, which is not accounted by the earlier thermodynamic model [44]. The neglect of the effect of coherency strains will result in a large error, due to the large strain within the bcc(t) Cu/ MgO hetero-structure.

To better understand the orientation relationship between each phase, the selected area diffraction patterns of fcc Cu, MgO and bcc(t) Cu are demonstrated in Figures 7.4 (c), (d) and (e) respectively. Figures 7.4 (c) and (d) are [110] zone axis patterns for fcc Cu and MgO, respectively, from which it is clearly seen that the interface plane is fcc Cu $\{-111\}$ /MgO $\{-111\}$ . The  $\{002\}$  lattice planes of Cu match with those of MgO across the  $\{-111\}$  interface plane. Figure 7.4 (e) is the [111] zone axis pattern for bcc(t) Cu, which indicates that the interface plane is actually  $\{-101\}$  lattice plane for bcc(t) Cu. The  $\{002\}$  lattice planes of MgO now connect  $\{01-1\}$  lattice planes of bcc(t) Cu

across the interface plane. Using MgO ( $a=4.216 \text{ \AA}$ ) as the internal calibration standard, the lattice parameter of bcc(t) Cu is calculated to be  $2.886 \pm 0.010 \text{ \AA}$ , which fits well to the reported range of the lattice constant of bulk bcc(t) Cu (from 2.87 to 2.96  $\text{\AA}$  [45]). Compared with small lattice misfit systems ( $\sim 0.3\%$ ) in which bcc(t) Cu grows pseudomorphically on substrates such as Ag [20], planar spacing matching instead of lattice matching holds true for bcc(t) Cu/MgO. The following equation satisfies the domain matching among these three phases:

$$\frac{a_{MgO}}{2} = \frac{a_{FCC\ Cu}}{\sqrt{3}} = \frac{a_{BCC\ Cu}}{\sqrt{2}}$$

It should be pointed out that although this relationship is derived from flat interfaces presented in this paper, the above equation is applicable to wavy (curved) interfaces as well. Wei et al. [46] reported that the wavy interface gave rise to a variety of orientation relationships and the interface structure may be more complex and involve disconnections. At the top/bottom layers, K-S [34] and N-W orientations (common interface plane:  $\{111\}_{fcc}||\{011\}_{bcc}$  [35]) dominated between two adjacent (V/Ag) layers, while on the slopes of the wavy interface, the Bain orientation relationship (common interface plane:  $\{100\}_{fcc}||\{100\}_{bcc}$  [47]) was preferred.

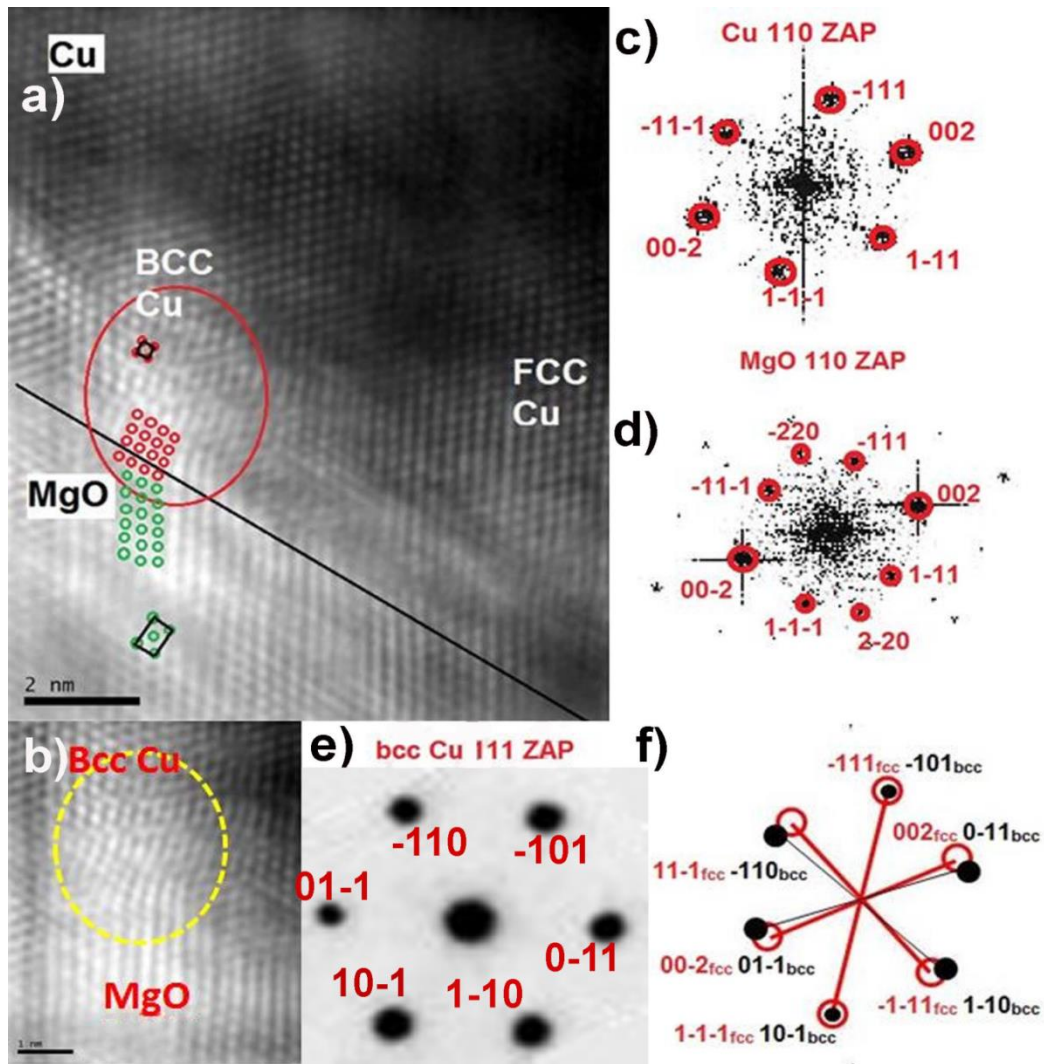


Figure 7.4 (a) A typical HRTEM image in which island-shaped bcc(t) Cu and epitaxial fcc Cu coexist on MgO(111). (b) Enlarged HRTEM image showing the island region where bcc Cu lattice appears. (c) [110] ZAP of fcc Cu. (d) [110] ZAP of MgO. (e) [111] ZAP of bcc Cu. (f) Simulated [110] ZAP of fcc Cu and [111] ZAP of bcc Cu.

However, although the orientation relationships between two adjacent layers may change from one position to another for wavy interfaces, the matching planes for bcc(t) Cu, fcc Cu and MgO phases will not change, which are bcc(t) Cu{110}||MgO{200}||fcc Cu{200} planes. The DME mechanism determines that this equation holds true for wavy interfaces as well. This is important because curved surfaces play a critical role in dislocation nucleation as a result of interfacial steps and strain relaxation [48, 49]. The simulated diffraction patterns for fcc Cu and bcc(t) Cu are shown together in Figure 7.4 (f), which corresponds well to the zone axis patterns we obtained for the two phases.

#### **7.4 Conclusions**

Bcc(t) and fcc Cu were fabricated onto MgO(100)/TiN(100)/Si(100) and MgO(111)/TiN(111)/Si(111) for integration on Silicon substrates. At high temperature, only fcc Cu grows on both MgO(100) and MgO(111) templates. At room temperature, an epitaxial layer of bcc(t) Cu will first grow on MgO(100) pseudomorphically, and then transform back to fcc Cu after exceeding the critical thickness. In contrast, the majority of Cu on MgO(111) would remain fcc-structured, and island-shaped bcc(t) Cu will occasionally grow on MgO(111). For both MgO/TiN(100) and MgO/TiN(111) templates, the growth of these hetero-structures involves epitaxy across the misfit scale by

matching MgO{200} with bcc(t) Cu{110} planes. The morphology of the Cu layer can be controlled by the the orientation of MgO templates and the deposition temperatures.

## References

- [1] S.P. Murarka, S.W. Hymes, *Copper metallization for ULSI and beyond*. Critical Reviews in Solid State and Materials Sciences 1995;20(2):87-124.
- [2] H. Itow, Y. Nakasaki, G. Minamihaba, K. Suguro, H. Okano, *Self-aligned passivation on copper interconnection durability against oxidizing ambient annealing*. Applied Physics Letters 1993;63(7):934-936.
- [3] J. Tao, N.W. Cheung, C.M. Hu, *Electromigration characteristics of copper interconnects*. IEEE Electron Device Letters 1993;14(5):249-251.
- [4] P.J. Lin, M.C. Chen, *Copper chemical vapor deposition films deposited from Cu(1,1,1,5,5,5-hexafluoroacetylacetonate) vinyltrimethylsilane*. Japanese Journal of Applied Physics Part 1-Regular Papers Short Notes & Review Papers 1999;38(8):4863-4867.
- [5] Y.J. Park, V.K. Andleigh, C.V. Thompson, *Simulations of stress evolution and the current density scaling of electromigration-induced failure times in pure and alloyed interconnects*. Journal of Applied Physics 1999;85(7):3546-3555.
- [6] C. Whitman, M.M. Moslehi, A. Paranjpe, L. Velo, T. Omstead, *Ultralarge scale integrated metallization and interconnects*. Journal of Vacuum Science & Technology a-Vacuum Surfaces and Films 1999;17(4):1893-1897.

- [7] A. Chugh, A. Tiwari, A. Kvit, J. Narayan, *A novel technique for making self-encapsulated and self-aligned copper films*. Materials Science and Engineering B-Solid State Materials for Advanced Technology 2003;103(1):45-48.
- [8] R.C. Liu, C.S. Pai, E. Martinez, *Interconnect technology trend for microelectronics*. Solid-State Electronics 1999;43(6):1003-1009.
- [9] W.C. Roh, D.J. Jung, *Diffusion barrier characteristics of Hf(C,N) thin films deposited by plasma enhanced metal organic chemical vapor deposition for Cu metallization*. Japanese Journal of Applied Physics Part 2-Letters 1998;37(4A):L406-L408.
- [10] W. Lee, H. Cho, B. Cho, H.J. Yang, J. Kim, Y.S. Kim, W.G. Jung, H. Kwon, J. Lee, P.J. Reucroft, C. Lee, E. Lee, J. Lee, *Thermal stability enhancement of Cu interconnects by employing a self-aligned MgO layer obtained from a Cu(Mg) alloy film*. Japanese Journal of Applied Physics Part 1-Regular Papers Brief Communications & Review Papers 2001;40(4A):2408-2412.
- [11] W.H. Lee, H.L. Cho, B.S. Cho, J.Y. Kim, W.J. Nam, Y.S. Kim, W.G. Jung, H. Kwon, J.H. Lee, J.G. Lee, P.J. Reucroft, C.M. Lee, E.G. Lee, *Diffusion barrier and electrical characteristics of a self-aligned MgO layer obtained from a Cu(Mg) alloy film*. Applied Physics Letters 2000;77(14):2192-2194.
- [12] K. Burger, W. Mader, M. Ruhle, *Structure, chemistry and diffusion bonding of metal ceramic interfaces*. Ultramicroscopy 1987;22(1-4):1-13.

- [13] F. Ernst, P. Pirouz, A.H. Heuer, *HRTEM study of a Cu/Al<sub>2</sub>O<sub>3</sub> Interface*. Philosophical Magazine a-Physics of Condensed Matter Structure Defects and Mechanical Properties 1991;63(2):259-277.
- [14] Y.F. Zhukovskii, E.A. Kotomin, D. Fuks, S. Dorfman, A.M. Stoneham, O. Sychev, G. Borstel, *First principles simulations of 2D Cu superlattices on the MgO(001) surface*. Applied Surface Science 2004;226(1-3):298-305.
- [15] T. Mewes, M. Rickart, A. Mougín, S.O. Demokritov, J. Fassbender, B. Hillebrands, M. Scheib, *Comparative study of the epitaxial growth of Cu on MgO(001) and on hydrogen terminated Si(001)*. Surface Science 2001;481(1-3):87-96.
- [16] G. Eilers, K. Mukasa, *Surface morphology of thin Cu films grown on magnesium oxide (100)*. Japanese Journal of Applied Physics Part 1-Regular Papers Short Notes & Review Papers 2000;39(6B):3780-3783.
- [17] M.P. Delplancke, P. Delcambe, L. Binst, M. Jardinieroffergeld, F. Bouillon, *Structure and purity of epitaxial films of copper and rhodium deposited onto MgO single-crystal substrates by glow-discharge sputtering*. Thin Solid Films 1986;143(1):43-51.
- [18] F. Reniers, M.P. Delplancke, A. Asskali, V. Rooryck, O. VanSinay, *Glow discharge sputtering deposition of thin films of Ag, Cr, Cu, Ni, Pd, Rh and their binary alloys onto NaCl and MgO experimental parameters and epitaxy*. Applied Surface Science 1996;9235-42.

- [19] H. Kung, Y.C. Lu, A.J. Griffin, M. Nastasi, T.E. Mitchell, J.D. Embury, *Observation of body centered cubic Cu in Cu/Nb nanolayered composites*. Applied Physics Letters 1997;71(15):2103-2105.
- [20] H. Li, D. Tian, J. Quinn, Y.S. Li, F. Jona, P.M. Marcus, *Low-energy electron diffraction and photoemission study of epitaxial films of Cu on Ag{001}*. Physical Review B 1991;43(8):6342-6346.
- [21] E. Hahn, E. Kampshoff, N. Wälchli, K. Kern, *Strain Driven fcc-bct Phase Transition of Pseudomorphic Cu Films on Pd(100)*. Physical Review Letters 1995;74(10):1803-1806.
- [22] H. Li, S.C. Wu, D. Tian, J. Quinn, Y.S. Li, F. Jona, P.M. Marcus, *Epitaxial growth of body centered tetragonal copper*. Physical Review B 1989;40(8):5841-5844.
- [23] A. Misra, M.J. Demkowicz, X. Zhang, R.G. Hoagland, *The radiation damage tolerance of ultra-high strength nanolayered composites*. JOM 2007;59(9):62-65.
- [24] M.J. Demkowicz, R.G. Hoagland, J.P. Hirth, *Interface Structure and Radiation Damage Resistance in Cu-Nb Multilayer Nanocomposites*. Physical Review Letters 2008;100(13):136102.
- [25] J. Wang, R.G. Hoagland, A. Misra, *Room-temperature dislocation climb in metallic interfaces*. Applied Physics Letters 2009;94(13).
- [26] A. Perumal, Y.K. Takahashi, T.O. Seki, K. Hono, *Particulate structure of L1(0) ordered ultrathin FePt films for perpendicular recording*. Applied Physics Letters 2008;92(13).
- [27] J. Narayan, *Recent progress in thin film epitaxy across the misfit scale (2011 Acta Gold Medal Paper)*. Acta Materialia 2013;61(8):2703-2724.

- [28] J. Narayan, P. Tiwari, X. Chen, J. Singh, R. Chowdhury, T. Zheleva, *Epitaxial growth of thin films on (100) Si substrates by laser physical vapor deposition*. Applied Physics Letters 1992;61(11):1290-1292.
- [29] J. Narayan, B.C. Larson, *Domain epitaxy: A unified paradigm for thin film growth*. Journal of Applied Physics 2003;93(1):278-285.
- [30] Q.M. Wei, X.Y. Liu, A. Misra, *Observation of continuous and reversible bcc-fcc phase transformation in Ag/V multilayers*. Applied Physics Letters 2011;98(11).
- [31] J. Wang, A. Misra, *An overview of interface-dominated deformation mechanisms in metallic multilayers*. Current Opinion in Solid State & Materials Science 2011;15(1):20-28.
- [32] R.F. Zhang, J. Wang, I.J. Beyerlein, T.C. Germann, *Dislocation nucleation mechanisms from fcc/bcc incoherent interfaces*. Scripta Materialia 2011;65(11):1022-1025.
- [33] A. Misra, M. Verdier, Y.C. Lu, H. Kung, T.E. Mitchell, N. Nastasi, J.D. Embury, *Structure and mechanical properties of Cu-X (X = Nb,Cr,Ni) nanolayered composites*. Scripta Materialia 1998;39(4-5):555-560.
- [34] G. Kurdjumow, G. Sachs, *Über den Mechanismus der Stahlhärtung*. Z. Physik 1930;64(5-6):325-343.
- [35] B. Wang, H.M. Urbassek, *Phase transitions in an Fe system containing a bcc/fcc phase boundary: An atomistic study*. Physical Review B 2013;87(10):104108.
- [36] F. Wu, Y. Zhu, J. Narayan, *Grain size effect on twin density in as-deposited nanocrystalline Cu film*. Philosophical Magazine 2013;accepted.

- [37] F. Wu, H. Wen, E. Lavernia, J. Narayan, Y. Zhu, *Twin intersection mechanisms in nanocrystalline fcc metals*. Materials Science and Engineering A 2013;accepted.
- [38] A.K. Sharma, J. Narayan, C. Jin, A. Kvit, S. Chattopadhyay, C. Lee, *Integration of Pb(Zr<sub>0.52</sub>Ti<sub>0.48</sub>)O<sub>3</sub> epilayers with Si by domain epitaxy*. Applied Physics Letters 2000;76(11):1458-1460.
- [39] J. Narayan, Y. Chen, R.M. Moon, R.W. Carpenter, *Characterization of metal precipitates in Magnesium oxide.1*. Philosophical Magazine a-Physics of Condensed Matter Structure Defects and Mechanical Properties 1984;49(2):287-300.
- [40] F.R. Chen, S.K. Chiou, L. Chang, C.S. Hong, *High-resolution electron microscopy of Cu/MgO and Pd/MgO interfaces*. Ultramicroscopy 1994;54(2-4):179-191.
- [41] P. Lu, F. Cosandey, *Electron-microscopy studies of metal MgO interfaces*. Ultramicroscopy 1992;40(3):271-280.
- [42] T. Zheleva, K. Jagannadham, J. Narayan, *Epitaxial growth in large lattice mismatch systems*. Journal of Applied Physics 1994;75(2):860-871.
- [43] S. Sharan, J. Narayan, *Strain-relief Mechanisms and Nature of Misfit Dislocations in GaAs/Si Heterostructures*. Materials Science and Engineering: A 1989;11357-63.
- [44] S.A. Dregia, R. Banerjee, H.L. Fraser, *Polymorphic phase stability in thin multilayers*. Scripta Materialia 1998;39(2):217-223.
- [45] C. Schmidt, F. Ernst, M.W. Finnis, V. Vitek, *Prediction and Observation of the bcc Structure in Pure Copper at a  $\Sigma 3$  Grain Boundary*. Physical Review Letters 1995;75(11):2160-2163.

- [46] Q. Wei, A. Misra, *Transmission electron microscopy study of the microstructure and crystallographic orientation relationships in V/Ag multilayers*. Acta Materialia 2010;58(14):4871-4882.
- [47] B.M. Clemens, H. Kung, S.A. Barnett, *Structure and strength of multilayers*. MRS Bulletin 1999;24(2):20-26.
- [48] M. Ichimura, J. Narayan, *Atomic study of dislocation nucleation in Ge/(001)Si heterostructures*. Philosophical Magazine a-Physics of Condensed Matter Structure Defects and Mechanical Properties 1995;72(2):281-295.
- [49] M. Ichimura, J. Narayan, *Negative surface-energy change associated with step formation caused by misfit dislocation nucleation in semiconductor heterostructures*. Philosophical Magazine a-Physics of Condensed Matter Structure Defects and Mechanical Properties 1995;72(2):297-304.

## **Chapter 8**

# **Fabrication and investigation of the interface between Ni and MgO on Si**

Epitaxial Ni thin films were integrated with tunneling barrier MgO on Si(100) substrates. During pulsed laser deposition, early island-like structure transformed into uniform thin film with increasing number of laser pulses. This led to transitions in exchange bias from positive to negative and back to positive, which is ascribed to morphology associated residual strain. The Ni island structure has a coercive field as high as 3 times that of the continuous film. The work in this chapter holds a tremendous promise in the realization of magnetic devices integrated with a Si platform.

### **8.1 Introduction**

Metal-oxide [1, 2] interfaces are of growing interest from both fundamental and technological viewpoints. Ni/MgO is one of the most attractive metal-ceramic systems due to its high temperature stability, the excellent tunneling barrier characteristics of MgO, and the ferromagnetic properties of Ni [3]. In addition, Ni films can work as an

effective buffer/seed layer for growing other materials like carbon nanotubes [4]. Various studies have been done on the Ni/MgO system. For instance, Raatz and Woltersdorf [5] reported the effect of Ni film thickness on its film orientation. McCaffrey [6], Svedberg [7], Reniers [8] and Qiu [9] *et al* studied the effect of growth temperature on the orientation of epitaxial Ni films on MgO(001). Lukaszew [10] *et al* studied the magneto-optic Kerr effect (the magnetization-induced change in polarization state and/or intensity of the light reflected from the surface of a magnetized medium) of Ni thin films on MgO single crystal substrates. Furthermore, there have been several reports on Ni nanowires [11] and thin films [12] that were used to engineer the magnetic properties for data storage applications. Unfortunately, all of the above investigations, particularly, the magnetic properties of Ni thin films hitherto have been focused on films grown on MgO substrates using MBE and sputtering techniques, while we study the effect of film thickness and morphology on the magnetic properties of epitaxial Ni thin films, growing on MgO buffer layers prepared on Si(100) substrates, which is highly relevant to magnetic tunnel junction devices.

Here I report distinctive magnetic properties such as transition of exchange bias ( $H_{EB}$ ) (from positive to negative to positive) and coercive field ( $H_C$ ) (technologically relevant magnetic device parameters) as a function Ni thin film morphology. Furthermore, this work demonstrates the integration of epitaxial Ni thin films on a conventional Si platform. By successfully fabricating an epitaxial MgO template on Si using TiN as the buffer layer, we were successful in fabricating epitaxial Ni/MgO stacks

for integration on the technologically important silicon substrate, which is inexpensive, readily available, and widely used in present-day microelectronic devices. More importantly, the buffer layer approach demonstrated here holds tremendous promise because several other smart structures such as bcc(t)Cu/MgO [13], ferroelectric [14], permalloy [15], ferromagnetic oxide heterostructures and topological insulators [16] have already been integrated with Si (100), and found to have useful physical properties for application in present-day microelectronic or nanoelectronic devices. The atomic structure at the interface between Ni and MgO is investigated.

## 8.2 Experimental Approach

The multilayer Ni/MgO/TiN/Si(100) heterostructures were produced using pulsed laser deposition (PLD) in a multi-target stainless-steel chamber. Detailed experimental parameters related to the PLD process (e.g. chamber configuration, laser energy, wavelength, pulse duration, etc.) have been described elsewhere [17, 18]. The base vacuum pressure in the deposition chamber was  $1 \times 10^{-6}$  torr. Though the lattice misfit between TiN ( $a = 4.21 \text{ \AA}$ ) layer and Si ( $a = 5.43 \text{ \AA}$ ) substrate is large ( $\sim 22.5\%$ ), a good epitaxial growth of TiN occurs via domain matching epitaxy (DME) [19], in which alternating 3/4 domain matching and 4/5 domain matching mechanisms coexist. The epitaxial growth of MgO ( $a = 4.22 \text{ \AA}$ ) was then easily accomplished, due to the excellent lattice match with TiN. The combination of MgO and TiN layers provides a superior

diffusion barrier and perfect base for the subsequent growth of an epitaxial thin layer of Ni and overall integration with Si (100). Optimized deposition conditions for the growth of MgO and TiN layers have been identified previously [14, 20] for this geometry. Three Ni/MgO/TiN/Si(100) heterostructures with different Ni thicknesses were fabricated to systematically investigate the effect of thicknesses of Ni films on their morphology, microstructure and magnetic properties. The thicknesses of Ni layers were controlled by increasing the number of deposition pulses of Ni, which were 1500, 3500 and 7000, respectively for the three stacks. The Ni target was 4N purity Ni sheet obtained from ESPI Metals Inc. Ni deposition was carried out under vacuum at a substrate temperature of 550 °C. The energy density and pulse frequency were 3 J/cm<sup>2</sup> and 10 Hz, respectively, based on our previous experiences with ablation of metal targets [21, 22] by pulsed laser. Once completed, the samples were cooled slowly to ambient temperature under vacuum.

A Rigaku SmartLab X-ray diffractometer with a Bragg Brentano Goniometer (copper X-ray anode, K $\alpha$  radiation,  $\lambda = 1.54 \text{ \AA}$ ) was employed for  $\theta$ - $2\theta$  scans to determine the structure, crystallinity and out-of-plane orientation of the films. The microstructures of these films were characterized using a JEOL-2000FX transmission electron microscope (TEM). A detailed atomic-resolution study at Ni/MgO interfaces was performed, using a JEOL-2010F high resolution TEM (HRTEM), equipped with a Gatan image filter tuning attachment, which has a point-to-point resolution of 1.8 Å. The

aberration corrected FEI Titan 80-300 probe with a point-to-point resolution of 0.7 Å was used for scanning transmission electron microscope (STEM-Z contrast) observation. Instead of traditional sample preparation methods [17], focused ion beam (FIB) technique was adopted to prepare TEM samples, using a FEI Quanta 3D FEG, which is a dual-beam instrument that combines a traditional field emission column with a FIB column.

Magnetic-field dependent magnetization measurements were carried out using a Quantum design MPMS SQUID VSM dc magnetometer with the sensitivity  $\leq 10^{-8}$  emu at 0 Oe. TiN and MgO buffer layers were confirmed to be non-magnetic [20], such that only the Ni layer contributes to the magnetic properties of the Ni/MgO/TiN/Si(100) heterostructures, reported in this work. For magnetization measurements, a 4 mm  $\times$  4 mm section was cut from original samples. Great care was taken in handling the specimens to avoid external contamination throughout the experiment.

### **8.3 Results and Discussion**

Figure 8.1 presents the XRD  $\theta$ - $2\theta$  patterns of the three multi-layer Ni/MgO/TiN/Si(100) heterostructures. The number of pulses for Ni deposition for samples 1, 2 and 3 are 1500, 3500 and 7000 pulses, respectively. For convenience, the three samples are labeled as Ni1, Ni2 and Ni3, respectively. All of the peaks in this

pattern are identified and assigned to Ni, MgO, TiN and Si. No indication of other phases, such as interfacial reaction products, can be observed in the XRD patterns.

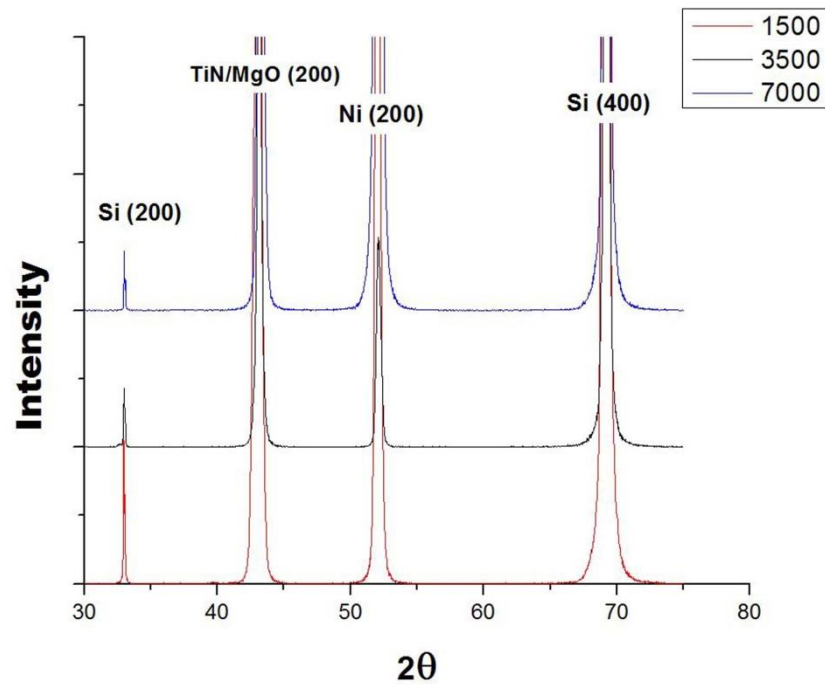


Figure 8.1: The  $\theta$ - $2\theta$  XRD patterns of the three multilayer Ni/MgO/TiN/Si(100) heterostructures, for which the deposition pulses of Ni are 1500, 3500 and 7000 pulses, respectively.

It is evident from this pattern that all the layers in three samples demonstrate the preferential orientation  $\langle 00l \rangle$ , normal to the Si {001} substrate, suggesting the epitaxial

growth of the multilayered structures. Given the wavelength of  $K_{\alpha}$  radiation of the copper anode to be 1.54 Å, the out-of-plane (OOP) lattice parameters of samples 1, 2 and 3 are 3.51 Å, 3.50 Å, and 3.51 Å, respectively, which are somewhat smaller than that (3.52 Å) of bulk Ni. This indicates that the Ni1, Ni2 and Ni3 are under OOP compressive stresses and in-plane tensile stresses.

The residual strain within Ni films can be calculated based on the Ni {002} peak positions in Figure 1. Taking Ni1 as an example, the Ni {002} peak is measured to be located at the position of  $2\theta = 52.0197^{\circ}$ . According to the Bragg Law ( $2d\sin\theta = \lambda$ ), the planar spacing of Ni {002} planes parallel to the surface is calculated to be  $d// = 1.756$  Å. Consequently, the lattice constant of Ni along the out-of-plane direction is  $a_{zz} = 2d// = 3.513$  Å. Since the standard lattice constant of bulk Ni is 3.520 Å, the out-of-plane strain  $\epsilon_{zz}$  of the Ni film can thus be calculated to be -0.1976%. According to the generalized relationship between stress and strain tensors in cubic crystals [23], the stresses and strains along different directions are related to each other [24]. Combining these relationships with the equation among the out-of-plane strain  $\epsilon_{zz}$ , in-plane strain  $\epsilon_{xx}$ ,  $\epsilon_{yy}$ , and Poisson's ratio  $\nu$ , i.e. ( $\epsilon_{zz}/(\epsilon_{xx} + \epsilon_{yy}) = -\nu/(1 - \nu)$ ) [24], we can calculate the in-plane strain of Ni1 to be 0.2199% (note that the Poisson's ratio  $\nu$  is taken to be 0.31 for Ni here). This residual strain is in agreement with other reported unrelieved strain ( $\sim 0.2\%$ ) in as-deposited epitaxial Ni films [25]. This routine procedure to calculate in-plane strain within thin films from XRD scan patterns has been published elsewhere [22]

and can also be found in the text [26]. Note that the comparison among the residual strains within three Ni films can provide internal strain information of specific films, since the strains were calculated using the same procedure. The out-of-plane lattice constants, strains and in-plane strains of Ni film 1-3 were calculated and summarized in table 8.1. Since the islands are restrained from expanding only along the interface [27], the interface between the islands and the substrate becomes curved and results in a large non-uniform strain inside islands [27]. In comparison, the strain in the uniform film may be relieved by the nucleation of dislocations beyond the critical thickness [27].

Figure 8.2 (a) shows the typical cross-sectional bright field (BF) TEM image of Ni1. The Pt layer was deposited onto this stack for protection during the FIB sample preparation process. As it can be immediately noticed, the individual Ni islands grew on the MgO buffer layer, indicating a 3-D growth mode of Ni (adatom-adatom interactions are stronger than those of the adatom with the surface, leading to the formation of three-dimensional adatom clusters or islands). The thickness of Ni layer is  $\sim 80\text{nm}$ , and the average width of individual Ni islands is  $\sim 180\text{nm}$ . To study the microstructures of the buffer layers and the orientation relationships between them, selected area diffraction patterns (SADP) were obtained at each interface of Ni1.

Figure 8.2 (b) shows the  $[110]$  zone-axis SADP of Ni1, in which the diffraction patterns corresponding to Si, TiN, MgO and Ni are labeled. These patterns clearly demonstrate cube-on-cube relationships among the three layers and the Si substrate.

**Table 8.1:** The correlation between Out-of-plane lattice constants, in-plane and out of plane strain, coercive field, and exchange bias,

<b>Number of pulses for Ni</b>	<b>Out-of-plane lattice constants (Å)</b>	<b>Out-of-plane strain <math>\epsilon_{zz}</math> (%)</b>	<b>In-plane strain <math>\epsilon_{xx}</math> or <math>\epsilon_{yy}</math> (%)</b>	<b>Exchange bias <math>H_{EB}</math> (Oe)</b>	<b>Coercive field <math>H_c</math> (Oe)</b>
<b>1500(80 nm thick, island-like)</b>	3.513	-0.1976	0.2199	70 (positive)	241
<b>3500(200 nm thick, extended island-like)</b>	3.507	-0.3704	0.4123	40 (negative)	147
<b>7000(350 nm thick, continuous)</b>	3.515	-0.1266	0.1409	49 (positive)	86

The diffraction points corresponding to the same planes of TiN, MgO, Ni and Si split but appear along the same directions, due to the differences of lattice constants

among four phases. The interfaces are Ni(001)/ MgO(001)/ TiN(001)/ Si(001). The OOP orientations for these four phases are [002]. Figure 8.2 (c) demonstrates the typical cross-sectional BF TEM image of Ni2. Similar to Ni1, individual Ni islands exist on the MgO buffer layer, again indicating a 3-D growth mode of Ni. However, due to the increase of deposition pulses, the thickness of Ni islands increased to about 200 nm, and the average width of individual Ni islands increased to  $\sim 750$ nm. This observation indicates that while Ni islands grow thicker along the OOP orientation as the number of pulses increases, the Ni islands also grow wider along the in-plane orientation. The Ni islands are thus expected to connect with each other and form a continuous film, when reaching a critical deposition pulse number, as shown for Ni3 depicted in Fig. 8.2 (d). Unlike Ni1 and Ni2, the Ni3 grew out to form a uniform and continuous film, instead of individual islands. The thickness of this film reached  $\sim 350$ nm. Therefore according to the TEM observations of all three samples, the morphology of Ni phase on MgO buffer layer is dependent on the number of pulses. The SADP of Ni films in Ni2 and Ni3 are similar to the pattern shown in Fig. 8.2 (b). This indicates that although the morphology of Ni phase changes from islands to a continuous film, the epitaxial relationship between Ni and MgO buffer layer remains unchanged with increasing number of pulses.

The atomic structure between Ni and MgO(100) interface was investigated using STEM-Z contrast imaging, see Figure 8.3 (a). The viewing directions for both Ni and MgO phases are along  $\langle 110 \rangle$ . The Ni/MgO(100) interface is atomically flat and sharp,

without any secondary phase (such as NiO) over a large area. Periodic contrast is visible along the interface due to the existence of misfit dislocations with a fixed separation of 21.475Å, indicating that the Ni/MgO(100) interface is semi-coherent. The Ni {111} planes are connected with MgO{111} planes across the interface between the interfacial dislocations and bent only within the localized width of the misfit dislocations. Though MgO and Ni possess very different electric and magnetic properties, both of them belong to the same space group of Fm3m.

At 550°C (the growth temperature employed in this work),  $a_{\text{Ni}} = 3.5527\text{Å}$  and  $a_{\text{MgO}} = 4.2950\text{Å}$ , such that MgO has a larger lattice constant by a mismatch of ~17.28%. Such a large lattice misfit can only be accommodated by the DME [28] paradigm, the traditional lattice matching epitaxy (LME) is generally believed to have no validity as the two matching materials approaches ~7–8% [19]. In the current case, domains form as labeled in Figure 8.3 (b). In each domain, six planes of Ni{111} match with 5 planes of MgO{111}. The highly magnified HRTEM BF image shown in Figure 8.3 (b) demonstrates a periodic contrast variation across the interface region.

In Figure 8.4, we show the in-plane isothermal (4 K) magnetic hysteresis data collected on all three Ni heterostructures. In all the magnetization data presented here, the magnetic field is applied along <100> direction of the sample. The data were collected after each sample was zero field cooled (ZFC) from 400 K down to 4 K.

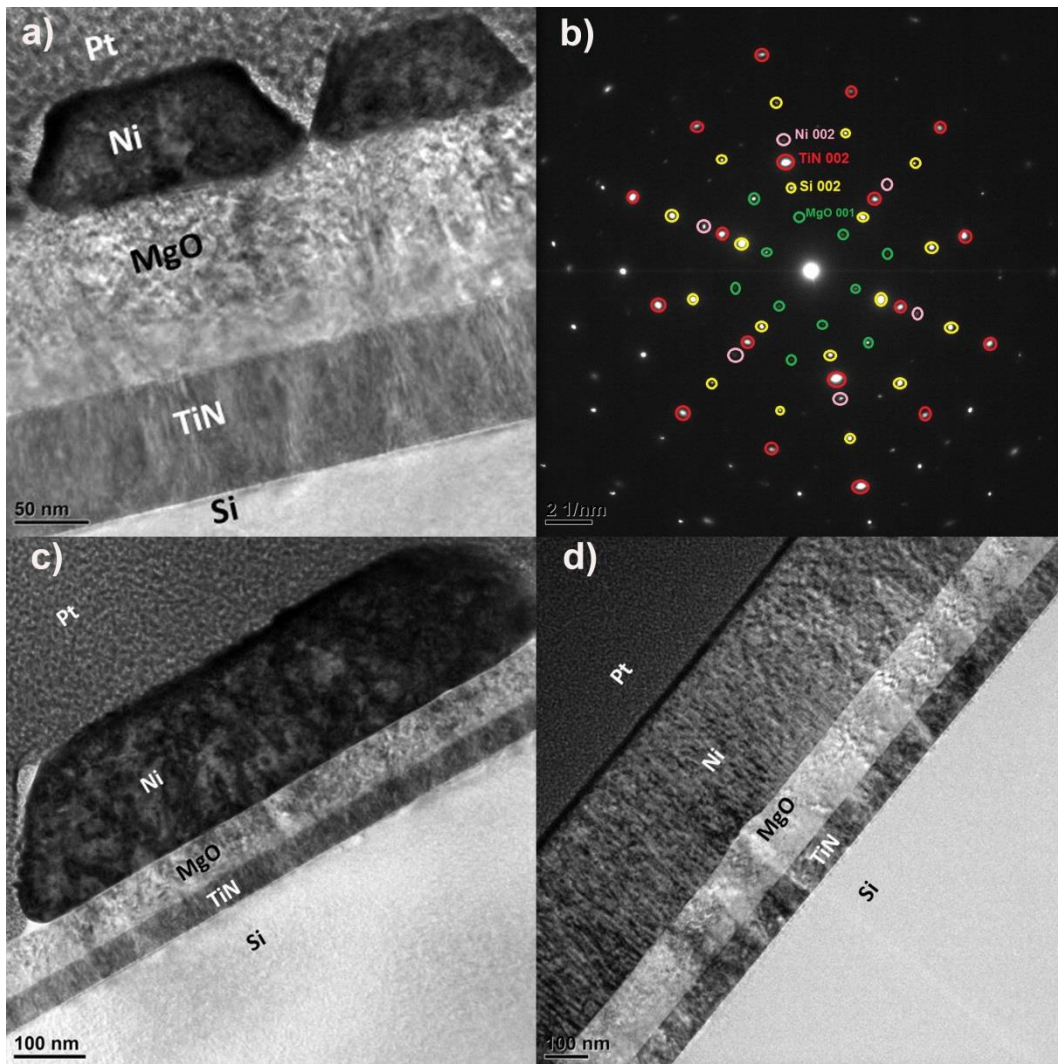


Figure 8.2: (a) The typical cross-sectional bright field (BF) TEM image of Ni1. (b) The [110] zone-axis SADP of Ni1, in which the diffraction patterns corresponding to Si, TiN, MgO and Ni are labeled. (c) The typical cross-sectional BF TEM image of Ni2. (d) The typical cross-sectional BF TEM image of Ni3.

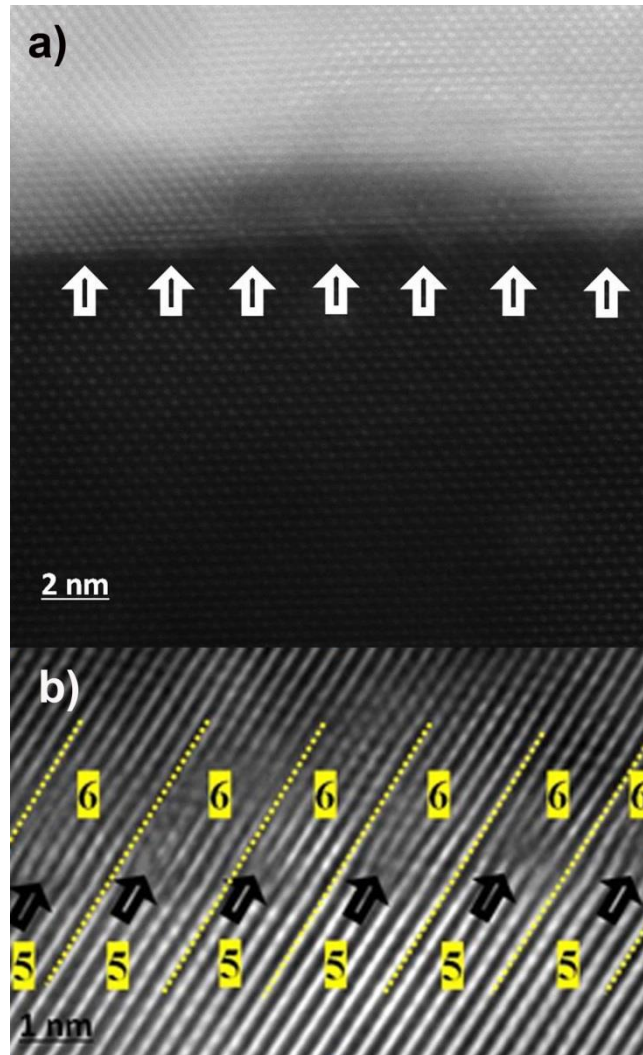


Figure 8.3: (a) STEM-Z contrast image demonstrating the Ni/ MgO (100) interface, viewed along  $\langle 110 \rangle$  direction for both Ni and MgO phases. (b) HRTEM image showing the Ni/ MgO (100) interface, in which DME mechanism is labeled in detail.

The hallmark magnetic parameters such as coercive field  $H_c$  (the applied field where the hysteresis loop crosses zero) and exchange bias  $H_{EB}$  inferred from Figure 8.4 are shown in Table 8.1. The exchange bias field is defined as  $H_{EB} = (|H_{right}| - |H_{left}|)/2$ , and coercive field as  $H_c = (|H_{right}| + |H_{left}|)/2$ , where  $H_{right}$  and  $H_{left}$  being the magnetic field values where the loop intersects the field axis on right and left, respectively. Several important features can be noted: (a) the magnetic characteristics and magnetization reversal processes are highly dependent on the Ni thin film morphology and thickness; (b) coercive field and exchange bias are found to be strong functions of Ni morphology and thickness; (c) most importantly, the 80nm-thick sample shows positive exchange bias (PEB) (shift of MH loop toward positive field axis), 200nm-thick sample shows negative exchange bias (NEB) (shift of MH loop toward negative field axis), and the 350nm-thick sample shows PEB. For more clarity, the zoomed version is depicted in the inset of Figure 8.4 (b). The Ni film prepared at highest number of pulses (Ni3) exhibits bulk-like soft ferromagnetic features associated with improved squareness and lower  $H_c$  (85 Oe), when compared to the other Ni films (Ni1 and Ni2), prepared with lower number of pulses. The later films show highly unsaturated MH loops with the  $H_c$  as high as 241 Oe, much higher than the values ( $\sim 160$  Oe) reported for electrodeposited Ni nano dots of similar diameter [29]. The highest  $H_c$  value reported here is comparable to earlier reported values ( $\sim 250$  Oe) for Al<sub>2</sub>O<sub>3</sub> capped Ni nanoparticles of 12nm size [30].

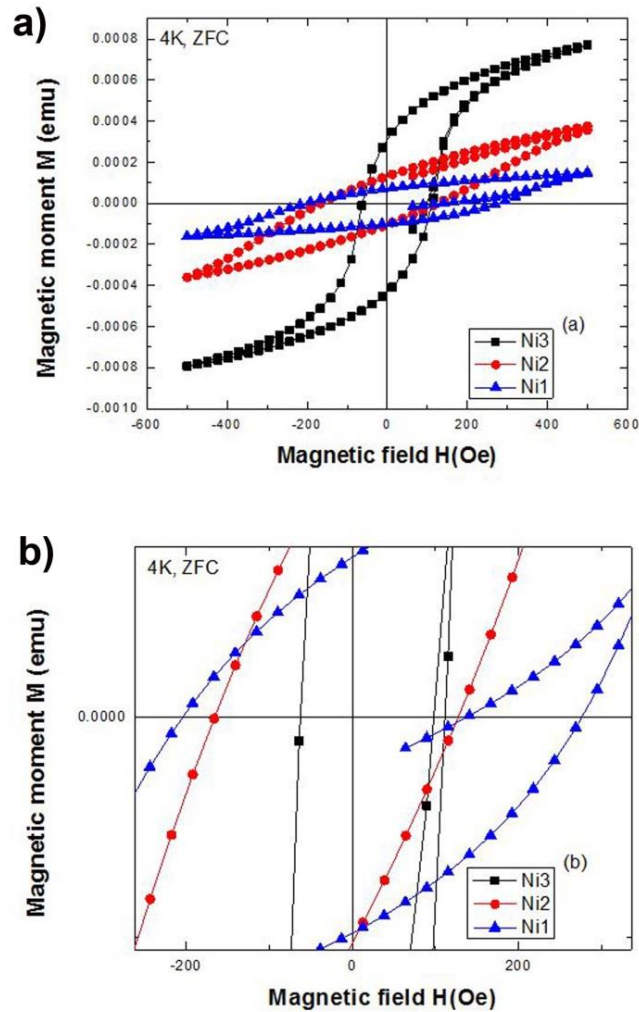


Figure 8.4 (a) Comparison of isothermal M-H curves measured on Ni1, Ni2 and Ni3 under in-plane configuration measured 4 K. (b) A significant M-H loop shift toward the positive magnetic field axis, called positive exchange bias (PEB) for Ni1, negative exchange bias (NEB) (M-H loop shift toward negative field axis) for Ni2 and PEB for Ni3 have been observed when each sample was cooled under zero field and then measured during the warming up cycle.

The high  $H_c$  observed in Ni1 could be due to the island-like morphology, causing higher shape and magneto-crystalline anisotropy contributing to  $H_c$ . It is plausible that the thinner epitaxial films have sources of localized stresses due to coherency strain, which cause domain wall pinning and hence, higher  $H_c$ . Such strong morphology-dependent  $H_c$  was reported earlier in the case of epitaxial FePt system [31].

Previous studies on Ni nanowires [11] have reported  $H_c$  values of 1200 Oe, explained in terms of macroscopic magnetic interactions and peculiar domain structure. While the observed  $H_c$  is comparable to the values ( $\sim 200$  Oe) reported in previous studies [12] on Ni/MgO (wafer), prepared by MBE technique, the  $H_{EB}$  ( $\sim 16$  Oe) observed in this work is more than double that of previous reports [12]. In that work, the  $H_{EB}$  has been argued to be due to the formation (unwanted) of NiO at Ni/MgO. We believe that this is not the case here as our STEM-Z images show clean and sharp interface with no NiO present. Such positive exchange bias has been observed in our earlier work [20] on  $Ni_{82.5}Fe_{17.5}/MgO/TiN/Si$  (100) when the sample was zero field cooled. The observed variation in the nature of exchange bias may be assigned to the morphology-associated residual strain and magnetic anisotropy. Similar to our results, a sign change in exchange bias from square shaped island to continuous film of NiO/Ni samples was reported earlier, attributed to the interplay between shape and unidirectional anisotropy [32]. Such transition from positive to negative exchange bias has been reported earlier in the case of Ni/FeF<sub>2</sub> heterostructures [33]. Field induced transitions from positive exchange bias to negative exchange bias have also been

reported [34] in previous studies on  $\text{Ni}_{80}\text{Fe}_{20}/(\text{Ni,Fe})\text{O}$ , and ascribed to the modification in the interface exchange coupling. Unlike the previous studies, in the current work, we are able to tune the nature of exchange bias by changing the morphology and thickness of Ni film, without applying external magnetic field or varying the measurement temperature. The variation in the sign of exchange bias as a function of Ni thin film morphology follows the trend of lattice parameters and residual strain (see table 8.1). Therefore it is more likely that the exchange bias is related with the residual strain. However, additional work is necessary to arrive at a complete understanding.

#### **8.4 Conclusions**

An epitaxial integration of Ni/MgO thin films on the technologically important substrate Si (100) is demonstrated, and their magnetic properties is investigated as a function of Ni thin film morphology and thickness. Most importantly, the nature of intrinsic exchange bias that changed from positive to negative to positive, is ascribed to morphology-associated residual strain. The present work represents a significant step in the realization of magnetic devices integrated with the Si-platform.

## References

- [1] Narayan J, Chen Y, Moon RM. *Nickel colloids in reduced Ni-doped magnesium-oxide* Physical Review Letters. 1981;46:1491-4.
- [2] Ramachandran S, Narayan J, Prater JT. *Magnetic properties of Ni-doped MgO diluted magnetic insulators*. Applied Physics Letters. 2007;90.
- [3] Lin C, Xu YH, Naramoto H, Wei P, Kitazawa S, Narumi K. *Morphology evolution of thin Ni film on MgO(100) substrate*. Journal of Physics D-Applied Physics. 2002;35:1864-6.
- [4] Choi YC, Shin YM, Lim SC, Bae DJ, Lee YH, Lee BS, et al. *Effect of surface morphology of Ni thin film on the growth of aligned carbon nanotubes by microwave plasma-enhanced chemical vapor deposition*. Journal of Applied Physics. 2000;88:4898-903.
- [5] Raatz G, Woltersdorf J. *Structure of metal deposits on ceramic materials studied in the Ni/MgO system*. Physica Status Solidi a-Applied Research. 1989;113:131-41.
- [6] McCaffrey JP, Svedberg EB, Phillips JR, Madsen LD. *Epitaxial variations of Ni films grown on MgO(0 0 1)*. Journal of Crystal Growth. 1999;200:498-504.
- [7] Svedberg EB, Sandstrom P, Sundgren J, Greene JE, Madsen LD. *Epitaxial growth of Ni on MgO(002)1x1: surface interaction vs. multidomain strain relief*. Surface Science. 1999;429:206-16.
- [8] Reniers F, Delplancke MP, Asskali A, Rooryck V, VanSinay O. *Glow discharge sputtering deposition of thin films of Ag, Cr, Cu, Ni, Pd, Rh and their binary alloys onto*

*NaCl and MgO experimental parameters and epitaxy.* Applied Surface Science. 1996;92:35-42.

[9] Qiu H, Nakai H, Hashimoto M, Safran G, Adamik M, Barna PB, et al. *Epitaxial growth and characterization of Ni films grown on MgO(001) by biased direct-current sputter deposition.* Journal of Vacuum Science & Technology A. 1994;12:2855-8.

[10] Lukaszew RA, Zhang ZD, Stoica V, Clarke R. *Annealing effects on (001) Ni films grown on MgO.* Applied Surface Science. 2003;219:74-9.

[11] Nielsch K, Wehrspohn RB, Barthel J, Kirschner J, Gosele U, Fischer SF, et al. *Hexagonally ordered 100 nm period nickel nanowire arrays.* Applied Physics Letters. 2001;79:1360-2.

[12] Lukaszew RA, Mitra M, Zhang Z, Yeadon M. *Exchange bias on epitaxial Ni films due to ultrathin NiO layer.* European Physical Journal B. 2005;45:181-4.

[13] Wu F, Narayan J. *Controlled Epitaxial Growth of Body-Centered Cubic and Face-Centered Cubic Cu on MgO for Integration on Si.* Crystal Growth & Design. 2013;13:5018-24.

[14] Rao SS, Prater JT, Wu F, Shelton CT, Maria JP, Narayan J. *Interface Magnetism in Epitaxial BiFeO<sub>3</sub>-La<sub>0.7</sub>Sr<sub>0.3</sub>MnO<sub>3</sub> Heterostructures Integrated on Si(100).* Nano Letters. 2013;13:5814-21.

[15] S.S. Rao, J.T. Prater, Fan Wu, S. Nori, D. Kumar, L. Yue, et al. *Positive exchange bias in epitaxial permalloy/MgO integrated with Si (1 0 0).* Current Opinion in Solid State and Materials Science. 2014;in press.

- [16] Lee YF, Wu F, Kumar R, Hunte F, Schwartz J, Narayan J. *Epitaxial integration of dilute magnetic semiconductor  $Sr_3SnO$  with Si (001)*. Applied Physics Letters. 2013;103:-.
- [17] Wu F, Wen HM, Lavernia EJ, Narayan J, Zhu YT. *Twin intersection mechanisms in nanocrystalline fcc metals*. Materials Science and Engineering: A. 2013;585:292-6.
- [18] Bayati MR, Molaei R, Wu F, Budai JD, Liu Y, Narayan RJ, et al. *Correlation between structure and semiconductor-to-metal transition characteristics of  $VO_2/TiO_2$ /sapphire thin film heterostructures*. Acta Materialia. 2013;61:7805-15.
- [19] Narayan J, Larson BC. *Domain epitaxy: A unified paradigm for thin film growth*. Journal of Applied Physics. 2003;93:278-85.
- [20] Rao SS, Prater JT, Wu F, Nori S, Kumar D, Narayan J. *Integration of epitaxial permalloy on Si (100) through domain matching epitaxy paradigm*. Current Opinion in Solid State and Materials Science. 2013;18:1-5.
- [21] Wu F, Zhu YT, Narayan J. *Grain size effect on twin density in as-deposited nanocrystalline Cu film*. Philosophical Magazine. 2013;93:4355-63.
- [22] Wu F, Zhu YT, Narayan J. *Macroscopic Twinning Strain in Nanocrystalline Cu*. Materials Research Letters. 2014;2:63-9.
- [23] JP Hirth, Lothe J. *Theory of dislocations*. New York: McGraw-Hill; 1968.
- [24] Narayan J. *Recent progress in thin film epitaxy across the misfit scale (2011 Acta Gold Medal Paper)*. Acta Materialia. 2013;61:2703-24.

- [25] Hameed S, Talagala P, Naik R, Wenger LE, Naik VM, Proksch R. *Analysis of disordered stripe magnetic domains in strained epitaxial Ni(001) films*. Physical Review B. 2001;64:184406.
- [26] SSLB F. *Thin film materials: stress, defect formation, and surface evolution*. New York: Cambridge University Press; 2003.
- [27] Johnson HT, Freund LB. *Mechanics of coherent and dislocated island morphologies in strained epitaxial material systems*. Journal of Applied Physics. 1997;81:6081-90.
- [28] Narayan J, Tiwari P, Chen X, Singh J, Chowdhury R, Zheleva T. *Epitaxial growth of TiN films on (100) silicon substrates by laser physical vapor deposition*. Applied Physics Letters. 1992;61:1290-2.
- [29] Jung JS, Kim EM, Chae WS, Malkinski LM, Lim JH, O'Connor C, et al. *Electrodeposited Nickel Nanodots Array on the Silicon Wafer*. Bulletin of the Korean Chemical Society. 2008;29:2169-71.
- [30] Gupta A, Narayan J, Kumar D. *Magnetic Properties of Self-Assembled Ni Nanoparticles in Two Dimensional Structures*. Journal of Nanoscience and Nanotechnology. 2009;9:3993-6.
- [31] Trichy GR, Chakraborti D, Narayan J, Prater JT. *Structure-magnetic property correlations in the epitaxial FePt system*. Applied Physics Letters. 2008;92.
- [32] Asshoff P, Theis-Broehl K, Petravic O, Zabel H. *Vortex states in patterned exchange biased NiO/Ni samples*. Journal of Applied Physics. 2009;106.

[33] Kovylyna M, Erekhinsky M, Morales R, Villegas JE, Schuller IK, Labarta A, et al. *Tuning exchange bias in Ni/FeF<sub>2</sub> heterostructures using antidot arrays*. Applied Physics Letters. 2009;95.

[34] Ouyang H, Lin KW, Liu CC, Lo SC, Tzeng YM, Guo ZY, et al. *Exchange bias dependence on interface spin alignment in a Ni<sub>80</sub>Fe<sub>20</sub>/(Ni,Fe)O thin film*. Physical Review Letters. 2007;98.

## Chapter 9

### Structure and properties of epitaxial Cu<sub>3</sub>Ge films on sapphire

In this chapter, epitaxial Cu<sub>3</sub>Ge thin films were fabricated on c-plane sapphire substrates. The systematic study on the crystallinity of Cu<sub>3</sub>Ge thin films was carried out to establish correlations of epitaxial characteristics with substrate lattice misfit. The crystallinity and epitaxy of the as-grown Cu<sub>3</sub>Ge thin films are improved considerably, due to a novel design of our deposition system. The epitaxial characteristics and formation of twins in Cu<sub>3</sub>Ge are investigated and a mechanism of twin formation in Cu<sub>3</sub>Ge  $\epsilon_1$ -phase is discussed. The present Cu<sub>3</sub>Ge thin film with controlled crystallinity and defect structure is a promising candidate for the next-generation metallization material in semiconductor industry.

#### 9.1 Introduction

Cu<sub>3</sub>Ge has received widespread attention in microelectronics industry due to its low bulk resistivity ( $\sim 6 \mu\Omega \text{ cm}$  compared with  $\sim 2 \mu\Omega \text{ cm}$  for Cu) over a large Ge composition range of 25-35 at.% Ge [1, 2] and its stability up to 450 °C [1]. It also

reduces the out diffusion of Cu [3], such that the service life and performance of devices and interconnects are improved considerably. Furthermore, Cu<sub>3</sub>Ge remains stable against oxidation in air up to ~500 °C [3, 4]. Consequently, Cu<sub>3</sub>Ge has been considered to be a candidate for contacts and interconnections, as an alternative to Cu, in advanced integrated circuit devices.

The Cu<sub>3</sub>Ge  $\epsilon_1$ -phase has been grown in the form of polycrystalline films on various substrates, such as Si [3, 5-7], Si<sub>x</sub>Ge<sub>1-x</sub> [5, 6, 8], Ge [7, 9], GaAs [10-12], GaN [13], YBa<sub>2</sub>Cu<sub>3</sub>O<sub>7-x</sub> [14], Ta/TaN [15]. Different deposition methods have been explored to fabricate Cu<sub>3</sub>Ge thin films, such as Physical Vapor Deposition (including sputtering, electron beam, and thermal evaporation) [1-3, 9, 14, 16], thermal evaporation of the melt of Cu-Ge mixtures [17], and vapor–solid reaction of GeH<sub>4</sub> with Cu films [15]. However, all of these Cu<sub>3</sub>Ge films were polycrystalline with a poor crystallinity. For example, thick layers of Cu and Ge were deposited separately by electron-beam and thermal evaporation, and then annealed for reaction [1-3, 5-12, 14], resulting to polycrystalline Cu<sub>3</sub>Ge films frequently with excess Ge. Cu<sub>3</sub>Ge films with a better crystallinity are highly desired due to the reduced diffusion path (grain boundaries) and lower electrical resistivity.

Here I report the fabrication of Cu<sub>3</sub>Ge thin films on c- plane sapphire substrates. Here I show that  $\epsilon_1$ -Cu<sub>3</sub>Ge phase (orthorhombic) can be grown by the paradigm of domain matching epitaxy on c-plane sapphire, having a six-fold symmetry. This opens

the door for epitaxial  $\text{Cu}_3\text{Ge}$  as contacts on other substrates. Due to its low electrical but high heat conductivities, sapphire has been widely used as an insulating substrate in high-power, high-frequency CMOS integrated circuits, especially for high-power radio-frequency applications. Single-crystal sapphire has also been commonly used in semiconductor devices, such as blue light-emitting diodes (LED) [18]. Consequently, the integration of  $\text{Cu}_3\text{Ge}$  as contacts or interconnections onto sapphire substrate will have tremendous promise in semiconductor industry. The systematic study on the crystallinity and epitaxy of  $\text{Cu}_3\text{Ge}$  thin films is performed. More importantly, a novel deposition route of  $\text{Cu}_3\text{Ge}$  thin films is designed, such that the crystallinity of the as-grown  $\text{Cu}_3\text{Ge}$  thin films is expected to be improved significantly. Twinning in as-grown  $\text{Cu}_3\text{Ge}$  thin films has never been reported previously. Twins can reduce the diffusion of Cu and Ge atoms into the substrate or adjacent layers, and enhance the mechanical stability of  $\text{Cu}_3\text{Ge}$  thin films due to the improved strength and ductility and higher electromigration resistance. Since the stacking fault energy (SFE) of most metals is lowered by the addition of alloying elements [19], twins may form more easily in  $\text{Cu}_3\text{Ge}$  thin films than in pure Cu. Therefore, the investigation of twinning structure in the as-grown  $\text{Cu}_3\text{Ge}$  thin film is also one goal of the present study. The as-grown  $\text{Cu}_3\text{Ge}$  thin films with controlled crystallinity and defect structure will be a promising candidate for the next-generation metallization material in semiconductor industry.

## 9.2 Experimental Approach

Multiple repetitions of Ge/Cu depositions on sapphire substrates were performed by PLD technique. In each repetition, the Ge and Cu layers were controlled to be ultrathin, such that Cu and Ge atoms can mix completely and bond with each other. Note that for PLD, the energy of the ablated species can be as high as 10 to 100 eV, while for thermal or e-beam evaporation techniques, the energy of the ejected species is about 0.1 eV at 1200 K [20]. The excess kinetic energies of the Cu and Ge atoms will contribute to higher diffusion and reaction rates, thus a  $\text{Cu}_3\text{Ge}$  film with better crystallinity is expected. Five samples were fabricated at  $400 \pm 10$  °C, with a laser shot frequency of 1HZ. Sample 1-5 were deposited on c-plane sapphire substrates to systematically investigate the crystallinity and microstructure of the obtained  $\text{Cu}_3\text{Ge}$  film. For all five samples, 90 repetitions of Ge/Cu depositions were performed, but the pulse numbers for Ge and Cu irradiations in each repetition vary for different samples. The detailed deposition parameters are listed out in table 9.1. All the depositions of these films were carried out in a multi-target stainless steel laser deposition chamber using a pulsed KrF excimer laser (wavelength 248 nm, pulse duration 25 ns). The targets were 4N pure Cu and Ge sheets purchased from ESPI Metals Inc. The PLD chamber was evacuated by a turbomolecular pump to a vacuum of  $\sim 9.0 \times 10^{-7}$  torr. While heating the substrate to the deposition temperature ( $400 \pm 10$  °C), the chamber vacuum decreased to  $\sim 3.0 \times 10^{-4}$  torr. The laser beam was focused onto the targets at a  $45^\circ$  incidence angle and had a

square spot size of 2mm× 3 mm. The laser was excited from its source under “High Voltage Constant” mode so that the exciting voltage was maintained at 23.8 keV, and the energy of laser beam at the front of the chamber was ~ 0.29–0.30 J. As a result, the energy density of the laser beam was estimated to be 4.8 - 5 J cm<sup>-2</sup>. The sapphire substrates were initially cleaned through a multi-step procedure including boiling in acetone at 150 °C for 5 min, ultrasonic cleaning in acetone for 5 min and ultrasonic cleaning in methanol for 5 min. The cleaned substrates were fully dried by nitrogen gun and then loaded into the deposition chamber where the target–substrate distance was 4 cm. The sapphire substrates were held parallel to the targets during deposition, and the targets were rotated in order to provide a uniform ablation and avoid pitting on the target surface.

The microstructural characterization of the as-deposited films was performed by TEM, using a JEOL-2000FX analytical electron microscope and HRTEM, using a JEOL-2010F analytical electron microscope equipped with a Gatan image filter tuning attachment, which has a point-to-point resolution of 0.18 nm. The samples for TEM observation were prepared using Focus Ion Beam (FIB) technique. Au and Pt layers were deposited on Cu<sub>3</sub>Ge films during FIB sample preparation for electron conduction and protection. X-Ray Diffraction (XRD)  $\theta$ –2 $\theta$  scan analysis was carried out using a Rigaku X-ray diffractometer with Cu-K $\alpha$  radiation ( $\lambda=0.154$  nm).

Table 9.1: PLD parameters of Cu<sub>3</sub>Ge thin films for sample 1 to 5

Sample number	substrate (sapphire)	Deposition temperature	Laser frequency	Pulse number in each repetition of deposition		Number of deposition repetitions
				Ge	Cu	
1	C-plane	400±10 °C	1 HZ	5	35	90
2	C-plane	400±10 °C	1 HZ	5	25	90
3	C-plane	400±10 °C	1 HZ	5	15	90
4	C-plane	400±10 °C	1 HZ	2	14	90
5	C-plane	400±10 °C	1 HZ	1	7	90

### 9.3 Results and Discussion

Figure 9.1 demonstrates the XRD  $\theta$ - $2\theta$  patterns of sample 1 to 5. In each repetition, the Ge and Cu layers were designed to be ultrathin, such that Cu and Ge atoms can react completely and form the desired phase.

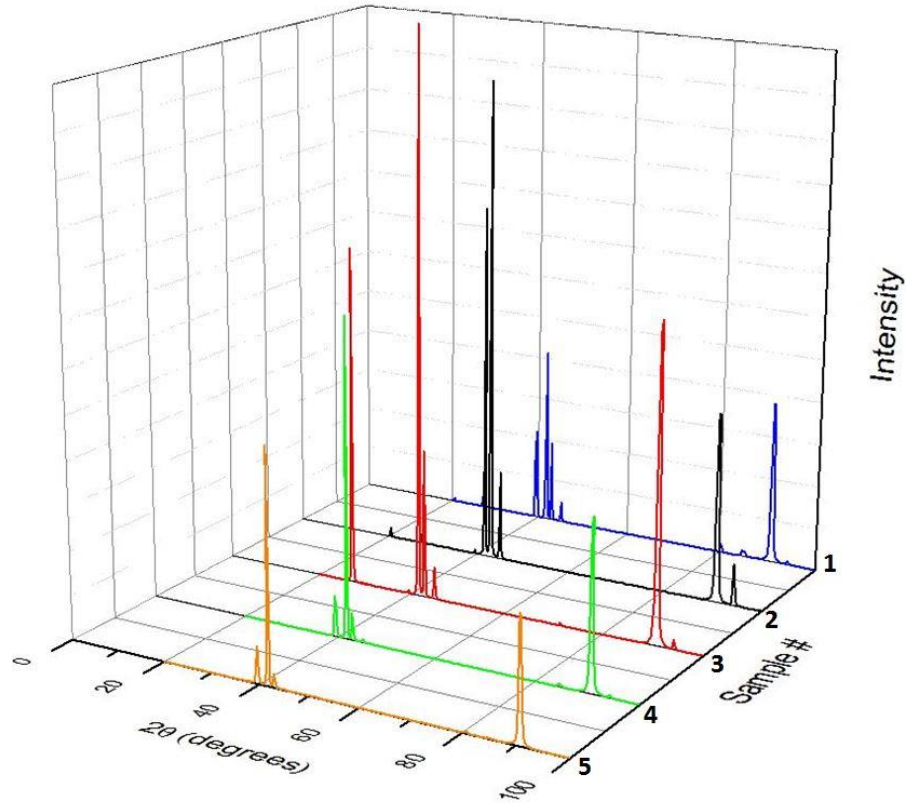


Figure 9.1: XRD  $\theta$ - $2\theta$  patterns for samples on c-plane sapphire ( $\text{Al}_2\text{O}_3\{0001\}$ ). For all five samples, the laser shot frequency is 1HZ, the deposition temperature is 400C, and 90 repetitions of depositions of Cu/Ge were performed, while numbers of laser pulses for Cu and Ge depositions are different: sample 1: Cu:Ge=35:5; sample 2: Cu:Ge=25:5; sample 3: Cu:Ge=15:5; sample 4: Cu:Ge=14:2; sample 5: Cu:Ge=7:1.

This innovative design of deposition route is distinguished from previous fabrication methods [1-3, 9, 14, 16], where a thick layer of Cu and a thick layer of Ge

were deposited separately by electron-beam and thermal evaporation, and then annealed for reaction. Previously the layers were too thick for Cu and Ge atoms to mix completely so that polycrystalline  $\text{Cu}_3\text{Ge}$  thin films with poor crystallinities and often with excess Ge were obtained [1-3, 9, 14, 16]. Here the pulse numbers for Cu and Ge deposition in each repetition decreased from sample 1 to sample 5, as shown in table 9.1. The crystallinity of  $\text{Cu}_3\text{Ge}$  films are thus expected to be improved from sample 1 to sample 5, as the thickness of each Cu/Ge layer is getting thinner and the reaction rate is increased. In all five XRD  $\theta$ - $2\theta$  patterns, the two peaks located at  $41.68^\circ$  and  $90.68^\circ$  correspond to the (0006) and (00012) planes of c-plane sapphire, respectively. For sample 1, the peaks located at  $39.56^\circ$ ,  $41.80^\circ$ ,  $43.00^\circ$ ,  $80.20^\circ$ ,  $84.56^\circ$  and  $91.64^\circ$  correspond to  $\epsilon_1\text{-Cu}_3\text{Ge}$  (002), (020), (-111), (-131), (004) and (040) planes, respectively. Note that at  $27.32^\circ$ , there is a peak corresponding to Ge (111) plane, indicating the film obtained for sample 1 is polycrystalline  $\text{Cu}_3\text{Ge}$  film with existence of excess Ge grains, which is similar to what was obtained in previous studies [1-3, 9, 14, 16]. A careful examination on the XRD patterns reveals that the Ge (111) peak at  $27.32^\circ$  continues to exist for sample 2 and 3, but disappears in the patterns of sample 4 and 5. This is attributed to two reasons: 1): the Cu and Ge layers were still too thick in sample 1 so that Cu and Ge could not react completely to form pure  $\text{Cu}_3\text{Ge}$  during each repetition; 2): the Ge:Cu pulse ratio in each repetition was too high for sample 2 and 3, such that excessive Ge atoms bonded with themselves to form pure Ge grains, intermixed with the  $\text{Cu}_3\text{Ge}$  grains. In contrast, the pulse numbers of Ge and Cu

depositions in each repetition for sample 4 and 5 were reduced to 1 and 7, such that all Ge atoms bonded with Cu to form Cu<sub>3</sub>Ge phase and no extra Ge was left. For sample 2 and 3, the XRD peaks corresponding to  $\epsilon_1$ -Cu<sub>3</sub>Ge (002), (020), (-111), (103) and (040) planes exist, but the crystallinity has been improved compared to sample 1. The XRD  $\theta$ - $2\theta$  patterns of sample 4 and 5 only show peaks corresponding to  $\epsilon_1$ -Cu<sub>3</sub>Ge (002) and (020) planes, indicating a biaxial relationship between the Cu<sub>3</sub>Ge thin film and the c-sapphire substrate. The crystallinity and epitaxy of the  $\epsilon_1$ -Cu<sub>3</sub>Ge films in samples 4 and 5 have been improved considerably, by controlling the Cu and Ge layers to be extremely thin. Since only 1 laser pulse was used to ablate Ge in each repetition, this should be the optimum condition for Cu<sub>3</sub>Ge films by PLD with the best crystallinity. The quality and crystallinity of Cu<sub>3</sub>Ge films in sample 1-5 are also evidenced by the plan-view images of these samples in the optical microscope (shown as Figure S9.1 in Supporting Information). Figure S9.1 (a)-(e) correspond to the plan-view images of samples (1)-(5), respectively. Chunks appear in the plan-view images of sample 1, 2, and 3, possibly due to the existence of the Ge grains intermixed with the Cu<sub>3</sub>Ge phase. In contrast, uniform films are observed in Figure S9.1 (e) and (f), proving the high quality of the Cu<sub>3</sub>Ge films with a good crystallinity for sample 4 and 5. The detailed observation and analysis of film morphology of the sample with the best crystallinity and epitaxy (sample 5) are demonstrated as following.

The  $\text{Cu}_3\text{Ge}$  film on c-sapphire in sample 5 is demonstrated in the plan-view SEM image (shown as Figure S9.2 in Supporting Information). A uniform  $\text{Cu}_3\text{Ge}$  film grown via 3-D growth mode is observed, without the existence of chunks and excessive Ge grains. Figure 9.2 (a) is the typical bright-field cross-section TEM image, showing the film morphology of sample 5. The Au and Pt layers were deposited during FIB sample preparation for electron conduction and protection. The  $\text{Cu}_3\text{Ge}$  film grows on the c-plane sapphire via Stranski–Krastanov mode (also known as 'layer-plus-island growth'), i.e. the film growth follows a two-step process: 1): the  $\text{Cu}_3\text{Ge}$  initially grew in a layer-by-layer fashion on the c-plane sapphire to form an ultrathin uniform film up to several monolayers thick; 2): beyond a critical thickness, the  $\text{Cu}_3\text{Ge}$  growth continued through the nucleation and coalescence of adsorbate islands.

The average thickness of the  $\text{Cu}_3\text{Ge}$  film is  $\sim 120$  nm. The interface between the  $\text{Cu}_3\text{Ge}$  film and the c-plane sapphire is sharp and straight, without traces of diffusion and secondary phase over a large area. To study the orientation relationships between the  $\text{Cu}_3\text{Ge}$  film and the sapphire substrate, selected area diffraction pattern (SADP) was obtained at the interface for a single  $\text{Cu}_3\text{Ge}$  island and shown in Figure 9.2 (b), clearly demonstrating an epitaxial relationship between the single-crystal  $\text{Cu}_3\text{Ge}$  island and c-sapphire substrate.

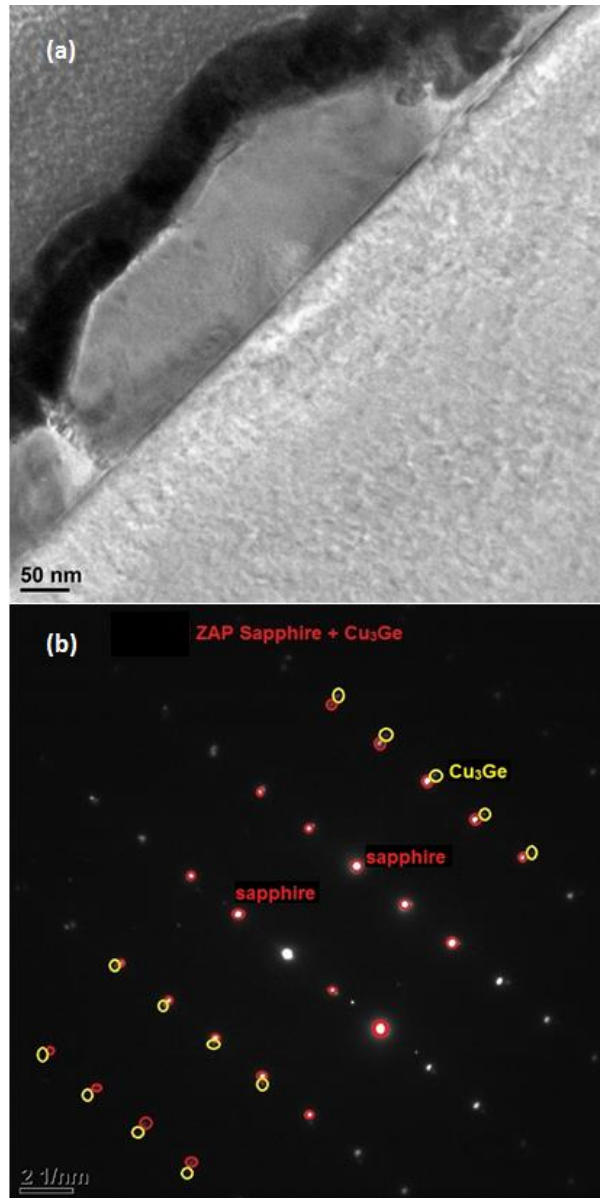


Figure 9.2: (a) The typical bright-field cross-section TEM image showing the film morphology of sample 5. (b) The zone-axis pattern (ZAP) of sample 5, clearly demonstrating an epitaxial relationship between the single-crystal Cu<sub>3</sub>Ge island and c-sapphire substrate.

The low-order diffraction points of  $\text{Cu}_3\text{Ge}$  lie so close to those of the c-sapphire that they coincide with each other, and only higher-order diffraction points corresponding to different planes of  $\text{Cu}_3\text{Ge}$  and c-sapphire split but appear along the same directions.

To investigate the atomic structure at the interface region between the  $\text{Cu}_3\text{Ge}$  island and c-sapphire substrate, HRTEM images were collected, as shown in Figure 9.3 (a). The viewing direction is  $[110]$  zone of c-sapphire ( $[11-20]$  zone in Miller-Bravais Indices system). Periodic contrast is visible along the interface due to the existence of misfit dislocations with a certain separation, indicating that the  $\text{Cu}_3\text{Ge}$  island/c-sapphire interface is semicoherent [21]. The periodic dislocation (edge dislocations in nature) exists at the interface to accommodate the misfit strain between the two phases. For c-sapphire, the interface plane is  $(0001)$  plane and parallel to the viewing zone. For  $\text{Cu}_3\text{Ge}$ , the interface plane is  $(010)$  plane. The matching scenario at the interface is illustrated schematically in Figure 9.3 (b). The  $(0001)$  plane of sapphire has atoms located at the four corners of a rectangle, with a width of  $4.759 \text{ \AA}$  and a length of  $8.243 \text{ \AA}$ , while  $\epsilon_1\text{-Cu}_3\text{Ge}$  has an orthorhombic structure, and  $(010)$  plane is also in rectangular shape, with a width of  $4.54 \text{ \AA}$  and a length of  $4.22 \text{ \AA}$ . Therefore, one lattice of the c-sapphire  $(0001)$  plane matches with 2 lattices of  $\epsilon_1\text{-Cu}_3\text{Ge}(010)$  plane, as shown in Figure 9.3 (b). The lattice misfit of the width between c-sapphire  $(0001)$  and  $\epsilon_1\text{-Cu}_3\text{Ge}(010)$  is  $\sim 4.60\%$ , and the lattice misfit of the length between one r-sapphire

(0001) and two  $\epsilon_1$ -Cu<sub>3</sub>Ge(010) is  $\sim -2.33\%$ . To study the atomic structure at the interface in detail, the region close to that of Figure 9.3 (a) is enlarged for observation using HRTEM, as shown in Figure 9.3 (c). The Cu<sub>3</sub>Ge planes connect with the lattice planes of c-sapphire across the interface between the interfacial dislocations and bend only within the localized width of the misfit dislocations. The matching of Cu<sub>3</sub>Ge and c-sapphire can be explained by the domain matching epitaxy (DME) paradigm [22], since the misfit strain between two phases is accommodated by misfit dislocations at the interface, without the pseudomorphic growth of Cu<sub>3</sub>Ge and appearance of threading dislocations. The misfit strain along the direction perpendicular to the interface is relaxed when 9/8 and 8/7 domains alternate with a relative frequency of 0.5. Arrangement of misfit dislocations at the Cu<sub>3</sub>Ge/c-sapphire interface is observed in Figure 9.3 (c) where alternation of 9/8 and 8/7 domains is evident.

Figure 9.4 is a typical HRTEM image showing the planar defects in Cu<sub>3</sub>Ge film, in which twins and stacking faults (SF) coexist. A careful study at the twin boundary (TB) region reveals the existence of extrinsic stacking fault, right on the plane next to the TB plane of the lower twin. The mechanism of this arrangement can be explained by the concept of “generalized planar fault energies (GPFEs)”, in which stacking fault energy (SFE), unstable stacking fault energy (USFE) and unstable twin fault energy (UTE) play together as the intrinsic material properties to affect the twinning propensity [23].

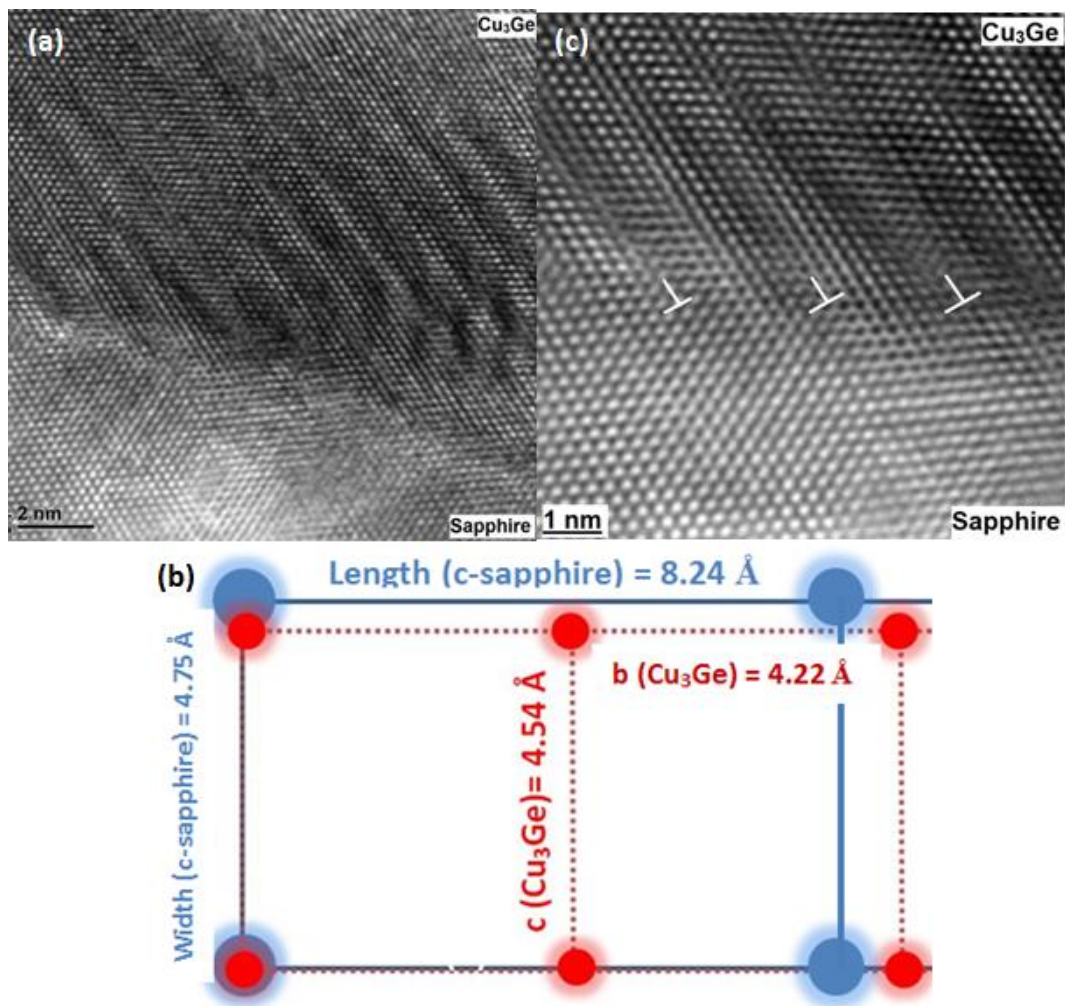


Figure 9.3: (a) The HRTEM image showing the atomic structure at the interface region between the Cu<sub>3</sub>Ge island and c-sapphire substrate. The viewing direction is [110] zone of c-sapphire ([11-20] zone in Miller-Bravais Indices system). (b) The schematic illustration of the matching scenario at the interface between  $\epsilon_1$ -Cu<sub>3</sub>Ge(010) and c-sapphire (0001). (c) The HRTEM image at a higher magnification showing the atomic structure at the interface in detail, at the region close to that of (a).

Note that GPFs are used to explain the formation of deformation twins, while the twins in the present  $\text{Cu}_3\text{Ge}$  films were formed during thin film deposition process, without further deformation. However, it has been shown [24] that deformation twins can be dominant in as-deposited films by PLD or other physical vapor deposition techniques. In previous studies [25], Cu alloy was chosen to study twin interaction phenomena, because it has long been established that the addition of alloying elements significantly lowers the SFE of most metals [19].

For the same reason, the  $\text{Cu}_3\text{Ge}$  alloy has a low SFE, due to the adding of Ge into Cu. The low SFE of  $\text{Cu}_3\text{Ge}$  leads to a small energy barrier for the generation of SFs by the nucleation and movements of a leading partial.

However, whether the SF is annihilated, maintained or transformed into a twin depend on the combined effect of SFE, USFE and UTE. The SF will be annihilated if the nucleation and gliding barrier for the trailing partial is small, and will be maintained if the barrier is large. Since this energy barrier for the trailing partial is a function of the difference between USFE and SFE, it should be large for  $\text{Cu}_3\text{Ge}$  due to the existence of SF in our films. This makes it possible for some first partials to slip without trailing partial following them, creating stacking faults.

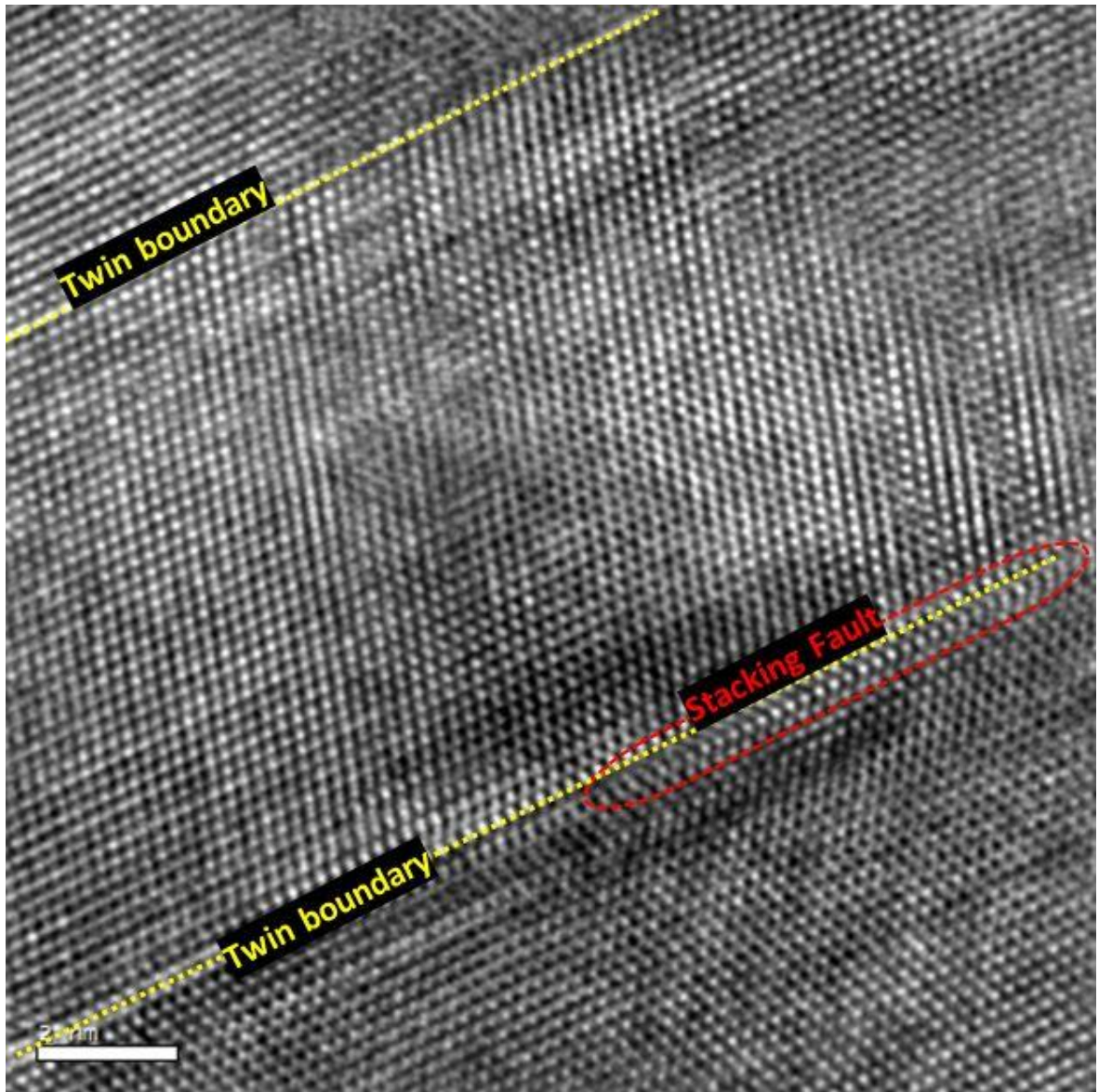


Figure 9.4: A typical HRTEM image showing the planar defects in Cu<sub>3</sub>Ge thin film, in which twins and stacking faults coexist.

Furthermore, since the UTE is not much higher than the USFE, twins are easily generated once a leading partial is emitted and a SF is formed. The more accurate and quantitative calculation of the GPFEs of  $\text{Cu}_3\text{Ge}$  alloy needs to be done by the ab initio approach [23]. Twins in metallic thin film heterostructures have been shown to contribute to superior properties, such as good electrical conductivity, excellent combination of high strength and ductility, and high resistance to electro-migration [23]. They also function to accommodate a part or even the majority of the residual strains in thin films [26]. The present study is the first report of  $\text{Cu}_3\text{Ge}$  thin films with twins. The introduction of twin structure in  $\text{Cu}_3\text{Ge}$  thin film will enhance its mechanical stability due to the improved strength and ductility and higher electro-migration resistance. More importantly, the twin boundaries will function as barriers for diffusion of Cu and Ge atoms into the substrate or adjacent layers, thus making  $\text{Cu}_3\text{Ge}$  with twins a better metallization material.

#### **9.4 Conclusions**

Epitaxial  $\epsilon_1$ - $\text{Cu}_3\text{Ge}$  thin films are fabricated on c-plane sapphire substrate for the first time. The crystallinity of the as-grown  $\text{Cu}_3\text{Ge}$  thin films is improved tremendously here, due to a novel route of deposition.  $\epsilon_1$ - $\text{Cu}_3\text{Ge}$  phase (orthorhombic) can be grown by the paradigm of domain matching epitaxy on c-plane sapphire, which opens the door

for epitaxial  $\text{Cu}_3\text{Ge}$  as contacts on other substrates. In addition, twins are observed and studied in  $\text{Cu}_3\text{Ge}$  thin films for the first time, and its formation mechanism is explained by the concept of generalized planar fault energies (GPFs). Twinning will reduce the diffusion of Cu and Ge atoms into the substrate or adjacent layers, and enhance the mechanical stability of  $\text{Cu}_3\text{Ge}$  thin films due to the improved strength and ductility and higher electro-migration resistance. Therefore, the present  $\text{Cu}_3\text{Ge}$  thin film with controlled crystallinity and defect structure is a promising candidate for the next-generation metallization material in semiconductor industry.

## 9.5 Supporting Information

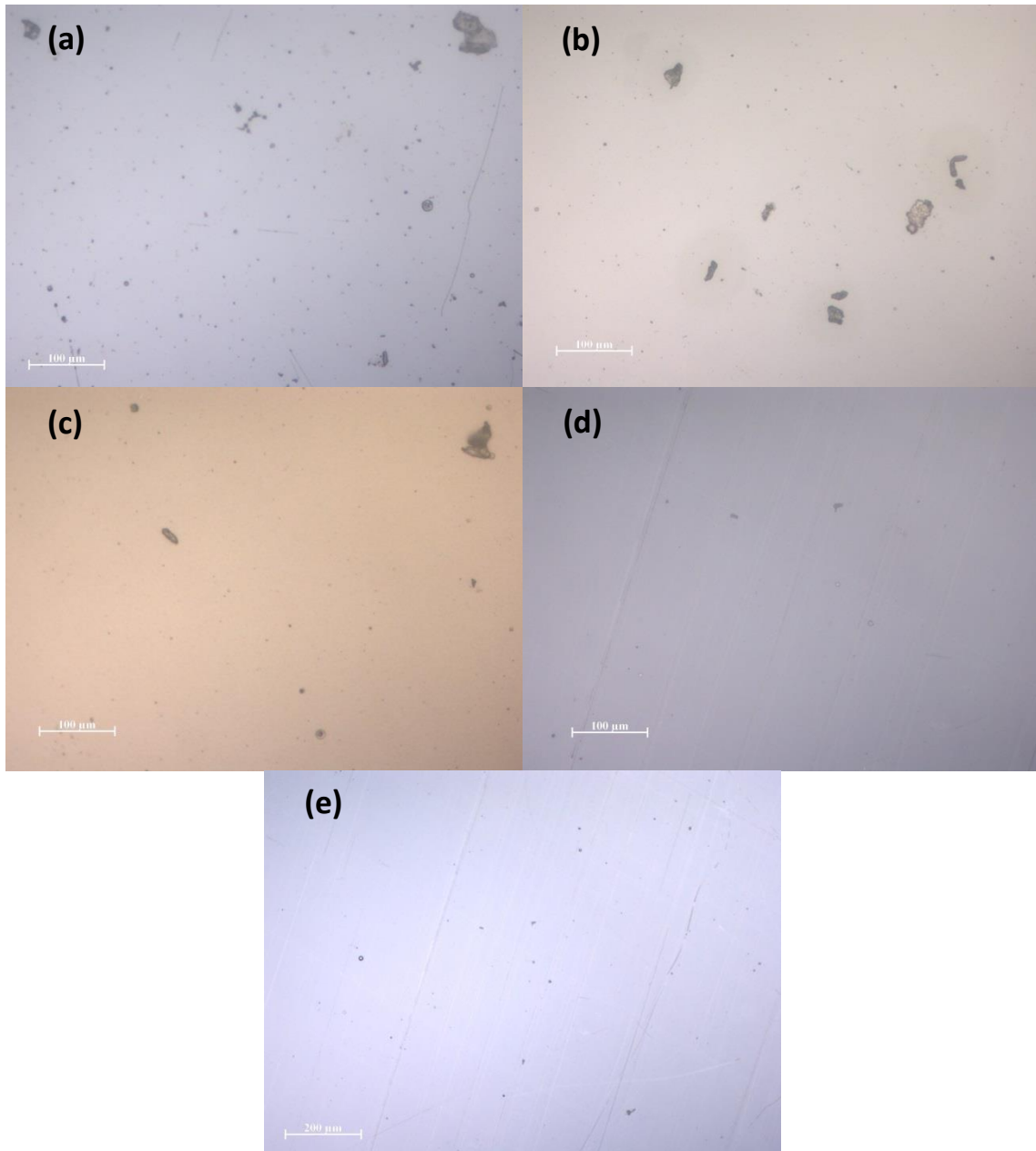


Figure S9.1: (a)-(e): the plan-view images of samples (1)-(5) respectively, observed by optical microscope.

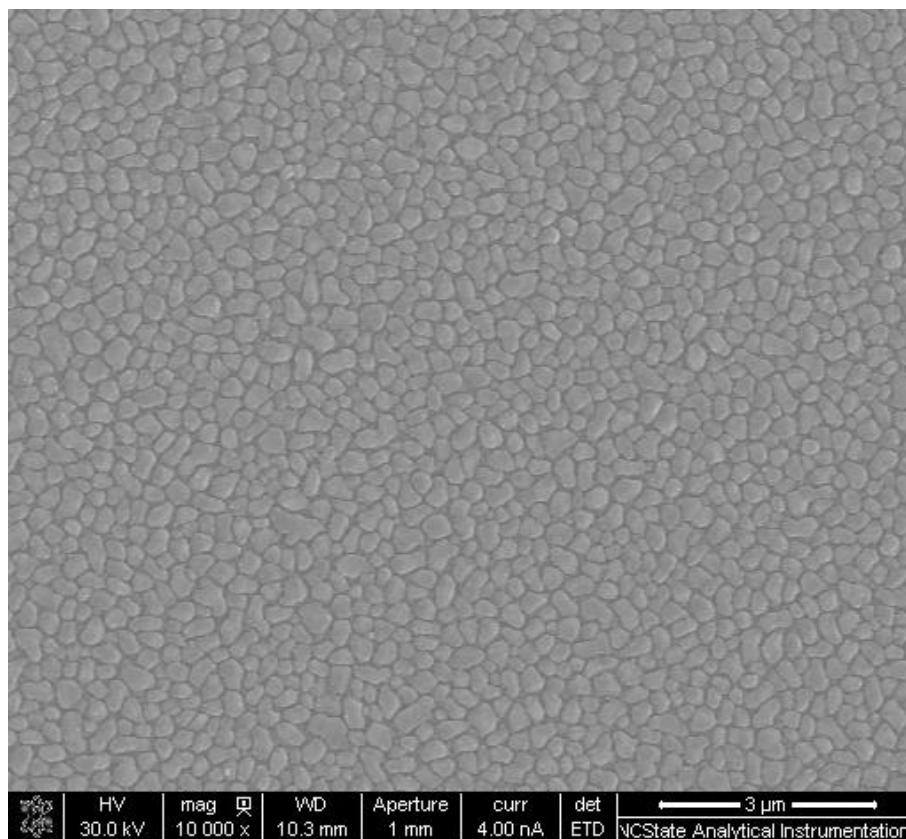


Figure S9.2: Typical plan-view SEM image of the  $\text{Cu}_3\text{Ge}$  film in sample 5, showing a uniform  $\text{Cu}_3\text{Ge}$  film grown via 3-D growth mode, without the formation of chunks and excessive Ge grains.

## References

1. Krusin-Elbaum, L. and M.O. Aboelfotoh, *Unusually low resistivity of copper germanide thin films formed at low temperatures*. Applied Physics Letters, 1991. **58**(12): p. 1341-1343.
2. Doyle, J.P., B.G. Svensson, and M.O. Aboelfotoh, *Copper germanide Schottky barrier contacts to silicon*. Journal of Applied Physics, 1996. **80**(4): p. 2530-2532.
3. Borek, M.A., et al., *Low resistivity copper germanide on (100) Si for contacts and interconnections*. Applied Physics Letters, 1996. **69**(23): p. 3560-3562.
4. Huang, J.S., et al., *Kinetics of Cu<sub>3</sub>Ge formation and reaction with Al*. Journal of Applied Physics, 1997. **82**(2): p. 644-649.
5. Borek, M.A., et al., *Properties of Cu<sub>3</sub>Ge films for contacts to Si and SiGe and Cu metallization*, in *Advanced Interconnects and Contact Materials and Processes for Future Integrated Circuits*, S.P. Murarka, et al., Editors. 1998. p. 269-274.
6. Aboelfotoh, M.O., M.A. Borek, and J. Narayan, *Interaction of Cu and Cu<sub>3</sub>Ge thin films with Si<sub>1-x</sub>Ge<sub>x</sub> alloys*. Applied Physics Letters, 1999. **75**(12): p. 1739-1741.
7. Aboelfotoh, M.O., et al., *Electrical transport properties of Cu<sub>3</sub>Ge thin films*. Journal of Applied Physics, 1994. **75**(3): p. 1616-1619.
8. Aboelfotoh, M.O., M.A. Borek, and J. Narayan, *Microstructure and electrical resistivity of Cu and Cu<sub>3</sub>Ge thin films on Si<sub>1-x</sub>Ge<sub>x</sub> alloy layers*. Journal of Applied Physics, 2000. **87**(1): p. 365-368.

9. Guizzetti, G., et al., *Optical response of Cu<sub>3</sub>Ge thin films*. Journal of Applied Physics, 1996. **79**(10): p. 8115-8117.
10. Aboelfotoh, M.O., M.A. Borek, and J. Narayan, *Ohmic contact to p-type GaAs using Cu<sub>3</sub>Ge*. Applied Physics Letters, 1999. **75**(25): p. 3953-3955.
11. Aboelfotoh, M.O., et al., *Microstructure characterization of Cu<sub>3</sub>Ge/n-type GaAs ohmic contacts*. Journal of Applied Physics, 1994. **76**(10): p. 5760-5763.
12. Aboelfotoh, M.O., C.L. Lin, and J.M. Woodall, *Novel low-resistance ohmic contact to n-type GaAs using Cu<sub>3</sub>Ge*. Applied Physics Letters, 1994. **65**(25): p. 3245-3247.
13. Hsin, H.-C., et al., *Cu<sub>3</sub>Ge Schottky contacts on n-GaN*. Journal of Materials Science: Materials in Electronics, 2002. **13**(4): p. 203-206.
14. Kumar, D., et al., *LaNiO<sub>3</sub> and Cu<sub>3</sub>Ge contacts to YBa<sub>2</sub>Cu<sub>3</sub>O<sub>7-x</sub> films*. Journal of Electronic Materials, 1996. **25**(11): p. 1760-1766.
15. Peter, A.P., et al., *Selective chemical vapor synthesis of Cu<sub>3</sub>Ge: Process optimization and film properties*. Intermetallics, 2013. **34**(0): p. 35-42.
16. Liang, H.H., J.S. Luo, and W.T. Lin, *Room temperature oxidation of Cu<sub>3</sub>Ge and Cu<sub>3</sub>(Si<sub>1-x</sub>Ge<sub>x</sub>) on Si<sub>1-x</sub>Ge<sub>x</sub>*. Materials Science in Semiconductor Processing, 2001. **4**(1-3): p. 233-235.
17. Nath, P. and K.L. Chopra, *Electrical resistivity and thermoelectric power of copper-Germanium films*. Thin Solid Films, 1979. **58**(2): p. 339-343.
18. Bianchi, M.P., *Gallium nitride collector grid solar cell*, 2002, Google Patents.

19. Venables, J.A., *The electron microscopy of deformation twinning*. Journal of Physics and Chemistry of Solids, 1964. **25**(7): p. 685-692.
20. Singh, R.K. and J. Narayan, *Pulsed-laser evaporation technique for deposition of thin films: Physics and theoretical model*. Physical Review B, 1990. **41**(13): p. 8843-8859.
21. Wu, F. and J. Narayan, *Controlled Epitaxial Growth of Body-Centered Cubic and Face-Centered Cubic Cu on MgO for Integration on Si*. Crystal Growth & Design, 2013. **13**(11): p. 5018-5024.
22. Narayan, J. and B.C. Larson, *Domain epitaxy: A unified paradigm for thin film growth*. Journal of Applied Physics, 2003. **93**(1): p. 278-285.
23. Zhu, Y.T., X.Z. Liao, and X.L. Wu, *Deformation twinning in nanocrystalline materials*. Progress in Materials Science, 2012. **57**(1): p. 1-62.
24. Wu, F., Y.T. Zhu, and J. Narayan, *Grain size effect on twin density in as-deposited nanocrystalline Cu film*. Philosophical Magazine, 2013. **93**(35): p. 4355-4363.
25. Wu, F., et al., *Twin intersection mechanisms in nanocrystalline fcc metals*. Materials Science and Engineering: A, 2013. **585**(0): p. 292-296.
26. Wu, F., Y.T. Zhu, and J. Narayan, *Macroscopic Twinning Strain in Nanocrystalline Cu*. Materials Research Letters, 2014. **2**(2): p. 63-69.

## Chapter 10

### Concluding Remarks

In this dissertation project, my research focuses on planar defects, specifically twin and phase interface, in nanocrystalline thin film heterostructures. The outcome of this research project is summarized as following:

#### **1: Grain size effect on twin density in as-deposited nanocrystalline Cu film**

The formation of twins and grain size dependence of twin density in as-fabricated NC Cu films were studied in this project for the first time [1]. The percentage of grains containing twins was found to decrease with decreasing grain size in the grain size range of 2–10 nm. Surprisingly, although the twins formed during the deposition process without mechanical deformation, deformation twins were dominant. Their formation was attributed to the following three reasons: (1) a similar grain size effect with that which occurs for deformation twins; (2) the deviation of the grain surface area density of twins from a constant; and (3) the high internal stress existing in the NC Cu films. This phenomenon may also happen in other NC metallic thin films where internal stresses are high. The presence of deformation twins is contrary to the intuition that growth twins should be dominant in these NC Cu films because the twins were formed

by crystalline growth during a physical deposition process. This novel observation indicates that deformation twins can form easily if the internal stress in the film is high. This phenomenon can also exist in other NC films produced by deposition methods [1].

## **2: Twin intersection mechanisms in nanocrystalline fcc metals**

Twin intersection mechanisms were investigated by observing twin transmission across the boundary of another twin using HRTEM [2]. Based on the experimental observations, I proposed the partial dislocation reaction mechanism for twin transmission phenomenon to occur at the twin boundary in an fcc system. If only some of the partial dislocations transmit across the twin boundary, the twin boundary will deviate from the original configuration. The deviation angle is related to the ratio between the number of incident partials and that of transmitted partials. The proposed mechanism was evidenced by HRTEM observation of twin intersection phenomena in NC fcc materials. The observations and mechanisms proposed [2] can be used to explain other twin intersection phenomena in all fcc materials.

## **3: Macroscopic twinning strain in nanocrystalline Cu**

Most deformation twins in NC fcc metals were reported to produce zero-macrostrain, which was attributed to either random activation of partials (RAP) or cooperative slip of three partials (CSTP). I designed a novel experimental approach [3]

to answer the long-existing question: which mechanism dominates? In my creative research, the RAP mechanism was suppressed, and ~44% twins in NC Cu were found to produce zero-macrostrain via the CSTP mechanism. This indicates that both RAP and CSTP are major mechanisms for generating zero-macrostrain twins. In addition, my research indicates that the stress state affects the twinning mechanism in NC fcc metals, and monotonic activation of partials with the same Burgers vector dominates twin formation under monotonic stress.

#### **4: Fabrication and investigation of the interface between bcc/fcc Cu and MgO on Si**

I reported [4], for the first time, the epitaxial growth by PLD of bcc(t) and fcc Cu on Si(100) and Si(111) substrates using MgO(100)/TiN(100) and MgO(111)/TiN(111) buffer layers. I found that the deposition temperature determined the structure of Cu. At high temperatures, only fcc Cu grows on both MgO/TiN(100) and MgO/TiN(111) templates. At room temperature, an epitaxial layer of bcc(t) Cu grows pseudomorphically on a MgO(100) template up to a critical thickness, while on a MgO/TiN(111) template, the majority of Cu is fcc, and bcc(t) Cu exists occasionally in a three-dimensional island shape. The growth of these heterostructures involves epitaxy across the misfit scale by matching MgO{200} planes with bcc(t) Cu{110} planes. The integration of Cu/MgO on the technologically important Si substrate holds tremendous

promise, because the novel bcc(t) Cu/MgO structure can be integrated with present-day microelectronic or nanoelectronic devices.

### **5: Fabrication and investigation of the interface between Ni and MgO on Si**

By successfully fabricating an epitaxial MgO template on Si using TiN as the buffer layer, epitaxial Ni/MgO stack was successfully integrated on the technologically important silicon substrate [5], which is inexpensive, readily available, and widely used in present-day microelectronic devices. The buffer layer approach demonstrated here holds tremendous promise in present-day microelectronic or nanoelectronic devices. The distinctive magnetic properties such as transition of exchange bias ( $H_{EB}$ ) (from positive to negative to positive) and coercive field ( $H_c$ ) (technologically relevant magnetic device parameters) as a function of Ni thin film morphology are reported.

### **6: Interface and twinning in $Cu_3Ge$ /sapphire thin film heterostructures**

In this project,  $Cu_3Ge$  thin films were fabricated on sapphire substrate for the first time [6]. The first systematic study on the crystallinity of  $Cu_3Ge$  thin films was performed. More importantly, the crystallinity of the as-grown  $Cu_3Ge$  thin films was improved tremendously, due to a novel route of deposition. In addition, twins were observed and studied in  $Cu_3Ge$  thin films for the first time, and its formation mechanism was explained by the concept of generalized planar fault energies (GPFs).

## References

1. Wu, F., Y.T. Zhu, and J. Narayan, *Grain size effect on twin density in as-deposited nanocrystalline Cu film*. Philosophical Magazine, 2013. **93**(35): p. 4355-4363.
2. Wu, F., et al., *Twin intersection mechanisms in nanocrystalline fcc metals*. Materials Science and Engineering: A, 2013. **585**(0): p. 292-296.
3. Wu, F., Y.T. Zhu, and J. Narayan, *Macroscopic Twinning Strain in Nanocrystalline Cu*. Materials Research Letters, 2014. **2**(2): p. 63-69.
4. Wu, F. and J. Narayan, *Controlled Epitaxial Growth of Body-Centered Cubic and Face-Centered Cubic Cu on MgO for Integration on Si*. Crystal Growth & Design, 2013. **13**(11): p. 5018-5024.
5. Wu F., S.S.R., J.T. Prater, Y.T. Zhu, J. Narayan, *Tuning exchange bias in epitaxial Ni/MgO/TiN heterostructures integrated on Si(100)*. Current Opinion in Solid State & Materials Science, 2014. **under review**.
6. Wu F., Z.J.K., Narayan J., Zhu Y.T. , *Structure and properties of epitaxial Cu<sub>3</sub>Ge films on sapphire* Current Opinion in Solid State & Materials Science, 2014. **under review**.